2020

Heat Transfer and Correlations of Jet Array Impingement with Flat and Pimple-Dimpled Plate

Husam Nizar Ahmad Zawati
University of Central Florida, hzawati@knights.ucf.edu

HEAT TRANSFER AND CORRELATIONS OF JET ARRAY IMPINGEMENT WITH FLAT AND PIMPLE-DIMPLED PLATE

by

HUSAM ZAWATI
B.S. Mechanical Engineering, University of Central Florida, 2015
M.S. Mechanical Engineering, University of Central Florida, 2017

A dissertation submitted in partial fulfillment of the requirements
for the degree of Doctor of Philosophy
in the Department of Mechanical and Aerospace Engineering
in the College of Engineering and Computer Science
at the University of Central Florida
Orlando, Florida, the United States of America

Spring Term
2020

Major Professor: Jayanta S. Kapat

ABSTRACT

This study compares and analyses the heat transfer between a novel jet array impingement configuration (designated as NPR) and a baseline jet orifice plate (flat) in a maximum crossflow scheme. Both jet plates feature inline arrays of 20 x 26 circular air jets that orthogonally impinge on a flat target surface consisting of 20 segments, parallel to the jet plates.

The NPR plate consists of staggered semi-spherical pimples (protrusions) and dimples (imprints) with a jet-to-pimple diameter ratio ($D_{j,p}/D_p$) of 0.07 and jet length-to-pimple diameter ratio ($L/D_{j,p}$) of ~ 1 with a protrusion ratio ($t_p/D_{j,p}$) of 2.78. The dimples (imprints) have a jet-to-dimple diameter ratio ($D_{j,d}/D_d$) of 0.14 with an ($L/D_{j,d}$) of 0.5 and an imprint ratio ($t_d/D_{j,d}$) of 1.28. The averaged jet diameter for the NPR plate is calculated based on the definition of the total effective open area of the jets, which is equal to 3.49 mm.

The flat plate is designed to be compared to the NPR plate and consists of jet orifice diameters (D_j) of 3.49 mm, with a length-to-diameter ratio (L/D_j) of ~ 1. In both plate configurations, the streamwise and spanwise directions jet-to-jet spacings (X/D_j), (Y/D_j), respectively, are maintained constant at 7.16.

The physical mechanisms that cause the change in heat transfer, normalized by Nusselt number, when comparing both configurations are discussed in two regions: impingement and crossflow.

Turbulent flow structures and experimental heat transfer are explored over three jet-averaged Reynolds numbers ($Re_{av,j}$) of 5,000, 7,000, and 9,000, and are compared to available numerical results. Jet-to-target wall ratio (Z/D_j) is varied between (2.4, 2.87, 3.25, 4, and 6) jet diameters.

Subsequently, multiple regression of the logarithms is used on the results obtained from the heat transfer experiments and are correlated into a dimensionless approach. Appropriate statistical methods are also reported along with the correlations for both flat and pimple-dimple plates.

Enhancement of up to 23% in the heat transfer coefficient in the NPR plate is seen in the crossflow region, where the crossflow effects are maximized. However, this convex-concaved plate yields lower globally-averaged heat transfer coefficients.

To my mother (thrice), and my father,

To Sara,

To those who suffered through COVID-19 Pandemic.

ACKNOWLEDGMENTS

Foremost, I owe much gratitude to my major advisor and mentor, Dr. Jayanta Kapat, for his support, guidance, and encouragement throughout all my three degrees at the University of Central Florida (UCF). His input and opinions will always remain appreciated. Further, I would like to express much appreciation to him for polishing me down and promoting critical thinking; the inspiration will significantly impact my life and career.

I would like to extend my appreciation to my committee members. The support from Dr. Fernandez, Dr. Bhattacharya, and Dr. Awad improved the impact and quality of my research through their continuous feedback. In addition to my committee members, I would like to thank the faculty and members of the Center for Advanced Turbomachinery and Energy Research (CATER). People of the Mechanical and Aerospace Engineering (MAE) department have always been resourceful, kind, and helpful.

I would also like to thank the personnel from Siemens. Namely, Dr. José Rodriguez and Ms. Megan Schaenzer for their ultimate support and guidance to this work. In addition to Jason and Dr. Yang, for sharing their long experiences with me.

At Siemens Energy Center (SEC) within CATER, I met many great people who became friends over time. In particular, I would like to acknowledge the influence of

Ahmad, Alok, Andrea, Andres, Akshay, Bernie, Erik, Gaurav, Jorge, Justin, Kevin, Luisana, Marcel, Michael, Patrick, Shinjan, and Yakym on my life.

I like to acknowledge the effort of my colleague, Gaurav Gupta, which contributed to Chapter 6 Numerical Modeling. The results from numerical analyses have been used here to compare with the results from experimental effort – the main focus of this dissertation.

Thank you to all of the MAE faculty and staff. I would like to thank Lynn Grabenhorst, in particular, for all she has done during the past seven years - she was always there when I needed help. I met many great people during my time at UCF. They made Orlando, Florida, a better place to be and helped make it feel like home.

Without the support of my parents, Nizar and Suhair, I would not be where I am today. They taught me the importance of education and giving back. My siblings, Mohammad and Samar, who were always there for me. A final thank you to Amo Adnan, Amo Omar and Teta for all your love and support.

TABLE OF CONTENTS

LIST OF FIGURES

LIST OF TABLES

LIST OF NOMENCLATURE

A	Area [m^2]
c_p	Specific heat capacity at constant pressure [k$J/kg\ K$]
c_v	Specific heat capacity at constant volume [k$J/kg\ K$]
D	Diameter [mm]
E	Eccentricity between the centers of jet and pimple/dimple [mm]
h	Convective heat transfer coefficient [$W/m^2.K$]
Hz	Of frequency [Hz]
i	Specific enthalpy [kJ/kg]
k	Thermal conductivity [$W/m.K$]
L	Orifice thickness [mm]
$\dot{m}$	Mass flow rate [kg/s]
n	Number (of) [-]
Nu	Nusselt number (h.$D_{av,j}$/k_{film}) [-]
P	Pressure [Pa]
Pwr	Power [W]
Pr	Prandtl number (c_p. μ/k_{film}) [-]
Q	Heat added [W], [kJ/kg] for specific heat added
Q''	Heat flux [W/m^2]

R	Result function
R	Gas constant
R^2, r^2	Coefficient of determination
Res	Resistance [Ω]
Re	Reynold number ($4.\dot{m}/(\pi. D_{av,j}.\mu)$) [-]
S	Entropy [*J/K*]
t	Pimple or dimple distance from surface [*mm*]
T	Temperature [*K*]
th	Thickness [*mm*]
V	Voltage [V]
W	Specific Work done or added (by turbine or compressor) [*kJ/kg*] (Ch. 1,2)
W	Width [mm] (in rest of chapters)
X	Streamwise jet-to-jet distance [*mm*]
Y	Spanwise jet-to-jet distance [*mm*]
Z	Jet plate-to-target wall distance [*mm*]

Greek Symbols

ε	Emissivity [-]
$\eta_{Brayton,\ ideal}$	Thermal efficiency of Brayton cycle [-]

γ	Specific heat ratio (c_P/c_v) [-]
μ	Dynamic viscosity of air [$N.s/m^2$]
Ω	Electric resistance [*Ohms*]
σ	Standard deviation, Stefan-Boltzmann constant [5.67×10^{-8} W/m^2.K^4]

Superscripts and Subscripts

1, 2, ..i	Process number
amb	Ambient
av	Averaged value
c	Compressor
cop	Copper
d	Dimple (imprint)
f, flat	Flat plate
film	at film, right above the surface
$i \rightarrow j$	From process (i) to process (j)
in	Input
ins	Insulation, in reference to Rohacell ®
j	Jet
kap	Kapton ®

net	Total
out	Output
p	Pimple (Protrusion)
pl	Plenum
rad	Radiation
ref	Reference, value at film
s	Surface
T	Turbine
tot	Total
vent	Venturi

Acronyms

AC	Alternating Current
AM	Additive Manufacturing
ANSI	American National Standards Institute
ASME	American Society of Mechanical Engineers
CAD	Computer Aided Design
CFD	Computational Fluid Dynamics
IR	Infrared

NPR	Negative Poisson Ratio
OEM	Original Equipment Manufacturer
PIV	Particle Image Velocimetry
PR	Pressure ratio
RANS	Reynolds Averaged Navier-Stokes
RH	Relative humidity [-]
RKE	Realizable κ–ε
TBC	Thermal Barrier Coatings
TC	Thermocouple
TIT	Turbine Inlet Temperature
TKE	Turbulence Kinetic Energy
TLC	Transient Liquid Crystal
VariAC	Variable AC Current Supply

CHAPTER 1:   INTRODUCTION

In this chapter, a brief coverage and overview of a modern gas turbine that includes design consideration, operation, and cooling techniques are presented. During the later section of this chapter, more in-depth coverage of the turbine blade's internal cooling techniques as a critical parameter to achieving higher thermal efficiencies is elaborated on, followed by an outline of the remaining chapters.

Background

Today, humanity is living in an era where (1) energy availability, (2) connectivity, and (3) rapid movement of goods, services, and people are a significant driver of a strong economy. The development and improvement of engines and machinery, especially in the past few decades, have had a direct impact on two out of the three drivers abovementioned.

In the 21st century, the world is challenged to keep up with the increasing demand for power. Turbomachinery Original Equipment Manufacturers (OEMs) are also facing the demands of a constantly changing climate and governmental regulations on emissions. OEMs are attempting to reduce the carbon emissions of their products and improve the overall efficiency while complying with governmental strict standards and restrictions. These, in turn, are the drives OEMs spend a considerable amount of time and

money on research and development (R&D) to invest in a cleaner, higher-efficient engines.

The increase in electric generating capacity is expected to increase over the foreseeable course of at least three decades. This increase directly reflects on the market share of turbines (gas and steam). Figure 1 shows the expected electric capacity between the years 2020 and 2050 in the United States. From the trends, it is apparent that the dependency on certain fossil fuels such as oil and natural gas, coal, and nuclear reactors are on a relatively low decline. However, this trend is opposite for the combined cycle and combustion turbine/diesel. For the former, it is forecasted that the increase in electric generating capacity will be around 60%. The latter, on the other hand, is expected to increase by ~ 218%. One thing in common between these two is the utilization of turbines.
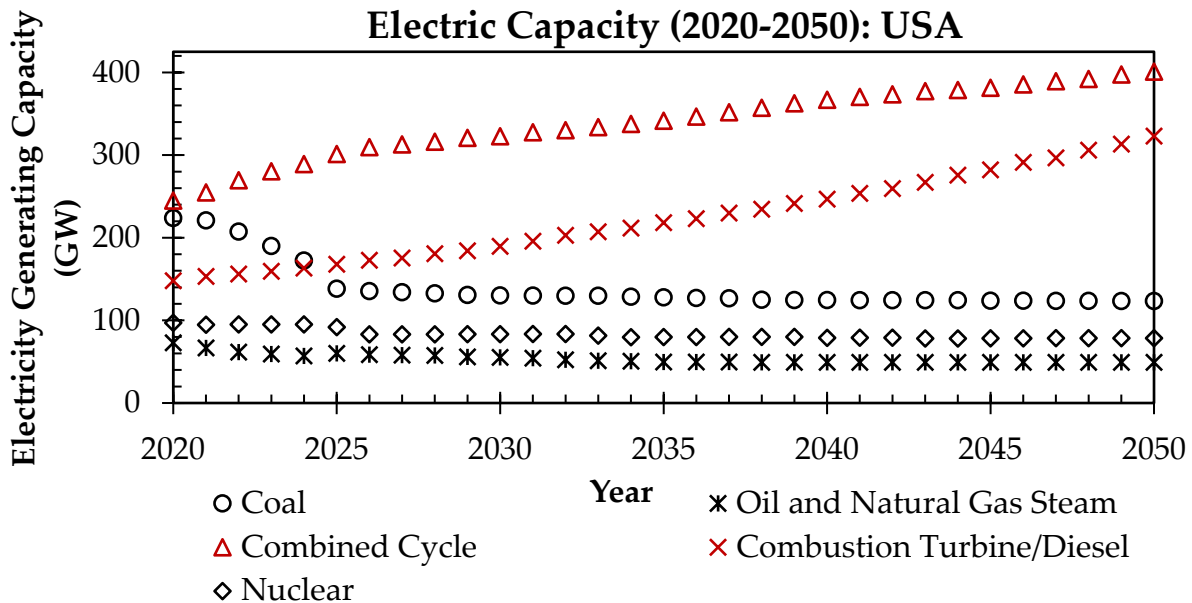
Figure 1: Estimated Annual Electricity Generation. Table A9 [1]

Many governments are providing for financial incentives and tax deductions for investors and entities that switch to alternative renewable sources of energy, often in the form of subsidies or feed tariffs [2-4]. However, and in a standard no-storage configuration, the dependency and reliability of sources of energy from solar photovoltaics and wind turbines require a continuous, uninterrupted supply of the sunlight and wind, respectively. While many would appreciate imposing as little strain as possible on the earth's ecological system, humanity seems to be at least a few decades from switching away from fossil fuels. As we stand today, aviation and power generation sectors are far from being 100% renewable, as this switch compromises the operational stability and reliability.

To put a final remark to the background section into perspective: turbines have been used for the two primary reasons in the past few decades; power generation and aviation. The cumulative improvements in the designs and operation added over these years are moving in the right direction. Particularly in the past decade, more research papers are covering exergy analysis of gas turbines, which is an essential tool for performance evaluation and enhancement assessment, than ever before [5].– More improvement can be made, and the peak of enhancement and increasing efficiency and reliability of these machines is yet to come, as the methodologies and techniques explained in the next sections will show

Gas Turbines

Gas turbines are cyclic heat engines derived from the Internal Combustion Engine (ICE) family. A gas turbine (for power generation) is shown in Figure 2. These engines are used in air-based applications as in most of the commercial airliners, and in land-based applications such as military equipment and power generation. Turbines are also found on the water in marine applications [6]. In a > $42 billion global industry, around 65% of the manufactured gas turbine engines are sold to aviation companies, while the rest are sold for power generation purposes, and this number is expected to grow further to cope up with the demand[7]. In other words, gas turbines make up for the workhorse that supplies energy to move and power billions of houses and industries around the globe with ~ 25% of all electricity in the United States and ~ 20% globally [8].
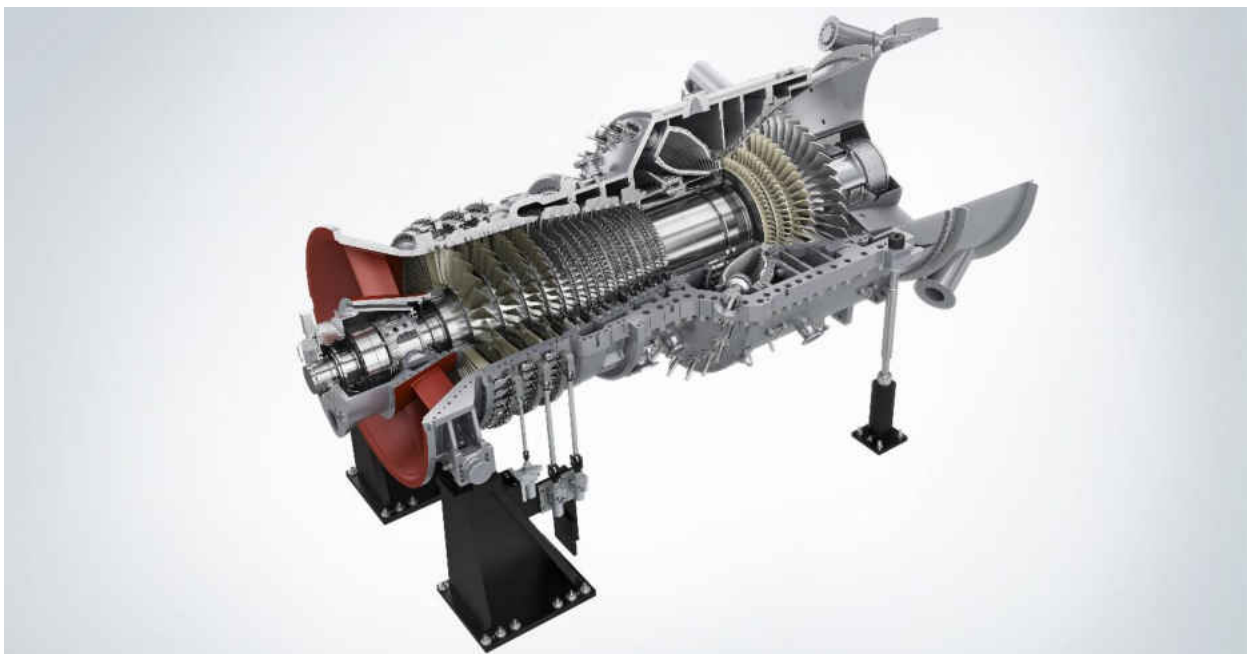
Figure 2: Siemens SGT5-4000F (Copyright Siemens AG. With permission.)

These cyclic engines are known to produce high specific power (energy per unit mass) and are considered a major player and key to powering the century. In terms of scaling, gas turbines are available in various sizes, depending on the application. Micro-turbines (referring to a miniature) are capable of producing power at a smaller scale, providing for as little as 30 kW. These smaller turbines are typically seen in remote locations or laboratories and are very useful in demonstrating out-of-classroom experiments [9]. Figure 3 shows an example of a micro-turbine for power generation that runs on Hydrocarbon gas mixtures. With the availability and readiness of the state-of-the-art additive manufacturing (AM) technologies, micro-turbines will have a promising future and a wide range of applications.

Figure 3: Cutaway of Capstone Model C30 (Courtesy: Capstone Turbine Corporation. With permission.)

Larger scale gas turbines are the industrial-sized ones used for power generation. These typically produce power of 100 to 400 MW, with a thermal efficiency of 35 – 40% in standalone operation. When functioning in a combined cycle, the thermal efficiency can reach higher efficiencies of 55%-60%. As of early 2020, the General Electric (GE 7HA) power generation gas turbine has been holding the world record from 2018, with a gross efficiency of 63.08% based on a combined cycle operation [10].

While the design requirements for power generation and aviation turbines are different, the aviation turbine needs to satisfy the specific size, mass, and high cyclic loading requirements, which are not as a strict requirement in land-based turbines.

Theory of Operation and Thermal Efficiency

It is necessary to distinguish between the "Turbine" of the gas turbine and the gas turbine itself. The former is a major component of the latter. The three major components to a gas turbine can be given by compressor with multiple stages, fuel/air combustion chamber, and a turbine to extract the energy, typically with a lower number of stages compared to the compressor. Figure 4 shows the three major components in a gas turbine. Flow direction is left to right here, starting with the first compressor stage, and ending with the last stage of the turbine.
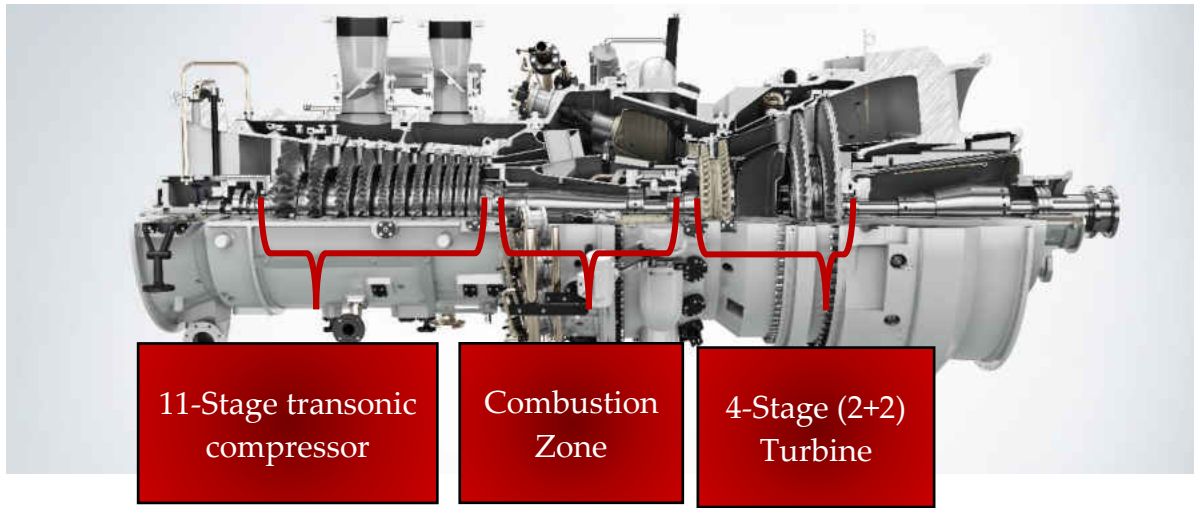
Figure 4: Siemens SGT-700 (Copyright Siemens AG. With permission.)

Named after George Brayton, the thermodynamic cycle of the gas turbines was proposed in the 19th century. An ideal Brayton cycle operates based on constant pressure processes (pressure isobars) that include heat addition and heat rejection, while other air-breathing engines operating on Otto cycle, for example, work based on the constant volume processes. In an ideal Brayton cycle, air enters the inlet of the compressor, where it undergoes isentropic compression as the air passes multiple stages of compression (rotors and stators). When at the design pressure ratio (PR), pressurized air enters the combustion chamber, and the heat addition process takes place at a constant pressure. Note that the heat addition could be direct combustion or heating through an external source. Expansion of the combusted (heated) working fluid in the turbine section provides enough energy to rotate the turbine, and also to drive the compressor through

one or multiple connected shafts, which turn the electric generator. To summarize, the four processes characterizing the ideal Brayton cycle are given by:

- 1→2:   Isentropic Compression

Isentropic compression is the first process in a turbomachinery cycle. Typically, a combination of low and high-pressure multi-stage-compressor for aviation engines and eleven to fourteen stages for power generation engines. The number of stages and modes of connectivity between the compressor and the turbine varies by OEM. The work addition to the fluid by the compressor can be written in terms of the difference between the specific enthalpy in Equation (1-1), such that:

$$W_c = W_{1\rightarrow2} = c_p(T_2\text{-}T_1) = (i_2\text{-}i_1) \tag{1-1}$$

Where

$W_c, W_{1\rightarrow2}$ Compressor work input between processes 1 to 2 [kJ/kg]

c_p Specific heat capacity at constant pressure [kJ/kg .K]

$T_{1,2}$ Compressor temperature at (1: inlet, 2: outlet) [K]

$i_{1,2}$ Specific enthalpy at (1: inlet, 2: outlet) [kJ/kg]

- 2→3:   Constant Pressure Heat Addition

After the air has been compressed, heat is added through the combustion of fuel and compressed air, or heat is added in a non-conventional mean. This process ideally occurs at constant pressure, and the heat addition is given by Equation (1-2).

$$Q_{in} = Q_{2\rightarrow3} = c_p(T_3 - T_2) = (i_3 - i_2) \tag{1-2}$$

Where

$Q_{in}, Q_{2\rightarrow3}$ Heat per unit mass added between processes 2 and 3 [kJ/kg]

- 3→4:   Isentropic Expansion

During this isentropic process, the turbine extracts and converts the energy from the working fluid into useful mechanical energy by expanding the hot, highly pressurized fluid, leaving the turbine at lower temperature and pressure. The work is done on the fluid here, or work done by the turbine is given by Equation (1-3). The number of turbine stages in this process majorly varies by OEM. Some have three (GE vintage E and F-class), most have four and five at times (GE/Alstom/Ansaldo) [11].

$$W_T = W_{3\rightarrow4} = c_p(T_3 - T_4) = (i_3 - i_4) \tag{1-3}$$

Where

$W_T, W_{3\rightarrow4}$ Turbine work input per unit mass between processes 3 and 4 [kJ/kg]

- 4→1:   Constant Pressure Heat Rejection

In reality, and unlike in the steam turbine cycle, the gas turbine exhaust is released into the atmosphere, making the process 4 to 1 useful when examining additional components to raise the efficiency of the cycle, such as a regenerator.

In an actual form of the Brayton cycle, pressure losses happen across both the compressor and the turbine due to leakages and other aerodynamic losses. The losses, in turn, reduce the power output of the turbine, and the ideal compression ratio across the compressor decreases, and the pressure isobars due to losses diverge. Figure 5 shows a comparison between the ideal and the actual Brayton cycles. The difference between the two processes across the compressor at the turbine is due to their respective efficiency not being at unity. In order to obtain the required power output, the amount of air-to-fuel ratio is increased and adjusted accordingly. However, there are some limitations to how much air and fuel can be supplied into the system.
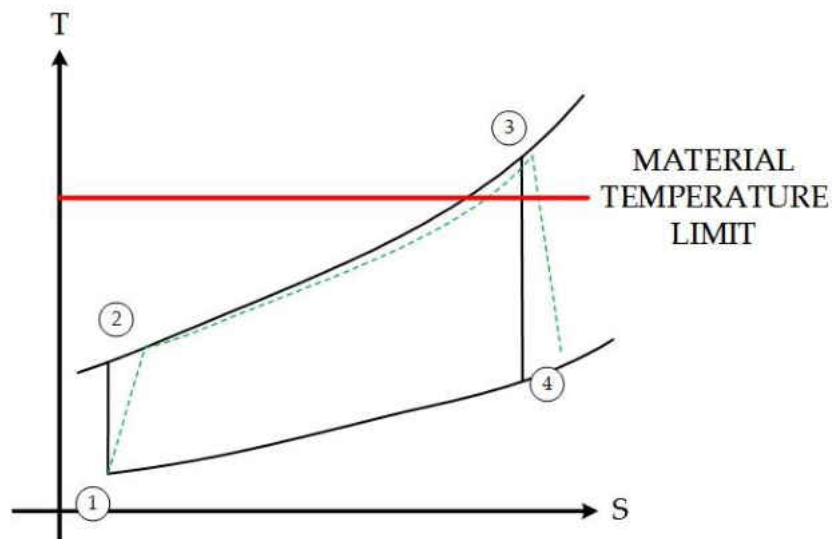
Figure 5: T-S Diagram of Brayton Cycle: Actual (Green) and Ideal (Black)

Utmost critical aspects considered in gas turbine design and performance are the thermal efficiency and the turbine-to-compressor work ratio, often referred to as the inverse back work ratio and thrust-to-weight ratio (for aviation engines). The first two depend only on two vital parameters: the ratio of turbine and compressor inlet temperatures (T_3/T_1), and the compressor pressure ratio (P_2/P_1). Equation (1-4) represents the net work done by the turbomachine, which is the difference between the work done by the turbine and the work added by the compressor in Equations (1-3) and (1-1), respectively, such that,

$$W_{net} = W_{3 \to 4} - W_{1 \to 2} = c_p \cdot (T_3 - T_4) - c_p \cdot (T_2 - T_1) \tag{1-4}$$

Where

W_{net} Specific net power output [kJ/kg]

The efficiency of the ideal Brayton cycle can be defined in Equation (1-5) as the ratio of the net work to the heat added

$$\eta_{Brayton,\,ideal} = \frac{W_{net}}{Q_{in}} = \frac{W_{net}}{Q_{2 \to 3}} = \frac{c_p \cdot (T_3 - T_4) - c_p \cdot (T_2 - T_1)}{c_p \cdot (T_3 - T_2)} \tag{1-5}$$

Where

$\eta_{Brayton,\,ideal}$ The efficiency of the ideal Brayton cycle

The isentropic relation is given by Equation (1-6)

$$\frac{T_2}{T_1} = \frac{T_3}{T_4} = PR^{\frac{\gamma-1}{\gamma}} \qquad (1-6)$$

Where

PR   Pressure ratio across the turbine or compressor in Equation (1-7)

γ Specific heat ratio in Equation (1-8)

$$PR = \frac{P_2}{P_1} = \frac{P_3}{P_4} \qquad (1-7)$$

$$\gamma = \frac{c_p}{c_v} \qquad (1-8)$$

Where

c_v Specific heat capacity at constant volume [kJ/kg .K]

With the assumption of cold air standard, the substitution of the above Equations, Equation (1-5) can then be rewritten as

$$\eta_{Brayton,\ ideal} = 1 - \frac{T_1}{T_2} = 1 - \frac{T_4}{T_3} = 1 - \frac{1}{\left(\frac{P_2}{P_1}\right)^{\frac{\gamma-1}{\gamma}}} \qquad (1-9)$$

Based on Equation (1-9), it can be seen that the simple Brayton cycle efficiency is dependent upon the <u>compression ratio</u> across the compressor or the turbine inlet temperature. However, with the current advancements in manufacturing, this temperature already exceeds the material's maximum allowable limit and pushing it further requires cooling techniques such as internal and external cooling

The second important parameter is the <u>inverse back work ratio</u> ($W_T/|W_c|$) between the turbine output and the absolute value of the compressor input. Here, the inverse back work ratio can be given by Equation (1-10).

$$\frac{W_T}{W_c} = \frac{\left(\frac{T_3}{T_1}\right)}{\left(\frac{P_2}{P_1}\right)^{\frac{\gamma-1}{\gamma}}} \tag{1-10}$$

This parameter is considered <u>useful work</u> and should be as large as possible since a large amount of the power produced by the turbine is used to drive the compressor. On one hand, this equation shows that there is an inverse proportionality between the work ratio and the pressure ratio. On the other hand, Equation (1-9) shows that the increase in thermal efficiency is related to the increase in pressure ratio. It is concluded that there is a trade-off between both variables. From the above equations, we can rewrite the net work in a non-dimensionalized form in Equation (1-11), assuming that the turbine and compressor efficiencies are ideal at 100% such that:

$$\frac{W_{net}}{c_p T_1} = \left(\frac{T_3}{T_1}\right)\left(1 - \frac{1}{\left(\frac{P_2}{P_1}\right)^{\frac{\gamma-1}{\gamma}}}\right) - \left(\left(\frac{P_2}{P_1}\right)^{\frac{\gamma-1}{\gamma}} - 1\right) \tag{1-11}$$

To visualize the effect of pressure ratio on the above equations, and under the presumption that the compressor inlet temperature (T_1), turbine inlet temperature (T_3) are constant values (here T_3/T_1 assumed at 3.5), (γ) is 1.4, Equation (1-9) and Equation

(1-11) can be plotted together as a function of pressure ratio on different y-axis scales. The trade-off abovementioned is plotted in Figure 6. Increasing the pressure ratio alone may result in a draw-back and reduction in net specific work output with an increase in thermal efficiency. Therefore, increasing the turbine inlet temperature will independently increase thermal efficiency. An increase of 55 K in the firing temperature increases the thermal efficiency by 1 – 1.5%, and the work output by ~ 10%[12].
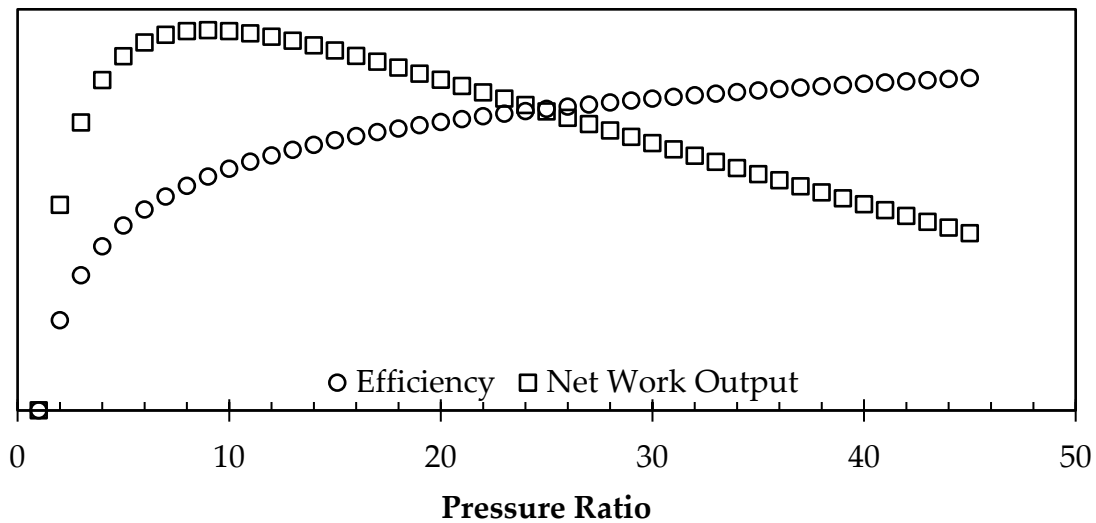
Figure 6: Specific Work Output and Thermal Efficiency

To conclude, there are some considerations to increase the overall cycle's efficiency, such as allowing for higher maximum temperature (T_3), increasing the efficiency for individual components, and modifying the basic Brayton cycle such as adding recooling, or recuperation as outlined in [13]. Since the current maximum temperatures in the cycle exceed the material's allowable limit, this could cause failure in

the turbine blades if cooling is not utilized. Many cooling techniques have been introduced to the blade to overcome material softening and failure. Advanced cooling allows for higher firing temperature capabilities while keeping the critical components protected. A portion of the compressed air gets directed towards the cooling of the blades at both internal and external levels. Even though the temperature of that compressed air at (T_2) is higher than ambient conditions (T_1), it remains lower than the maximum temperature in the cycle (T_3). Convection and impingement cooling techniques are used to cool the internals of the blades, and external cooling is utilized in the form of film cooling and potentially transpiration cooling.

Gas Turbine Cooling

In the previous section, a brief introduction to gas turbines, Brayton cycle, and operation principles were discussed. Increasing turbine efficiency by increasing the maximum operating temperature requires extensive research and testing. It was shown how a critical factor, increasing the turbine inlet temperature, is vital in stretching efficiency. Not to compromise the structural integrity of the blade, several internal and external cooling schemes can be introduced to reduce the thermal loading and increase the lifespan of the blade.

Internal Cooling

The design of internal and external turbine blade cooling is dependent upon the projected heat and mechanical load. Variations of the cooling technologies used can vary by OEM and operating conditions. However, the convective cooling inside the turbine blade is typically used in the form of two categories: (1) internal passage cooling at mid-chord, (2) impingement cooling, and (3) pin-fin cooling at the trailing edge [14]. Detailed information on the state-of-the-art internal and external cooling technologies are documented in the work of Han et al. [15]. Active internal and external cooling requires complex networks of channels and holes, as seen in Figure 7. Such internal and external geometries are complex to manufacture. Typically, cooling air flows through rib-roughened serpentine passages in a turbine blade. These rib-roughened extended surfaces act as promoters to flow mixing between the hot walls of the blade and the cooler air drawn from the compressor. After passing through the passages, air emanates through a multi-jet impingement scheme to provide for further cooling of the leading edge, which is the region where the maximum temperature an occur. On a parallel path, the air that passes through another channel is direct towards the trailing edge, which is supported by pin-fins. These extended structures are utilized to maximize mechanical strength, and also to maximize heat transfer in the trailing edge by increasing the surface

area and turbulence in the region. A portion of the coolant that passes through different

passages is directed towards tip cap cooling, as seen in Figure 7.
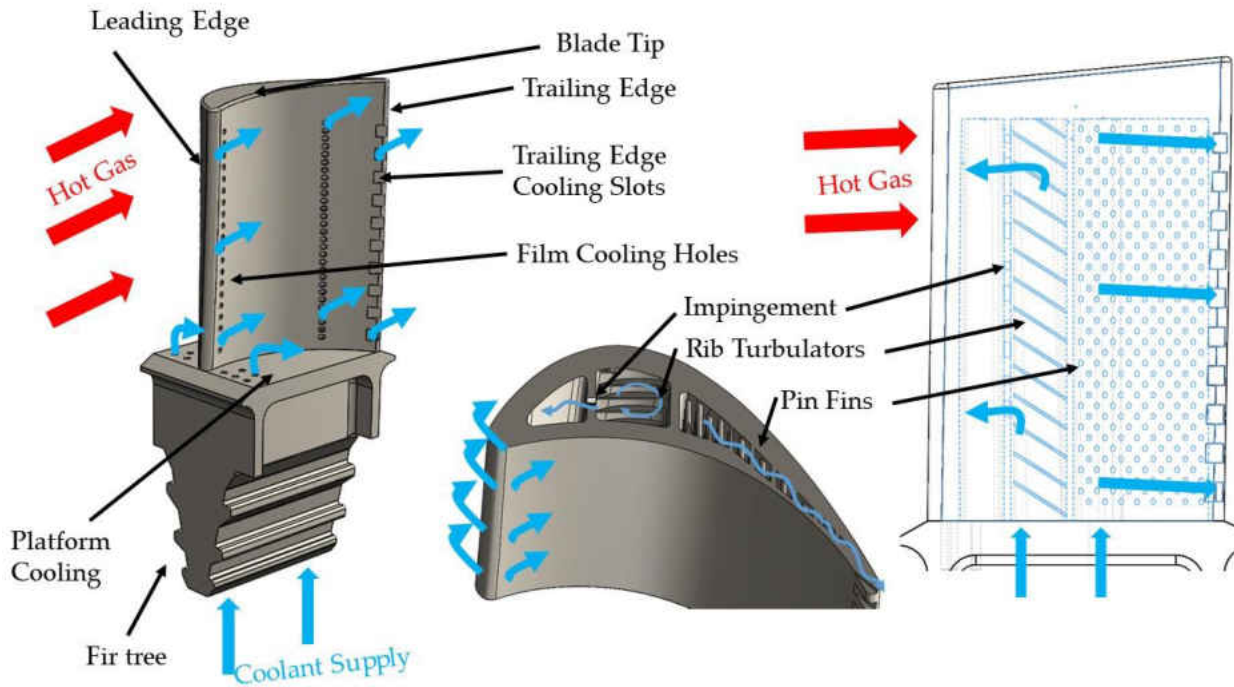
Figure 7: Schematic of Turbine Blade Cooling Passages [16]

External Cooling

Thermal Barrier Coatings (TBC) such as yttria-stabilized zirconia-based ceramic

(YSZ) and metallic bond-coat (MCrAlY) are materials applied to hot components such as

a turbine blade to protect them from the hot gases [17]. These coatings act as an insulator

and allow for an increase of (90 °C to 150 °C) in the turbine firing temperature, and thus

increase the turbine's efficiency. While these added layers of protection provide the

ability for elevated firing temperature, their thermal performance and surface roughness

are dependent upon the methodology used to coat the superalloy blades. Typically, the stages of the turbine are seen in a white/yellowish color, indicating the surfaces and often end-walls have been coated with TBCs since they experience the highest thermal loads. Refer to Figure 2 and Figure 4.

Discrete holes on the external surface of the turbine blades are meant for the coolant to be ejected on the surface, creating a colder film over the external surface in a process called film cooling. Over the past few decades, this method had helped in creating a protective layer of film between the blade and the hot gases, reducing the maximum temperature the blade is exposed to. Transpiration cooling is another technique that is of high potential to provide for better cooling. With the advancement of manufacturing techniques, the outer surface of the blade made is coated with a porous media, i.e., ceramic, allows for the cooler gasses to be ejected through the surface, creating a continuous film of cooler air. Despite being an under-development technique, this method can have the potential to yield favorable results in cooling technology [18].

As shown in Figure 8, with a combination of internal cooling, external cooling, endwall cooling, TBCs, and permeable coatings, OEMs have been able to develop machinery that can operate well beyond the allowable material temperature and thus increasing the cycle's efficiency.
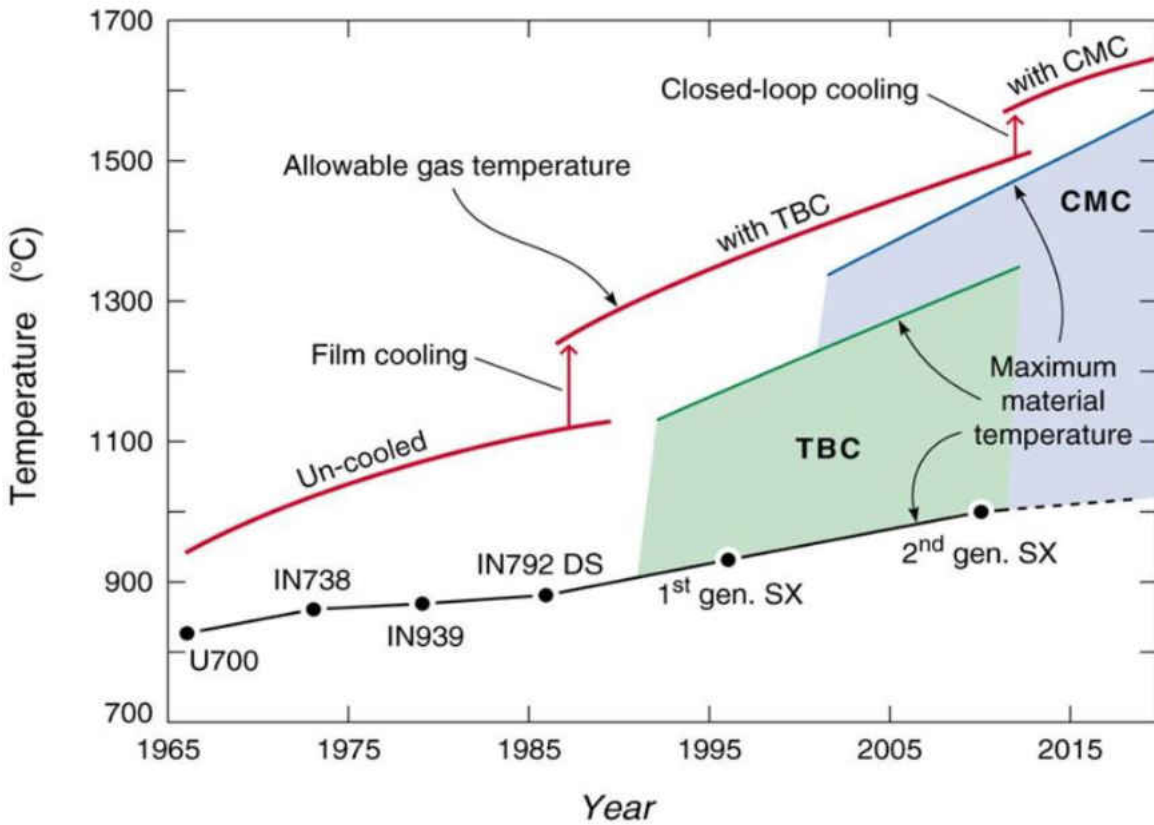
Figure 8: Gas Turbine Hot Temperature Progression of Various Materials, Cooling Techniques, and Coatings by Wadley Research Group, based on [19]and [20]

Structure and Anatomy of a Multi-Jet Scheme

With the amount of energy generated in a gas turbine, jet impingement cooling is one of the methods used to reject heat and continuously disrupt the thin boundary layer generated at a surface, which contributes to increasing the heat transfer coefficient. Air or any other cooling fluid is forced through a perforation, creating a jet that impinges on a surface (flat, curved, angled) referred to as the target surface. In turbomachinery applications, jet

impingement configurations provide a means to enhance the convective heat transfer process, yet remain challenging for this specific application. The complex geometry of the internals of the turbine blade coupled with highly turbulent flows, make understanding of flow physics and heat transfer associated with impingement jets a challenging topic [21, 22].

Since impingement cooling is highly localized in the stagnation region of the jets, this technique is considered to yield the highest heat transfer coefficients [15]. Impingement cooling is not exclusive to gas turbines, as it can be found in electronic cooling, drying of textiles and paper, and other applications [22]. In the open literature, two major types of jet impingement configurations can be found: (1) single-jet impingement and (2) an array of multi-jet impingement. Four main zones of the flow are considered for both configurations downstream the impingement orifice as can be seen in Figure 9 (right):

- Flow establishment (Potential core area)

This region extends from the nozzle of the orifice to the apex of the potential core; the region where the velocity of the jet is equal to the velocity of the inlet profile at the center. The potential core width is approximately 4.7 – 7.7 nozzle diameters for slot jets and 6 – 7 nozzle diameters for circular jets [23].

- Established flow

20

This is the region that extends from the apex of the potential core. The centerline jet velocity dissipates in this region and starts spreading in the transverse direction. Due to large interaction between the potential core and ambient, axial velocity decays in the developing zone, transferring it to the fully developed zone. The axial velocity then fades out as the jet approaches the wall boundary. In the shear layer of the impingement jet, the ambient and potential core interaction cause entrainment of energy, momentum, and mass into the core, causing the potential core region to gradually phase-out.

- Jet deflection regions (Stagnation region area)

- Wall jet region
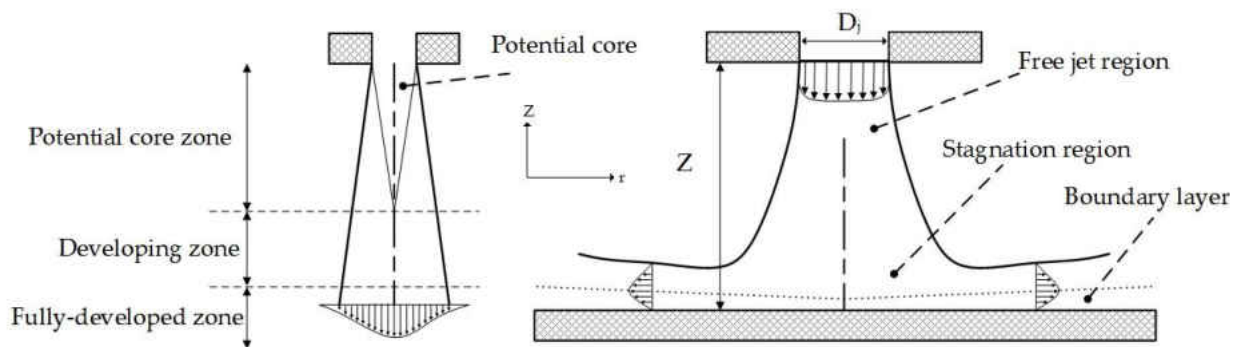
Figure 9: Free Jet (Left), Impinging Jet (Right)

The flow field for multiple jets is similar to a single jet configuration. However, there are two significant differences; jet-to-jet interaction between adjacent jets pre-impingement

and interactions post-impingement due to a collision of the jet with the opposing target wall. The former occurs from shear layer expansion for nearby stream or spanwise jet-to-jet spacing (X/D_j), (Y/D_j), and sizeable jet-to-wall spacing (Z/D_j). The latter, on the other hand, enhances boundary layer separation and promotes turbulence at high jet velocities and smaller jet-to-jet spacings. During this interaction, an up-wash fountain develops between two jets and forms recirculation, as can be seen in Figure 10.
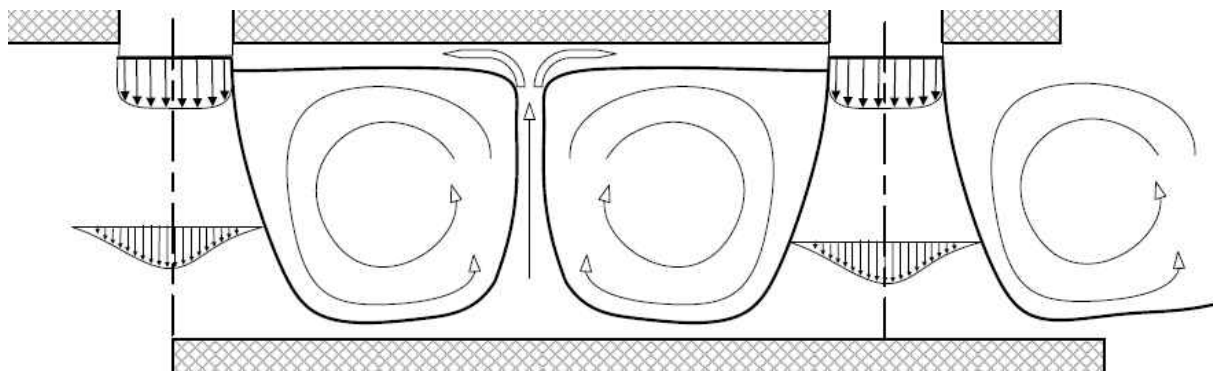
Figure 10: Flow Pattern and Interaction between Two Jets

A relevant term to identify is jet crossflow, the interaction of one jet with the surrounding spent fluid flowing across from the orifice. The interactions mentioned previously in this section are further emphasized and can appear more dominant with crossflow effects. Interactions of crossflow in their three forms (minimum, partial, complete) were extensively studied, and a wide range of publications can be found on the topic, some examples are to be found in [24-28].

Dissertation Organization

In CHAPTER 2:, the importance of cooling gas turbines is briefly discussed, paving the way for an introduction of various cooling techniques. Then narrowing the general topic down to impingement cooling and its role in maximizing the heat transfer in turbine blades.

An introduction to multi-jet impingement cooling in literature is also discussed, describing the notable work done by many researchers. The review based on previous studies is summarized for various testing parameters and conditions used. Another review based on impingement on non-flat surfaces, including a combination of pimples, dimples, cusps are presented follower by a summary of the studies found in the literature.

The motivation behind this work, objective, the novelty of the current work, and plate configurations are presented in CHAPTER 3:.

CHAPTER 4: discusses the description of the experimental work. What was used, why it was used, and how it was used. Detailed analysis of the heat transfer, data reduction, and an introduction to the 2-method testing procedure is presented. The schematics of the test section, two impingement plates used in this study, are also introduced in this chapter.

The methods and statistical tools used to find the total uncertainty are discussed in CHAPTER 5:, with an emphasis on the methodologies developed and been used by

the American Society of Mechanical Engineers (ASME) and the American National Standards and Institute (ANSI).

CHAPTER 6: Discusses the numerical techniques used to compare the experimental heat transfer study, along with some details on the various turbulence models used for comparison.

CHAPTER 7: gives a brief introduction to the statistical methods used to build correlations. These were based on multi variable logarithmic regression that gives the best approximation for the type of data collected in this study.

The heat transfer results and comparisons are presented in CHAPTER 8:. Validation of the baseline model against literature is shown. Then the heat transfer data for the impingement plates used are discussed, followed by sufficient explanations and reasonings behind the observed results. A comparison of the results from both plate configurations is presented herein.

CHAPTER 9: is the results section based on the methodology and approach presented in CHAPTER 7:. Here, the correlations developed are compared against the data available from open literature shown in CHAPTER 2: and against the experimental data. Error due to data fitting and modeling is also discussed.

Finally, CHAPTER 10: ends this work with concluding remarks, findings, and suggestions for future work.

CHAPTER 2:   LITERATURE REVIEW

Gas turbine performance has been improving over the past few decades, due to substantial improvement in technologies that led to an increase in the turbine inlet temperature (TIT) and compression ratios (PR). The improved temperature performance is higher than ever before, due to the advancements made in material sciences and the development of composite materials such as TBCs. Moreover, internal and external cooling technologies have come a far way in keeping the turbine blades and other critical hot components as cool as possible.

Enhancements in the turbine cooling scheme become vital when considering increasing the heat transfer efficiency as the maximum temperature the blade is exposed to well exceeds the material limitation. Thus, cooling using various techniques such as film cooling and jet impingement cooling assures safe, and long-lasting operation under extreme thermo-mechanical loading conditions.

Jet impingement as a method for turbine blade leading edge cooling is effective and provides for high heat transfer rejection from the surface. The impingement as a cooling technique has been studied extensively and is commonly used to cool hot components such as in combustor liners and leading edges of the turbine blade [29]. Single jet impingement has been extensively studied over the past decades, including the effects of confinement and other techniques to improve the performance of conventional

impingement jets [30-32]. These improvements can consist of means to increase the heat transfer surface, such as adding solid extrusions like rib-turbulators, pin-fins, surface rougheners, and also modifications to the jet, such as unsteady or fluidic oscillators [33-36]. However, certain extrusions and modifications were found to cause substantial nonuniformity in the flow field, increase thermal stress, and induce a significant pressure loss that leads to higher compressor load and reduction of turbine useful work [37].

Jet Impingement: Nomenclature

The current investigation focuses on determining heat transfer behavior for an array of jets with uniformly spaced configuration. To introduce necessary parameters needed in subsequent sections, Figure 11 shows typical nomenclature for a jet impingement plate. Often, these parameters are used in a non-dimensionalized fashion with respect to the jet diameter (D_j).
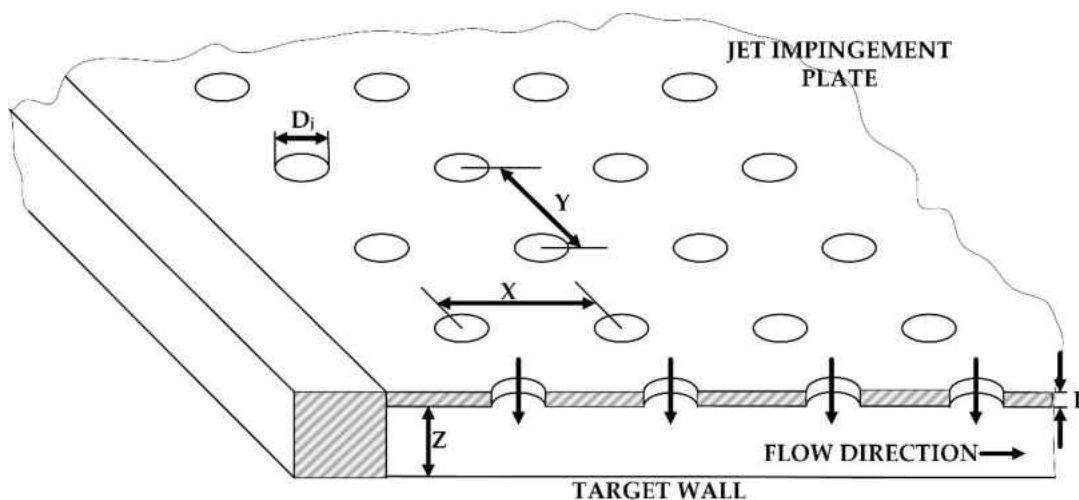
Figure 11: Nomenclature of Impingement Testing Plate

Where

D_j   Jet diameter [mm]

L   Jet plate thickness [mm]

X   Jet-to-jet distance (streamwise) [mm]

Y   Jet-to-jet distance (spanwise) [mm]

Z   Jet-to-target wall distance [mm]

Figure 12 shows the necessary nomenclature used for studies in Table 2, in configurations where the target surface is a non-flat wall, i.e., pimples or dimples, four more parameters than those shown in Figure 11 are used. The details on the geometry used for this study is shown in Figure 16 and Figure 18.

Figure 12: Nomenclature of Studies Shown in Table 2

Where

D_d   Diameter of the sphere used to imprint on the target wall [mm]

D_p Diameter of the sphere used to create the pimple [mm]

t_d Thickness of the sphere imprint on the target wall [mm]

t_p Thickness of the sphere extruding from the target wall [mm]

Multi-jet Impingement

Studies on the heat transfer characteristics and flow fields in multiple jet array impingement configurations have included effects on multiple geometric parameters, such as jet-to-jet spacing (X/D_j, Y/D_j), orifice diameters (D_j), and also with various flow configuration (minimum, partial, complete) crossflow. A vast number of studies have been summarized and analyzed in the review of Wiegand and Spring [38]. Their review includes a detailed discussion of the aspects that affect heat transfer. Such aspects include the effects of jet-to-jet interactions, crossflow configuration, and the effects of jet-to-target wall distance on flow separation. Table 1 summarizes some studies that focus on array impinging jets, covering a wide variety of parameters, including jet-averaged Reynolds number ($Re_{av,j}$), the jet array configuration, jet-to-jet spacings (X/D_j, Y/D_j), jet-to-target wall spacing (Z/D_j). The table is a reference and can be used as a highlight of related studies and to complement the scope of this work. The flat plate impingement of this study is included at the end of the table, in field number 26.

Table 1: Summary of Jet Impingement Array

No.	Author(s)	Array configuration	$Re_{av,j}$	X/D_j	Y/D_j	Z/D_j	Remarks	Ref.
1.	Andrews	-	$1{,}000 - 65{,}000$	$5 - 10$	$4 - 8$	$1 - 3$	-	[39]
2.	Katti and Prabhu		$3{,}000 - 7{,}000$	$3 - 5$	5	$1 - 3$	-	[40]
3.	Hollworth and Berry		$3{,}000 - 35{,}000$	$10 - 25$	$10 - 25$	$1 - 25$	-	[41]
4.	Geers et al.		$5{,}000 - 20{,}000$	-	$2 - 6$	$3 - 10$	Flow examination CFD comparison	[42]
5.	Park et al.		$5{,}000 - 20{,}000$	$2 - 10$	$2 - 10$	$1, 2, 5$	-	[43]
6.	Yong et al.		$5{,}000 - 25{,}000$	$2 - 5$	$2 - 5$	$2 - 4$	-	[44]
7.	Metzger et al.		$5{,}000 - 25{,}000$	10	$8 - 10$	$1 - 3$	-	[28]
8.	Florschuetz et al.		$5{,}000 - 70{,}000$	$5 - 15$	$4 - 8$	$1 - 3$	-	[45]
9.	Lee et al.	Complete	$8{,}000$	$5, 8, 12$	$5, 8, 12$	$1.5 - 8$	-	[46]
10.	Lee et al.		$8{,}000 - 50{,}000$	$5, 8, 12$	$5, 8, 12$	$1.5 - 8$	-	[47]
11.	Goodro et al.		$8{,}200 - 30{,}500$	$8, 12$	$8, 12$	3	-	[48]
12.	Dano et al.		$8{,}500 - 15{,}900$	-	-	$2 - 4$	Flow examination	[49]
13.	Chi et al.		$10{,}000 - 30{,}000$	4	8	3	CFD comparison	[50]
14.	Fechter et al.		$10{,}000 - 40{,}000$	5	5	$1 - 3$	CFD comparison	[51]
15.	Van Treuren et al.		$10{,}000 - 40{,}000$	8	8	1	-	[52]
16.	Ricklick and Kapat		$17{,}000 - 45{,}000$	5	4	$1, 3$	-	[53]
17.	Son et al.		$19{,}500 - 29{,}500$	$3 - 4.8$	$3.75 - 6$	$1.875 - 3$	-	[54]
18.	Esposito et al.		$20{,}000 - 60{,}000$	5	5	$3 - 6$	-	[55]
19.	Kercher and Tabakoff	Minimum Complete	$300 - 30{,}000$	$3.1 - 12.5$	$3.1 - 12.5$	$1 - 4.8$	-	[56]

No.	Author(s)	Array configuration	Re_j	X/D_j	Y/D_j	Z/D_j	Remarks	Ref.
20.	Huang et al.	Partial Complete	4,800 – 18,300	4	4	3	-	[57]
21.	Azad et al.	Partial	4,850 – 18,300	2.54	2.54	3	-	[58]
22.	Yan et al.	Complete	1,500 – 4,500	6	3	3 – 9	Rib-roughened walls	[59]
23.	Obot and Trabold	Minimum	1,000 – 21,000	10	10	4.5	-	[60, 61]
24.	Spring et al.	Partial Complete	17,000 – 34,000	5	5	3 – 5	-	[62]
25.	Xing et al.		17,000 – 34,000	5	5	3 – 5	-	[63]
26.	**This study**	**Complete**	**5,000 – 9,000**	**7.16**	**7.16**	**2.4, 2.87, 3.25, 4, 6**	**This study, comparison to a pimple-dimple plate**	**-**

Pimple-Dimple Impingement

Many studies focused on the investigation of heat transfer, fluid flow, and pressure drop for different flow confinement configurations as well as crossflow schemes. These include impinging on pimples, dimples, cusps or a combination of them.

Xie et al. [64] numerically evaluated a single jet impingement over a dimple, and combined that with a Particle Image Velocimetry (PIV) study for various jet plate configurations ($Re_{av,j}$ = 5,000 – 23,000, D_j/D_d = 0.318, 0.50 and 1.045, t/D_d = 0.10, 0.20 and 0.30, Z/D_j = 2). They found that the average heat transfer increases with the increase of dimple depth.

Sriromreun and Sriromreun [65] numerically and experimentally investigated the heat transfer characteristics on a cylindrical dimpled surface ($Re_{av,j}$ = 1,500 – 14,600, D_j/D_d = 0.50 and 1, t/D_d = 0.50, and Z/D_j = 2, 4 and 6). They found the highest thermal enhancement to be at the lower dimple diameter and a radial dimple distance of ($2 \times D_j$). Their results also agreed with many, that this enhancement came at the lowest (Z/D_j) case of ($2 \times D_j$).

One of the latest studies was made using a (3×3) array of jets and investigated by Vinze et al. [66] ($Re_{av,j}$ = 5,000 – 40,000, D_j/D_d = 0.25 and 0.50, t/D_d = 0.25, 0.50, and Z/D_j = 1 - 6). They concluded that the highest pitch yielded the maximum averaged heat transfer.

Xing and Weigand [67] investigated the heat transfer and friction of an inline array of jets on dimpled surfaces ($Re_{av,j}$ = 15,000 – 35,000, D_j/D_d = 0.556, t/D_d = 0.15, and Z/D_j = 3, 4 and 5) . They concluded that the lowest (Z/D_j) yielded the highest heat transfer and at minimum crossflow.

Azad et al. [68] carried out experiments of heat transfer on two different hemispherical dimpled target surfaces (23 x 9) and (11 x 5) dimples, using an array of (12 x 4) inline jets of air using the transient liquid crystal (TLC) technique with three crossflow configurations ($Re_{av,j}$ = 4,850 – 18,300 , D_j/D_d = 1, t/D_d = 0.5, and Z/D_j = 3). They concluded that a positive effect on heat transfer is seen with the increase of the number of dimples.

Chang et al. [69, 70] studied heat transfer, with and without effusion, of (4 x 3) impingement jets onto two surfaces with dimples, and dimples/protrusions using an IR camera ($Re_{av,j}$ = 5,000 – 15,000, D_j/D_d = 0.25, t/D_d = 0.25 and 0.875, and Z/D_j = 0.50 - 11, eccentricity-to-jet diameter (E/D_j) = 0, 3 and 6). Testing results showed that the highest Nusselt number is at its maximum for an (E/D_j) of 6. Their work concluded that increasing the Z/D_j reduces the heat transfer between effusion and non-effusion for both dimples and protrusions.

Ekkad and Kontrovitz [71] performed a similar study using TLC, on jets impinging on a dimpled surface with inline and staggered configurations ($Re_{av,j}$ = 4,800 – 14,800 ,

$D_j/D_d = 0.50$, $t/D_d = 0.125 – 0.25$, and $Z/D_j = 3$). They varied the dimple location and depth. They concluded that the increase of crossflow increases the heat transfer coefficient, and deeper dimples provide a higher heat transfer coefficient for both jet configurations.

In multiple publications, Kanokjaruvijit and Martinez-Botas [72-75] carried out experimental studies of multiple jets impinging on flat portions then centers of dimpled and cusped elliptical surfaces in three crossflow configurations; maximum, intermediate and minimum ($Re_{av,j} = 5,000 – 11,500$, $D_j/D_d = 0.25 – 1.15$, $t/D_d = 0.15, 0.2$, and $Z/D_j = 1 - 12$). The results from all their previous work were summarized into parametric correlations and are presented in [75]. Over the range of their work, highlights from their conclusions are:

- Hemispherical and cusped elliptical dimples did not perform much differently in terms of heat transfer with a slight favor to the hemispherical ones.

- Impingement on flat portions yielded higher heat transfer than when impinging on shallow dimples while impinging on deep dimples yielded higher heat transfer when comparing to impinging on flat only.

- Maximum crossflow configuration yielded higher pressure loss compared to intermediate and minimum ones.

- (c) When comparing (Nu_d/Nu_{flat}), minimum and intermediate crossflow reduces heat transfer values for all tested Z/D_j values except 2 while maximum crossflow demonstrated to be the best performing for (Z/D_j) = 4 and 8.

Kim and Kim [76] numerically evaluated the heat transfer performance of combinations of dimple/protrusions at laminar flow conditions, for both staggered and inline configurations ($Re_{av,j}$ = 80, D_j/D_d = 0.25 – 0.143, t/D_p = 0.20 – 1.60, and Z/D_j = 9). Their work showed that a staggered configuration on dimples yields the best heat transfer, while staggered protrusions yield the lowest pressure drop.

Summary of the previous studies involving impingement on pimple, dimple, cusps or combination of these is shown in Table 2.

Table 2: Summary of Impingement on Pimpled, Dimpled or Cusped Surfaces

No.	Jet configuration	Feature	Re_j	D_j/D_d	$t/D_{d/p}$	Z/D_j	X/D_j, Y/D_j	Method	Remarks	Ref.
↓↓↓Impingement on Pimples and/or Dimples↓↓↓										
1.	Single jet	1 Dimple	5,000 – 23,000	0.318 0.5 1.045	0.10 0.20 0.30	2	-	PIV CFD	Circumferential configuration	[64]
2.	Circumferential		1,500 – 14,600	0.50, 1	0.50	2, 4, 6	*	TCs CFD	* 2, 3 D_d in radius * 1.5, 3 D_d in circumference	[65]
3.	Inline		5,000 – 40,000	0.25, 0.50	0.25, 0.50	1 - 6	3, 4, 5	IR	Eccentricity (e = 0, 0.5 D_d)	[66]
4.	Inline	Dimples	15,000 – 35,000	0.556	0.15	3, 4, 5	5	TLC	Three crossflow orientations	[67]
5.	Inline		4,850 – 18,300	1	0.5	3	4	TLC	Three crossflow orientations	[68]
6.	Inline		5,000 – 15,000	0.25	0.875	0.5 - 11	4	IR	Eccentricity (E/ D_j = 0, 3, 6)	[69]
7.	Inline Staggered		4,800 – 14,800	0.50	0.125 0.25	3	4	TLC	-	[71]
8.	Staggered	Dimples Cusps	11,000	0.59	0.289	2, 4, 8	3.91	TLC	Hemispherical and elliptical shapes; three crossflow orientations	[72]
9.	Staggered		11,500	0.59	0.294	2, 4, 8	3.99	TLC	Three crossflow orientations	[73]

No.	Jet configuration		Re$_j$	D$_j$/D$_{d/p}$	t/D$_{d/p}$	Z/D$_j$	X/D$_j$, Y/D$_j$	Method	Remarks	Ref.
10.	Inline	Dimples Cusps	11,500 5,000 – 11,500 11,500 11,500	0.578 0.50 0.25 1.15	0.29 0.15, 0.25 0.15, 0.25 0.29	2, 4, 8, 12 1-8 2, 4 2, 4	5.02 6 & 10 6 & 10 5.02	TLC	Three crossflow orientations	[74]
11.	Inline		5,000 – 15,000	0.25	0.25	0.5 – 10	4	IR	Eccentricity (E/ D$_j$ = 0, 3, 6)	[70]
12.	Inline	Dimples	5,000 – 11,500	0.25 0.50 1.15	0.15 0.25 0.29	2, 4, 8, 12	4	TLC	Correlations built based of [72-74]	[75]
13.	Inline Staggered	Pimples Dimples	80	0.25 – 0.143	0.20 – 1.6	9	8	CFD	Laminar flow Compared CFD with experiment	[76]
↓↓↓Impingement from Pimple-dimpled Plate↓↓↓										
14.	Staggered pimples and dimples	Pimples Dimples	5,000, 7,000, 9,000	P:0.07 D:0.14	P:2.78 D:1.28	2.4 2.87 3.25 4 6	7.16	HT CFD	This study, compared with flat plate	

36

Summary

Several studies exist where the focus on the heat transfer, pressure drop, and overall performance of impinging on a non-flat surface, namely, semi-spheres. Referring to the relevant investigations above and the summary in Table 2, vast majority of the work shows that impinging on pimples, dimples, and cusps yields a higher heat transfer coefficient that when compared to a flat target surface

While some studies focused on impingement on dimples and protrusions, the conclusion drawn from the literature survey is that no previous studies have involved impingement from a non-flat surface. Alternatively, to be more specific, no combination of circular jet impingement array emanating from such shapes have been found in the literature.

The current study focuses on investigating the heat transfer aspects of an array of circular-shaped impinging jets emanating from a pimple-dimpled plate, which is arranged to have negative Poisson ratio auxetic properties when microscopically loaded. The target wall, opposite of the pimple-dimpled plate, is flat. Moreover, statistical methods are employed in this study, and correlations for the flat and pimple-dimpled plate are presented herein.

CHAPTER 3:   MOTIVATION, OBJECTIVES, AND NOVELTY

CHAPTER 2: introduced the jet array impingement and followed the discussion by a summary of the literature based on impingement on flat surfaces using a flat plate as well as impingement on pimples, dimples, and cusped surfaces from a flat plate. The work herein introduces jet impingement emanating from a non-flat plate. Motivation, background, objectives, and novelty of this work are discussed in detail in this chapter.

Background on the Unique NPR Structures

Turbine components such as the combustion liners and turbine blades undergo thermal expansion and massive stresses due to the elevated temperatures they are exposed to. Hot components made of metals, ceramics, or composites undergo material fatigue, and that can be a major cause of failure. Advancements in materials science and additive manufacturing allow for the innovation of new and sophisticated designs of such components. The use of auxetic geometries can provide for fracture resistance and higher energy absorption, which enables for reduces levels of material stress [77-79].

Auxetic materials are those that exhibit Negative Poisson Ratio (NPR) properties. Often in literature, researchers refer to these materials as either NPR [80] or auxetics [81, 82]. These properties enable for contraction (or expansion) in the transverse direction upon compression (or stretching) in an axial direction Dimple-and-void auxetic

structures can be customized and optimized depending on the application and the thermo-mechanical loading in a section.

Applications of these structures can include the turbine combustion wall and other sections of the turbine such as a vane of a blade. A cell composition can include square units, where every cell is composed of voids or dimples. Alternatively, other void shapes can be used such as elliptical or circular, I-, S-, or Z-shaped slots, barbell-shaped voids, hemispherical, semispherical shapes or a combination of these in order to maximize cooling and acoustic attenuation, coolant flow induced vibration as well as minimizing stresses [83-89]. Depending on the location of use, the structures can be optimized to match a minimum stress loading, compatibility of the geometry, and the temperature profile of a component.

Figure 13 shows an example of a hybrid dimple-and-void auxetic structure with an alternating pattern of symmetrical pimples and dimples. As a result of a stress optimization study, the current configuration of the pimple-dimple plate used in this work is introduced. Various parameters including the size and depth of both the pimples and dimples were adjusted topologically. The plate herein has symmetrical semi-circular pimple and dimple patterns with circular jet holes as explained in CHAPTER 4: of this work.
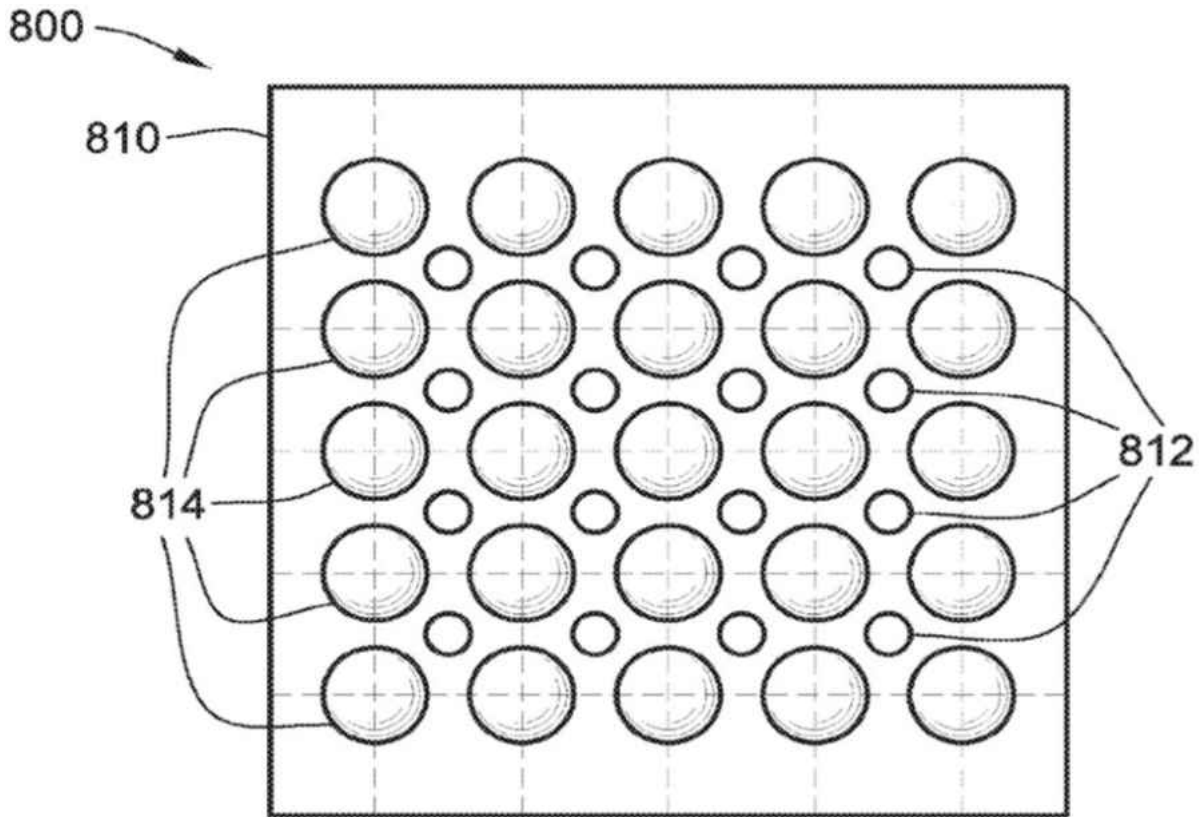
Figure 13: Example of a Hybrid Pimple-Dimple Auxetic Structures [83]

Objective of the Present Work

One of the main objectives of this study is to provide an understanding of the heat transfer in a multi-jet impingement configuration with pimples and dimples. The motivation of this study is to evaluate the combined effects of fluid flow and and heat transfer with the use of a plate with auxetic structures and the well-established heat transfer of multi-jet impingement on a flat wall in a crossflow configuration. The $Re_{av,j}$ is varied (5,000, 7,000 and 9,000) as well as (Z/D_j) between (2.4 - 6). The experimental set-up

and apparatus presented here are initially validated against the work done by Metzger et al. [28], and the span-averaged heat transfer on the surface is measured and validated with the correlations presented in [56, 90].

A numerical study is compared to the experimental work to help understand the physical phenomenon behind the heat transfer detriments and enhancements. Since the geometry is rather complex, various turbulence models need to be tested and compared against the experimental data. A further study of flow visualization has been carried out to complement the heat transfer work to obtain a better insight into the flow impingement characteristics. These details help to clarify some of the mechanisms related to the flow structures behind the heat transfer augmentation and detriments.

Novelty

The heat transfer study to examine an unusual method of vortex generation is proposed Equipping the jet plate with indentations and cavities have drag reduction features when compared to extruded or rough surfaces. While the heat transfer performance is an increase in some regions, it detriments in others. The detriment suggests that with the proper optimization of explanatory variables, the heat transfer coefficient can be maximized. Backed up by proper correlations for the validation and the novel impingement plates, this study is meant to set the first step into the exploration of

impingement cooling emanating from a plate with pimple and dimple geometries and

propose ideas to build upon.

CHAPTER 4:   EXPERIMENTAL PROCEDURE

In this chapter, an overview of the experimental setup is described. Examination of both flat and NPR plates are presented in the first section, showing geometric parameters of the jets, and the pimples and protrusions. The experimental apparatus used is discussed, followed by the details of the experimental setup. Methods on the data reduction and measurement techniques come last, followed by the heat transfer testing matrix used in this study.

Description of the Impingement Plates

Full CADs of the NPR orifice plates are shown in Figure 14, and that for the baseline plate in Figure 15. Due to the complexity of the geometry, the NPR plate was precisely machined at a machine shop. The baseline plate was manufactured using the in-house CNC machine. Starting from a flat sheet of Aluminum, this sheet was initially faced-off on both sides to ensure flatness, as any deviation in the plate thickness may result in an under or overestimation of the actual jet-to-plate distance. After that, in a two-step method, the orifices were drilled through, and then the orifice pockets were created.

Lastly, an all-around groove was machined on both plates, as can be seen in Figure 14 and Figure 15 as a housing for a rubber gasket. This ensures minimal-to-no leaking of the pressurized air between the plenum and the ambient, which forces the air into the

direction intended. To accurately obtain uniform jet diameters for both plates, the holes were initially pre-drilled to a size slightly smaller than the desired jet diameters. With rotary precision reamers, the jet holes were then enlarged and smoothened out completely. The precision of these reamers is in the order of 0.0002" (~ +/- 5 microns), and the exact value of 3.4875 mm was used in all calculations herein. However, the value of 3.49 mm is used throughout this text as a courtesy to the reader.

Each of the orifice plates consists of 26 jets in the x-direction (streamwise) and 20 jets in the y-direction (spanwise). Orifice holes used in both plates are arranged in a staggered configuration. The baseline plate has 520 jets with a diameter ($D_{j/f}$) of 3.49 mm and an orifice thickness-to-jet diameter ratio ($L/D_{j/f}$, $L/D_{j/p}$) of ~ 0.98 and ($L/D_{j/d}$) of 0.5. Maintaining the (L/D_j) value < 1 yields the highest heat transfer coefficient [91, 92]. The first row of jets are of 25 mm away from the closed wall. The NPR plate also has 520 jets with $D_{j/p}$ = 2.19 mm and $D_{j/d}$ = 4.63 mm for the protrusion and dimple, respectively. The ratio of protrusion overhang from the base of the plate-to-its jet diameter ($t_p/D_{j,p}$) is 2.78, while the dimple's inward depth-to-its jet diameter ratio ($t_d/D_{j,d}$) is 1.28. Nomenclature and geometric parameters of the NPR jet plate can be seen in Figure 16. The parameters used here are similar to those in Figure 12. The difference is in the jets emanating from the pimples and dimples for this study.

Figure 16 shows details of the geometrical parameters for the NPR plate. The sphere used to make the shapes are of ~ 34.13 mm and ~ 29.26 mm in diameter, for the dimple for the protrusion and dimple, respectively. In another form, ~ 35.7% of the protrusion is above the surface, and ~ 40.6% of the dimple is inside the surface. In both plate configurations, the streamwise jet-to-jet spacing (X_n) is equal to the axial jet-to-jet spacing (Y_n) of 25 mm. The height-to-target wall spacing (Z/D_j) was also varied in this study (2.4, 2.87, 3.25, 4, and 6). For the NPR plate, the actual (Z/D_j) varies because of the inward-outward spherical effects of the plate. To make a back-to-back comparison between the NPR plate and the baseline plate, the (Z/D_j) for the NPR plate was considered based on a ($D_{av,j}$) of 3.49 mm, as discussed earlier.
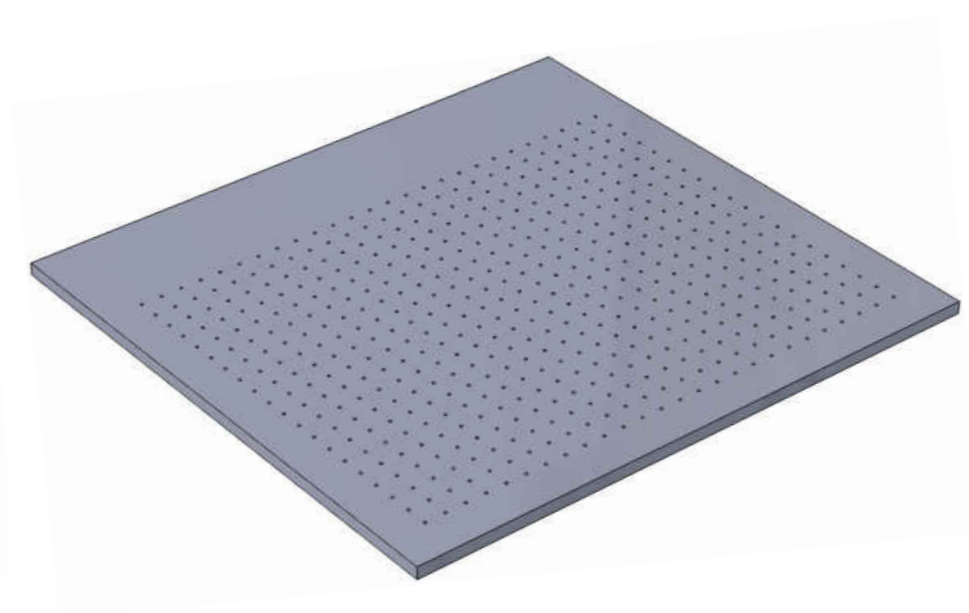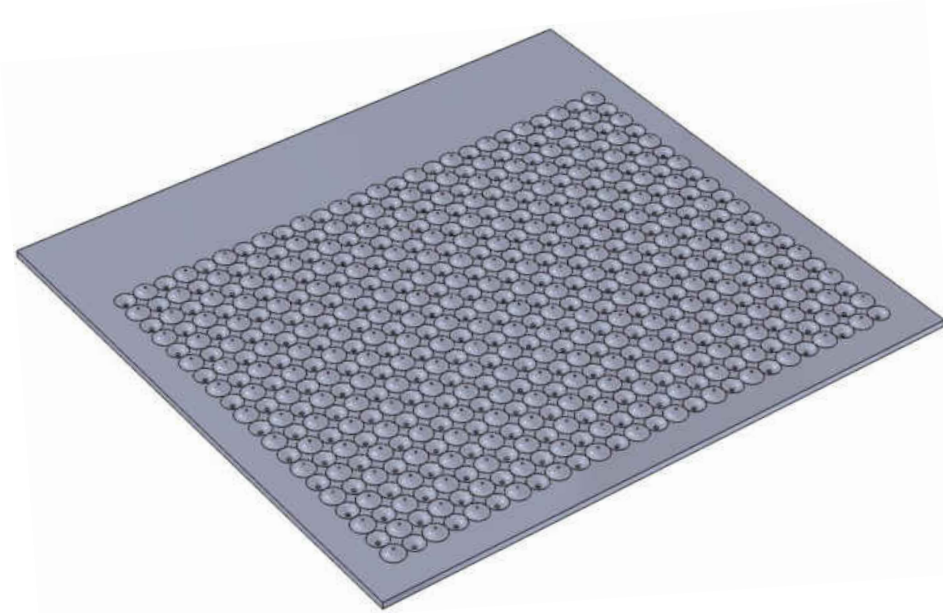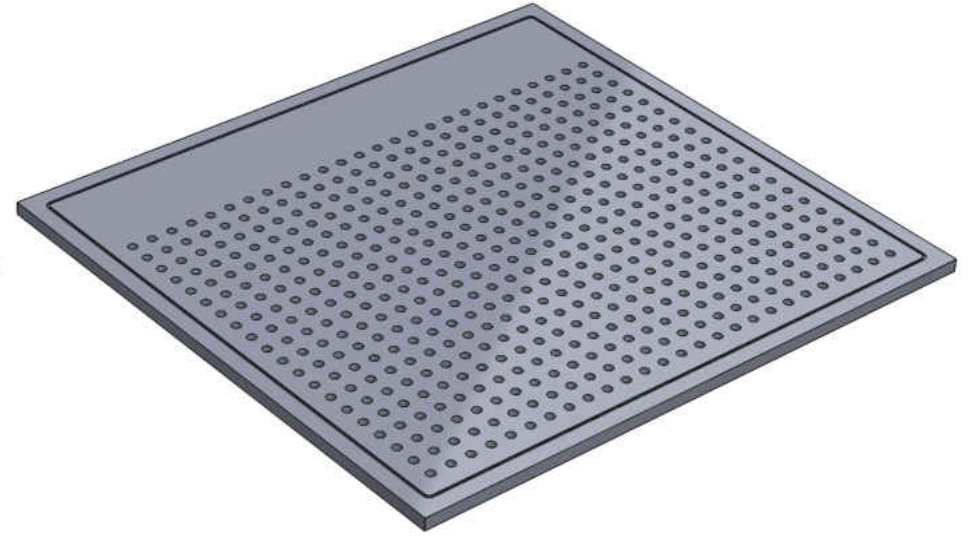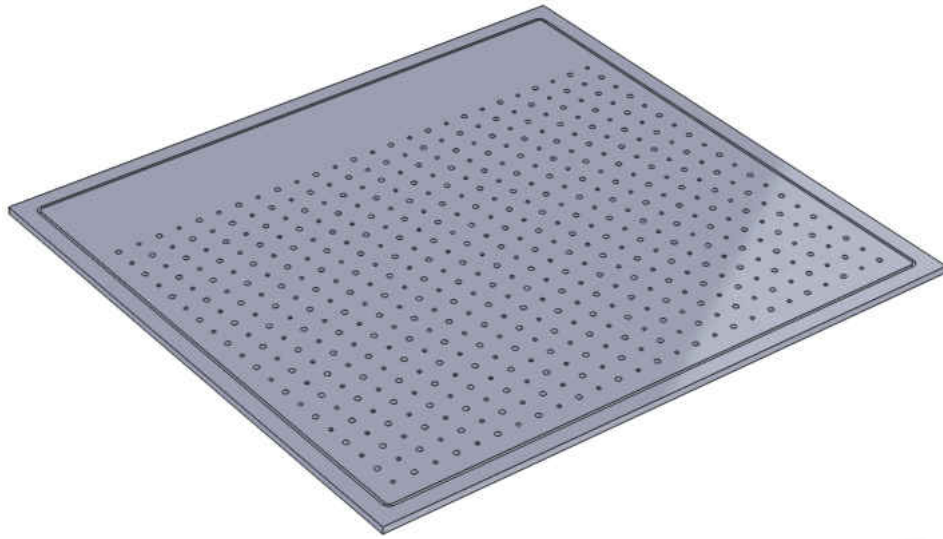
Figure 14: NPR Plate: Plenum Side (Top), Target Side (Bottom)   *Figure 15: Baseline Plate: Plenum Side (Top), Target Side (Bottom)*

Experimental Apparatus

A sketch of the experimental setup can be seen in Figure 17. Air is being discharged from one or two overhead blowers (Figure 17-A), providing a mass flow rate of up to 0.25 kg/s when operating in parallel, then the blown air is drawn through a 2" venturi flow meter (Figure 17-B). Downstream, the coolant air is directed into an elbow PVC pipe that feeds into a sheet metal plenum (Figure 17-C) with multiple stages of honeycomb flow straighteners (Figure 17-D).

Air is then discharged through one of two configurations of multi-hole orifice plates mounted on location seen in Figure 17-F and impinge on a target wall, segmented in 20 rows (Figure 17-G). From here on, we will call the plates with their designations; (baseline) plate with flat top and bottom, and NPR plate that has a flat top and a pimple-dimpled surface facing the target wall. The spent air is confined by three sidewalls positioned to induce a maximum crossflow configuration. In other words, a single preferential direction in the positive x-axis.

The test section is assembled from one of the two interchangeable orifice plates made of aluminum, mounted onto three interchangeable acrylic sidewalls of the same height. These three sidewalls serve as separators in the can vary in height, and to also constrain the flow to be spent in a single direction, maximum crossflow.

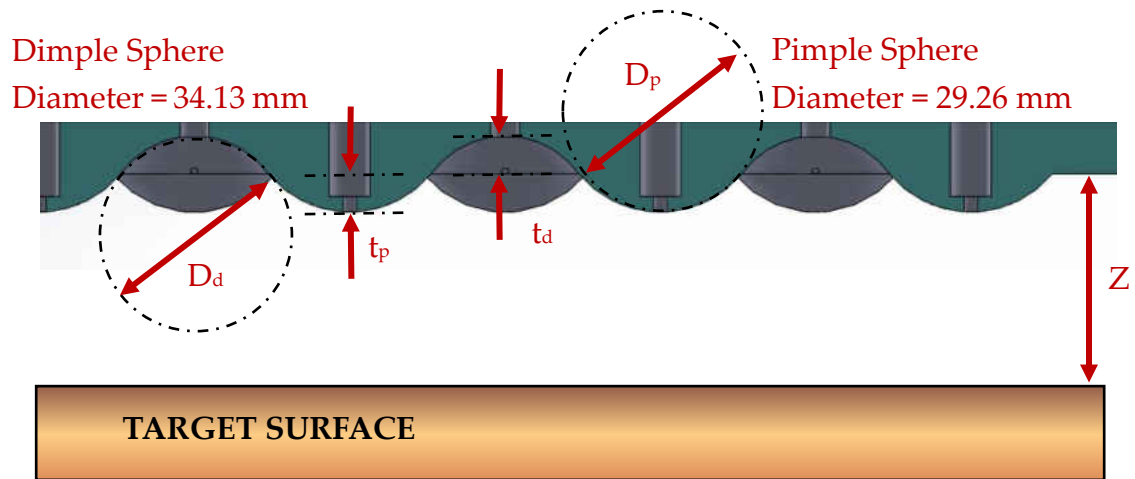Dimple Sphere Diameter = 34.13 mm

Pimple Sphere Diameter = 29.26 mm

D_p

D_d

t_p

t_d

Z

TARGET SURFACE

Figure 16: Dimensions and Nomenclature for NPR Jet Plate
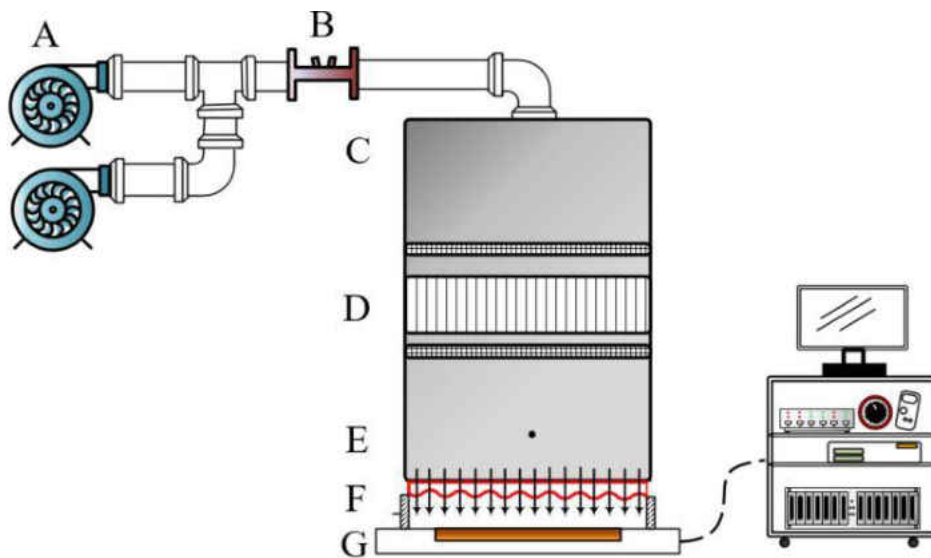

A

B

C

D

E

F

G

Figure 17: Schematic of Experimental Setup

Details of the Experimental Setup

The target surfaces are surrounded by Rohacell ® foam-based insulation ($k_{ins} < 0.03$ W/m.K) from all sides and bottom to ensure a maximum heat flux in a single (+ z) direction and minimal conduction losses from the target walls to the other directions. Moreover, extensive heat loss testing is quantified and applied in the calculation of the Nusselt number. Adjacent to each of the 20 target walls, a cork strip insulator of ~ 1.59 mm has been used along the length of each block to ensure minimal segment-to-segment heat conduction losses.

The target walls are made of smooth, machined copper. Each of those copper blocks is 320 mm long and ~ 23.41 mm wide, with a thickness of 10 mm. The bottom of those blocks each has a grove that runs in the middle, throughout the entire length, with three pre-drilled holes at a depth of 8 mm for thermocouples (TCs). Since the thermocouple junctions are 2 mm away from the surface, correction to the surface temperature may be considered Assuming a 1-D conduction model between the surface, and the thermocouple junction, a change in magnitude for the heat transfer coefficient is always < 1%. Details on this are described in the Surface Temperature section in Experimental Corrections of CHAPTER 4:.

Each TC is calibrated using the National Institute Standards and Technology (NIST) standards, and 3 TCs are instrumented into each block using Omega™ high

thermal conductivity epoxy (k = 12.5 W/m.K). Throughout this experiment, T-type

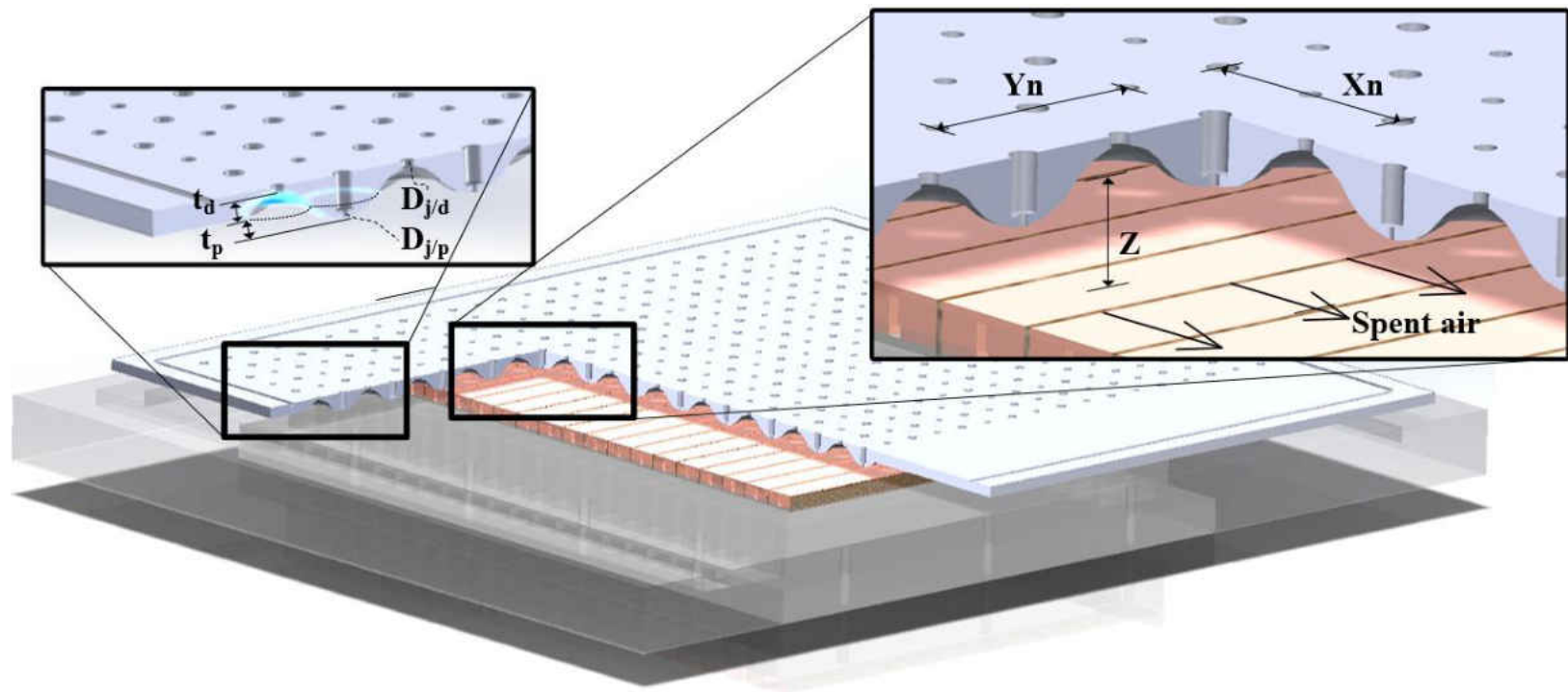Omega™ TCs are utilized for temperature measurement.

Figure 18: Detailed Schematic of the Testing Section

To obtain necessary flow boundary conditions that are used in this study, five TCs are installed in the plenum region, equally separated along the streamwise direction, and two TCs are instrumented downstream of the venturi flow meter. A rectangular covering sheet of Kapton ® tape (k_{kap} = 0.12 W/m.K, thickness = 7 x 10^{-5} m) is applied on top of the target walls to ensure surface smoothness and thus minimize flow tripping.

Figure 19 represents a schematic of the electrical circuit used for each heater. Each of the copper blocks sits on a custom-made silicone rubber heater (120 V, 114 Ω ± 2σ), supplying power up to 16,800 W/m². Four VariACs are utilized to supply a variable AC voltage to the heaters, with each supplying power to 5 heaters at a time. Since different copper block requires different power input, a set of 20 Rheostats (one for each heater) were connected to the heaters (50 Ω, 1.414 max amperage) to fine-tune the incoming current to each heater. These allow a robust control of heat input, and thus, the desired steady temperatures can be reached faster, and meet the required row-wise isothermal condition.

Pressure data was collected in order to compare that with the numerical study. A total number of 23 equally spaced static pressure taps were instrumented onto one of the sidewalls (inner diameter of 0.0575"), The streamwise location of each pressure tap is at each copper block centerline, except for block number 19 (due to a mounting bolt), and the four remaining taps are used downstream of the blocks. One additional pressure tap

is fixed to the testing plenum as is seen in Figure 17, 2.5″ above the jet impingement plate. Pressure taps are connected to a pressure scanner (Scanivalve SSS-48C MK4, range ± 20 inches of H_2O) by silicone tubing, which is connected to a 16-bit PCI migration board and a computer to record the data.
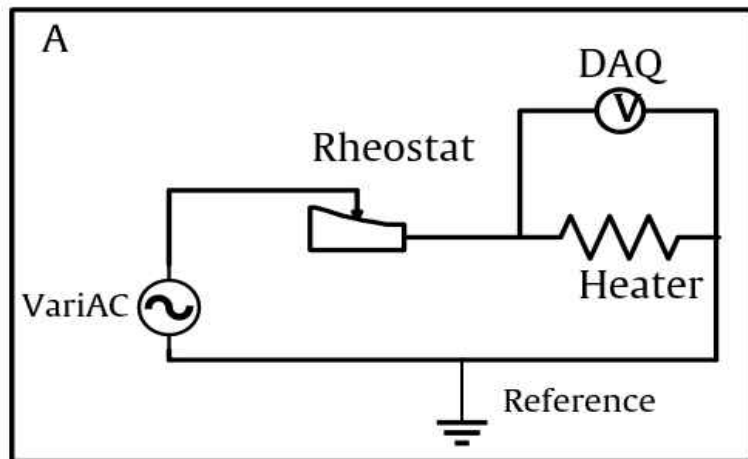

Figure 19: Electric Heater Circuit

Data Reduction and Measurement

Mass Flow Rate

Initially, a test is defined by setting the plate configuration and the jet-to-wall spacer for the correct (Z/D_j) value. One (or both) blower is turned on, and the flow is let cold in the system. The desired jet-average Reynolds number is achieved in the plenum and is determined by Equation (4-1).

$$Re_{av,j} = \frac{4\dot{m}_{tot}}{\pi D_{av,j} \mu} \frac{1}{n_{tot,j}} \qquad (4\text{-}1)$$

Where

$D_{av,j}$ Averaged jet diameter [mm]

$\dot{m}_{tot}$ is the total mass flow rate of air flowing in the plenum [kg/s]

μ Dynamic viscosity of air [N.s/m²]

$n_{tot,j}$ Total number of jets (520)

The mass flow rate is controlled by an adjustable flow regulator upstream of the venturi. Since the pimple-dimpled jet plate consists of two different jet diameters ($D_{av,j}$), the total effective open area of the jets is calculated based on the total open area multiplied by the experimentally found corresponding discharge coefficient of 0.665, 0.886 for the dimple and pimple, respectively. In a backward calculation of the total effective open area of the flat plate, it was determined that the average jet diameter is equal to ~ 3.49 mm for a discharge coefficient of 0.76, and this diameter was used to design the flat plate. This value is used in the calculations of ($Re_{av,j}$) for both jet plates. The number of jets, which is equal to 520 circular orifices is used to substitute ($n_{tot,j}$).

The differential pressure across the venturi throat, static pressure, atmospheric pressure, and temperature downstream of the venturi are measured and recorded. After that, the density of the air downstream can be calculated using Equation (4-2).

$$\rho_{air} = \frac{P_{amb} + P_{upstream}}{T_{vent} R_{air}} \qquad (4\text{-}2)$$

Where

ρ_{air} Air density [kg/m³]

P_{amb} Measured atmospheric pressure [Pa]

$P_{upstream}$ Pressure upstream of venturi throat [Pa]

T_{vent} The temperature of air at venturi [K]

R_{air} Gas constant

Then volumetric flow rate ($\dot{V}$) can be found using a pre-fitted third-order polynomial for a given pressure differential across the venturi throat. When these quantities are known, the total mass flow rate of air entering the system can be quantified in Equation (4-3).

$$\dot{m}_{tot} = \rho_{air} \dot{V} \qquad (4\text{-}3)$$

Where

$\dot{V}$ Air volumetric flow rate [m³/s]

Dynamic viscosity (μ) is assumed as a function of the temperature of the incoming air only and is found through a third-order polynomial curve fit given by Equation (4-4) at the temperature measured downstream of the venture. (T) here is the temperature

$$\mu = 5.42 \times 10^{-15} . T_{pl}^{3} - 2.53 \times 10^{-11} . T_{pl}^{2} + 5.87 \times 10^{-8} . T_{pl} + 2.8 \times 10^{-6} \qquad (4\text{-}4)$$

Experimental Corrections

Certain corrections within the data reduction are taken to provide for the most accurate results. These corrections include those related to the DAQ measurements, surface temperature readings, and heat leak-corrected heat input.

Heater Resistances

The DAQ, along with all other measurement devices, are calibrated against ASME standards. Detailed quantification of uncertainty in the measurements is described in detail in CHAPTER 5:. Examining the circuit diagram shown in Figure 19, the resistance associated with the DAQ is accounted for. In an independent test, the magnitude of the internal resistance for the DAQ is not associated with the temperature. This magnitude is found to be ~ 4.5 Ohms. The ohmage across the DAQ is subtracted from the calculation of power input into the system to provide for the most accurate results.

Surface Temperature

As described previously in the Details of the Experimental Setup of this chapter, the thermocouples are placed at 8 mm above the base of the copper blocks. However, the magnitude of temperature needed to calculate the Nusselt number should be that at the surface (10 mm) above the base. A 1-D conduction model over 2 mm of copper thickness

between the location of the thermocouple junction and the surface of the copper shows that the impact of the temperature difference on the heat transfer coefficient is always less than 0.1%. This is due to the relatively high thermal conductivity of copper

In a similar fashion, the 1-D conduction model over the thickness of the Kapton ® tape is carried to find the drop in temperature between the copper surface temperature and the temperature at the thin Kapton ® tape, where the jet impinges. Using the Kapton ®'s thickness, and thermal conductivity (th = 70 μm, k_{kap} = 0.12 W/m.K). Before data collection, validation tests are conducted with and without Kapton ®, to confirm the Kapton ® resistance characteristics. Figure 20 shows a side view of the testing section in Figure 18, with relative location of intrinsic thermocouples.

Figure 20: Relative Location of Thermocouple
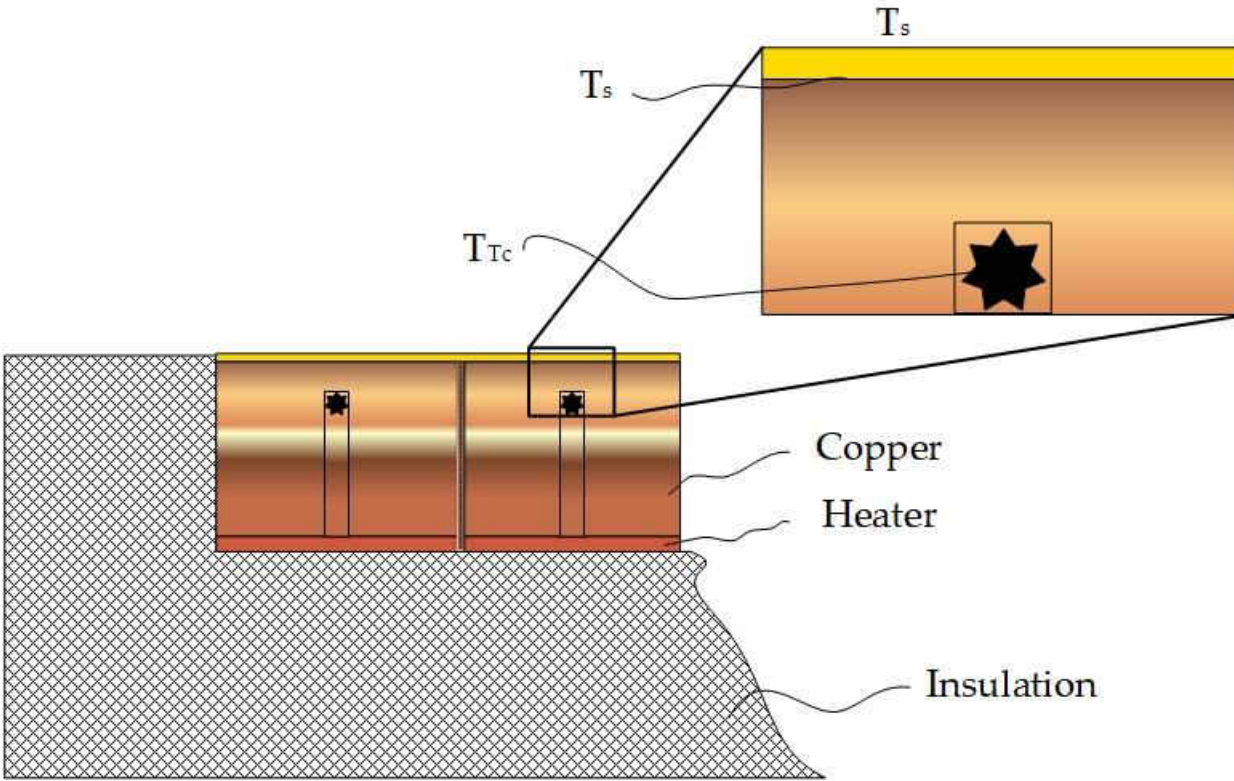
Heat Leakage

Heat leakage is quantified at a wide spread of temperatures for the experimental

setup without airflow. Since the experimental setup operates between the temperatures

of 60 °C and 90 °C, the power needed to reach these temperatures is deemed as power

lost (Q_{loss}). A curve fit of heat loss and surface temperature is created and utilized during

post-processing.

Conduction Losses

The following procedure for heat leakage applies to all twenty heaters. Here, a description of the process is outlined.

Initially, the power is turned on for all heaters, and the testing rig is let to steady-state at temperatures of 70, 80, 90, and 100 °C. At each of those temperatures, the voltage required to maintain the respective temperature, and the resistance of individual heaters are measured and recorded. At this stage, curve fitting of (1) resistance as a function of temperature, and (2) power lost due to conduction as a function of temperature are plotted and fitted against a 3rd order polynomial. This ensures the data is fitted with the highest coefficient of determination possible. In the temperature range described above, the coefficient of determination (r^2), which had a typical value of > 0.999. As expected, the fitting of the curves for resistance and power loss as a function of temperature could be fitted in linear regression. However, heaters 1 and 20 (first and last) experienced elevated levels of lateral conduction due to the unavailability of an adjacent heater from one side. A third-order polynomial was deemed best and was considered for all heaters to maintain consistency.

Losses Due to Radiation

Heat loss due to radiation can be given by Equation (4-5):

$$Q_{rad} = \varepsilon_{cop} \sigma A(T_s{}^4 - T_{amb}{}^4) \hspace{3cm} (4\text{-}5)$$

Where

Q_{rad} Heat lost due to radiation [W]

ε_{cop} the emissivity of the copper, polished down, w/out oxidation, 0.07 [93]. [-]

σ Stefan-Boltzmann Constant, 5.67 x 10⁻⁸ [W/m².K⁴]

A Surface area of the copper bock [m²]

T_s Temperature at the surface [K]

T_{amb} Temperature at ambient conditions [K]

Losses due to radiation are found to be multiple orders of magnitude lower than the losses due to conduction. Since heat loss due to radiation is minimal, the above procedure discussed herein does not account for these losses.

During the quantification of the overall heat losses, the jet holes were entirely blocked-off with sealing tape, and the outlet channel of the testing section is also blocked to limit the natural (free) convection.

Thermal Conductivity of the Air

The quantity (k_{film}) used in the calculation of Nusselt number varies with the measured relative humidity and the film temperature. The humidity is measured at the time of the test and recorded. In the air-condition controlled zone of the testing setup, the recorder relative humidity varied between 45 – 55%. An Omega™ RH-85 hygrometer is

used as a reference for the measurement. As for the temperature, an arithmetic mean of four temperatures is used: 2 from the plenum readings, and 2 temperatures of the isothermal surfaces of the copper. In the subsequent section, further explanation of the two-test method is described in detail. The final value for the thermal conductivity is found using the correlations developed by Tsilingiris for a given temperature and relative humidity [94] .

Heat Transfer

In the calculation of Nusselt number, two separate tests for each Reynolds number are conducted. That is, for each test, the power input for each block is individually tuned through a rheostat, to achieve an isothermal condition among the blocks. The definition of isothermal is that all 20 block segments are to be within 0.4 K from each other. The first test (low-temperature test) is 18 °C above the jet inlet temperature, while the second is 36 °C (high temperature) above the jet inlet temperature. At temperature ramp-up, TCs are closely monitored until the desired isothermal surface temperature is reached. Individual tuning of power input is necessary at this point since blocks lose heat to the spent air at different rates. When at a steady temperature, data is collected for 5 minutes at a sampling rate of 1 Hz for voltage and temperature. This sampling time length was set to achieve statistically stationary properties for the data sample.

Heat transfer due to convection is given by Equation (4-6)(5-7)

$$Q_{in} - Q_{loss} = h_{av,i}A(T_{s,i} - T_{ref,row})$$

(4-6)

Where

Q_{in} Heat input [W]

Q_{loss} Heat lost due to conduction [W]

$h_{av,i}$ local span-averaged row convective heat transfer coefficient [W/m².K]

$T_{s,i}$ average temperature of the surface wall, averaged using three equally

spaced TCs at 2 mm below the surface of the block [K]

$T_{ref,row}$ the reference temperature [K]

The difference between the two tests at the specified Reynolds number is the

power input, heat loss due to conduction and wall temperature. Using this method, and

combining two datasets, yields two heat transfer equations with two unknowns, being

the heat transfer coefficient ($h_{av,row}$) and ($T_{ref,row}$).

To find $T_{ref,row}$, the 2-test method is used to yield:

$$Q''_{in,1} - Q''_{loss,1} = h_{av,1}(T_{s,1} - T_{ref,row})$$

(4-7)

And,

$$Q''_{in,\,2} - Q''_{loss,2} = h_{av,2}(T_{s,2} - T_{ref,row})$$

(4-8)

Where

$Q''_{in,i}$ Heat flux into the system input [W/m²]

$Q''_{loss,i}$ Heat flux lost from the system [W/m^2]

$T_{s,i}$ Averaged segment surface temperature [K]

Solving for $T_{ref,row}$ yields

$$T_{ref,row}= \frac{(Q''_{in,1}- Q''_{loss,1})T_{s2}-(Q''_{in,2}- Q''_{loss,2})T_{s1}}{(Q''_{in,1}-Q''_{loss,1})-Q''_2-Q''_{loss,2}} \qquad (4\text{-}9)$$

Plugging the above Equation (4-9) into either Equation (4-7) or Equation (4-8) yields $h_{av,row}$, the local heat transfer coefficient on a given strip.

Heat input into the system can be given using the formula for electric power in Equation (4-10). The voltage and resistance are acquired during the steady-state of both tests.

$$Pwr = V^2 / Res \qquad (4\text{-}10)$$

Where

Pwr   Power supplied by the heater to each block [W]

V   Voltage input [V]

Res   Electric resistance at a specified temperature [Ω]

At the film, even though the TC average temperature makes for an excellent approximation of the temperature of the target surface, the thin layer of Kapton ® tape is considered as thermal resistance. From the above analysis and data reduction techniques, the heat transfer coefficient can be calculated at each copper segment.

Finally, the localized span-averaged row Nusselt number for a row of impinging jets is given by Equation (4-11)

$$Nu_{av,row} = \frac{h_{av,row} \cdot D_{av,j}}{k_{film}}$$ (4-11)

Where

$Nu_{av,row}$ is the span-averaged Nusselt number

$h_{av,row}$ local span-averaged row convective heat transfer coefficient [W/m².K]

$D_{av,j}$ Averaged jet diameter [mm]

k_{film} Thermal conductivity at the film

Since two tests are utilized in the calculation of Nusselt number, the best film temperature approximated value is in a range somewhere between the plenum and the surface temperature. However, because two tests are involved, the arithmetic means of 4 temperatures obtained from the surface temperature at high power test, the surface temperature at low power test, and both plenum temperatures were used along with the hygrometer-recorded relative humidity to find the final value of thermal conductivity at the film using the correlations mentioned in the previous section.

Heat Transfer Matrix

A range of Z/D_j values and Reynolds numbers were selected for both the baseline plate and the NPR plate. The details for these tests is found inTable 3. Initially, three Z/D_j

were selected to conduct this study. However, gaps in the data encouraged the addition

of two additional cases per jet-averaged Reynolds number per impingement plate.

Table 3: Heat Transfer Testing Matrix

Plate Configuration	Reynolds number	$Z/D_{av,j}$
Flat	5,000	2.4
		2.87
		3.25
		4
		6
	7,000	2.4
		2.87
		3.25
		4
		6
	9,000	2.4
		2.87
		3.25
		4
		6
NPR	5,000	2.4
		2.87
		3.25
		4
		6
	7,000	2.4
		2.87
		3.25
		4
		6
	9,000	2.4
		2.87
		3.25
		4
		6

CHAPTER 5:   EXPERIMENTAL UNCERTAINTY

The uncertainty analysis associated with the experimental data is inclusive of both systematic and random errors, with a 95 % confidence interval. Methodologies adopted in this chapter follow the guidelines of:

- ANSI/ASME PTC 19.1-2005 [95],

- The approach outlined in Figliola and Beasley [96] based on the partial differentiation method proposed by Moffat [97].

The systematic error, also known as bias, is an uncertainty due to an instrumentation error. These values are obtained from the manufacturer's datasheet for each equipment used. The random error, also known as the precision error, is based on the standard deviation of the data sets obtained from repeatability tests.

Error Propagation

If **R** is considered a result, determined through a functional relationship between independent variables x_1, x_2, x_3, …, x_n as defined in by relation (5-1).

$$\mathbf{R} = f_1 \{x_1, x_2, x_3, ..., x_n\} \tag{5-1}$$

Where

R   Result function

n   The number of independent variables

The uncertainty in **R** with respect to x_n can be denoted as

$$uR_{x_n} = \frac{\partial \mathbf{R}}{\partial x_n} \cdot u_{x_n} \tag{5-2}$$

for n = 1, 2 …, N

Where

uR_{x_n} Uncertainty in **R,** the result function

$\frac{\partial \mathbf{R}}{\partial x_n}$ Sensitivity index, the partial derivative of **R** with respect to x_n

u_{x_n} Uncertainty in x_n

Each variable will have some uncertainty associated with it that impacts the result.

To estimate the true mean value, **R** can be written as

$$\acute{R} = \overline{R} \pm u_R \tag{5-3}$$

Where,

$\acute{R}$ True mean value in result function **R**

$\overline{R}$ Sample mean;

u_R Uncertainty in $\overline{R}$

$$\overline{R} = f_1 \{\overline{x}_1, \overline{x}_2, \overline{x}_3, …, \overline{x}_n\} \tag{5-4}$$

$$u_R = f_1 \{u_{\overline{x_1}}, u_{\overline{x_2}}, u_{\overline{x_3}}, ..., u_{\overline{x_n}}\} \tag{5-5}$$

Where

u_R The individual uncertainty contribution propagating through **R**,

$u_{\overline{x_1}}$ The uncertainty of $\overline{x_1}$

The uncertainty in **R** with respect to x_i can finally be combined into Equation (5-7)

$$u\mathbf{R} = \sqrt[2]{\left(\frac{\partial R}{\partial x_1}u_{x_1}\right)^2 + \left(\frac{\partial R}{\partial x_2}u_{x_2}\right)^2 + \left(\frac{\partial R}{\partial x_3}u_{x_3}\right)^2 + \cdots + \left(\frac{\partial R}{\partial x_N}u_{x_N}\right)^2} \tag{5-6}$$

Where

u**R**   The total uncertainty that includes both errors due to bias and precision.

However, the following conditions must be satisfied when using Equation (5-6) [98]:

1. Measurements were each independent

2. Gaussian distribution is observed when repeated measurements are taken

3. The same confidence interval is used to quantify for each uncertainty.

<center>### Uncertainty Trees</center>

Uncertainty trees are one powerful tool that contributes to the understanding of error for various measurands. They are useful in tracking various parameters that contribute to the overall (total) uncertainty.

<center>**Reynolds number**</center>

The Equation for Reynolds number is given by Equation (4-1)

$$Re_{av,j} = \frac{4 \cdot \dot{m}_{tot}}{\pi D_{av,j} \mu} \frac{1}{n_{tot,j}}$$

(4-1)

Equation (4-1)**Error! Reference source not found.** can also be written as a function of the measurands as explained in CHAPTER 4:. I.e., in Equation (5-7):

$$Re_{av,j} = f\left(P_{amb}, P_{upstream}, T_{vent}, \Delta P_{vent}, D_{av,j}\right)$$

(5-7)

Where the measurand

ΔP_{vent} The pressure differential across the venture throat [Pa]

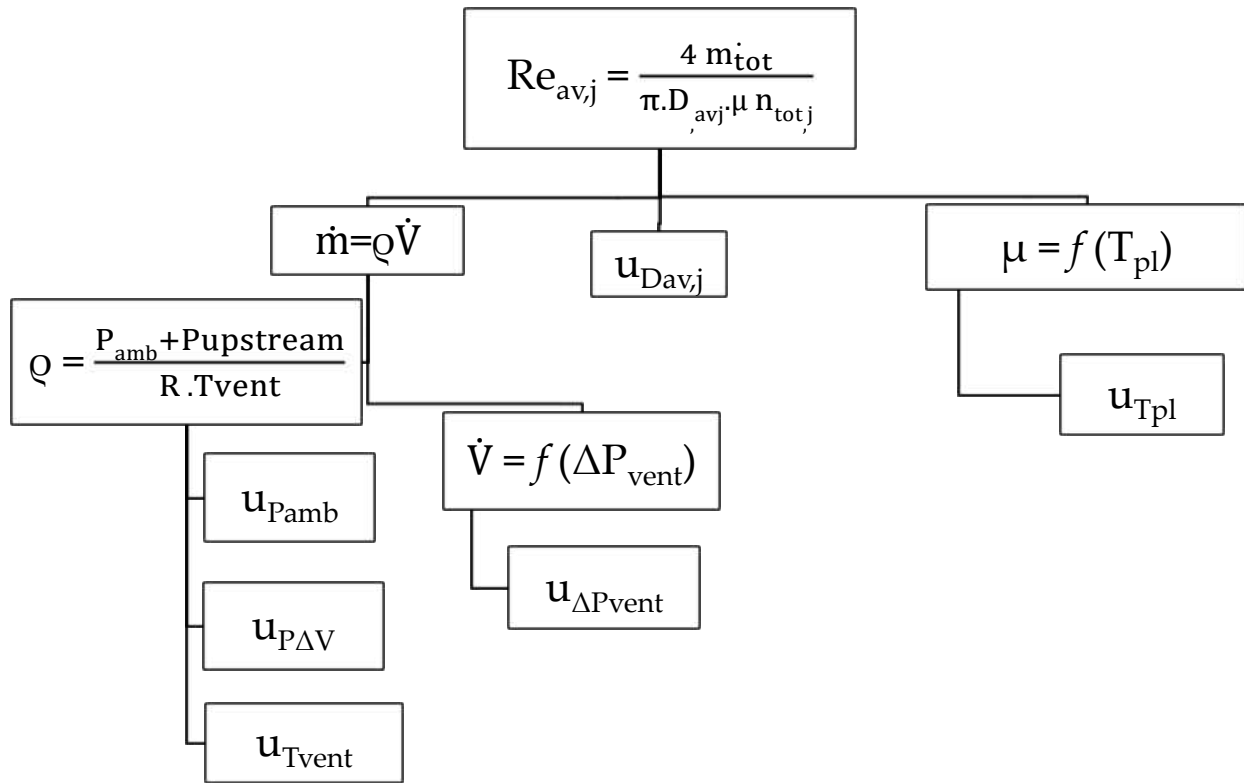The uncertainty tree associated with the Reynolds number is shown in Figure 21.

<center>69</center>

$$Re_{av,j} = \frac{4\ \dot{m}_{tot}}{\pi . D_{avj} . \mu\ n_{tot\,j}}$$

$$\dot{m} = \varrho \dot{V}$$

$$u_{Dav,j}$$

$$\mu = f(T_{pl})$$

$$\varrho = \frac{P_{amb} + P_{upstream}}{R . T_{vent}}$$

$$u_{Tpl}$$

$$u_{Pamb}$$

$$\dot{V} = f(\Delta P_{vent})$$

$$u_{P\Delta V}$$

$$u_{\Delta Pvent}$$

$$u_{Tvent}$$

Figure 21: Uncertainty Tree for Reynolds Number

Nusselt number

The Equation for Nusselt number is given by Equation (4-11).

$$Nu_{av,row} = \frac{h_{av,row} \cdot D_{av,j}}{k_{film}} \tag{4-11}$$

Equation (4-11) can also be written as a function of the measurands, explained in the Heat Transfer section on page 61:

$$Nu_{av,row} = f(T_{s1}, T_{s2}, T_{pl}\ V_1, V_2, D_{av,j}, D_{av,j}, W, L, RH) \qquad (5\text{-}8)$$

The uncertainty tree associated with the Nusselt number is shown Figure 22[1].
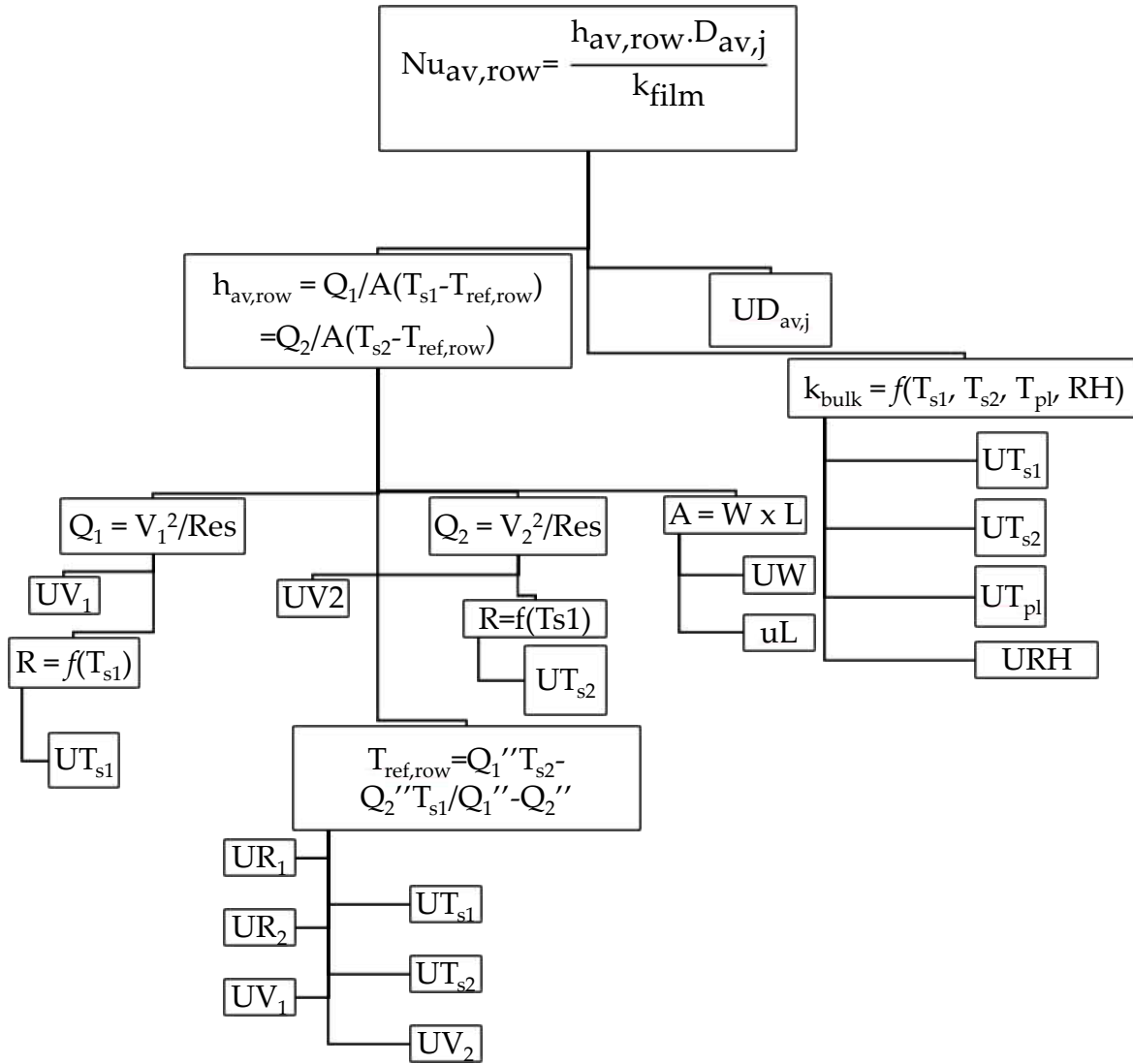

Figure 22: Uncertainty Tree for Nusselt Number

---

[1] Heat losses in the uncertainty calculation is accounted for and are a function of T_s and power input.

Summary of Uncertainty

The uncertainty associated with the temperature reading using thermocouples and DAQ equipment is ± 0.6 K. The uncertainty related to the power supplied to the heaters is approximately ± 5.7 %. The measured mass flow rate has an uncertainty of approximately ± 2.6 %. Pressure measurement readings have an uncertainty of 4%. According to the methodology outlined above, the maximum uncertainty in the calculation of the Nusselt number is ± 8.7%. For the flow rate measurement, the uncertainty associated with the calculation yields a ± 5.8% maximum error in Reynolds number. Error percentages due to uncertainty in the measurements are presented in Table 4.

Table 4: Summary of the Uncertainty in Experimental Results

Non-Dimensional Quantity.	± (%)
Nusselt number	8.7
Reynolds number	5.8
Mass flow rate	2.6
Heat flux	5.7

To obtain a better perspective on the uncertainty in Nusselt number, an individual study of the effects of each measurand is shown in Figure 23. The summation of all the contributors in the uncertainty is equal to 100 %. It can be seen that the highest

contributors to the total uncertainty come from the measurements of the surface temperature for both the high and the low tests, T_{s1} and T_{s2}. These combined contribute towards about ~ 81%. Next highest is the thickness of the Kapton ® tape used to calculate the actual surface temperature as explained in the Experimental Corrections section of CHAPTER 4:. Thermal conductivity of the film comes right after at ~ 12% and the rest of the measurands such as voltage readings, thermal conductivity of the Kapton ® tape, heater resistance, heat leakage, jet diameter, area of the copper blocks and plenum temperatures are counted towards < 5% each.
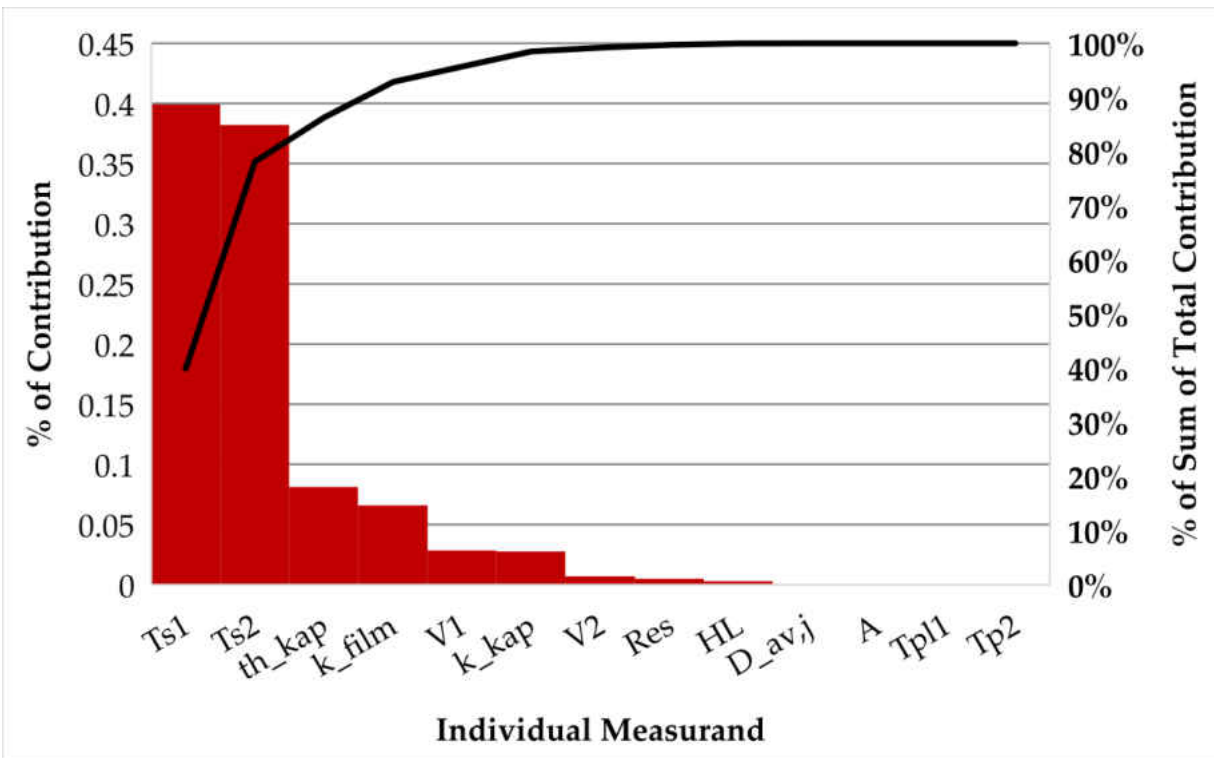

Figure 23: Pareto Chart of Uncertainty in Nusselt Number

CHAPTER 6:   NUMERICAL MODELING

Computational Fluid Dynamics (CFD) is becoming a more popular tool to solve various fluid-related problems. The availability of powerful computers has enabled more access to the tool. In this chapter, brief descriptions of the workflow of numerically approximating the solution for a problem is presented. Followed by the workflow followed for the problem presented herein. This includes a representation of the domain used, the process and refinements of meshing, the boundary conditions, and solvers, and lastly, a description of the various turbulence models used that got compared to the experimental results.

Introduction

With the increase in computational abilities, a new mode of utilizing CFD commercial solvers is by using them for optimization. Here, a feedback loop that involves the model, initial conditions, objective function(s) is considered. The geometry changes, re-meshed, and governing equations are solved again to reach to a closer target. The CFD problem is numerically solved (approximately) in a multi-step process that starts with the accurate modeling of the geometry in question. The importance of the CFD is to help understand complex physical phenomena happening with the flow, to help produce a better product. To avoid experimental building time and space for equipment associated

with experimental work, the solution to the numerical simulations can be validated against open literature when it exists.

A model is initially prepared in a Computer-Aided Design (CAD) software package, whether within the CFD software package or external CAD package. The created model represents the "as perceived" in real life. Since the CFD package solved for the fluid domain, a "negative" of the solid geometry is produced. The newly generated geometry is called "air-solid" or "fluid domain/volume". Some fluid domains may require modifications without much additional computational cost. An example of this would be to add an extension to an inlet or outlet to reduce solution instabilities. An example where the fluid and a solid is modeled would be in a conjugate heat transfer problem. Where both the solid and the fluid are modeled to solve a set of equations that conform with both the solid and the fluid, i.e. conduction and convection problem. In a non-conjugate heat transfer problem, the fluid domain is imported into the CFD package and is prepared for the next step, meshing or discretizing.

In order to solve the set of governing equations such as the conservation of energy, mass, and momentum, the fluid volume is then discretized in smaller cells that make up the mesh. The abovementioned equations are solved in each of those cells to produce a solution to the problem. The accuracy and stability of the solution highly depend on many aspects; the quality of the mesh is one of them. There exist many techniques, tips

and ideas on how to produce a high-quality mesh, and that depends on the method used

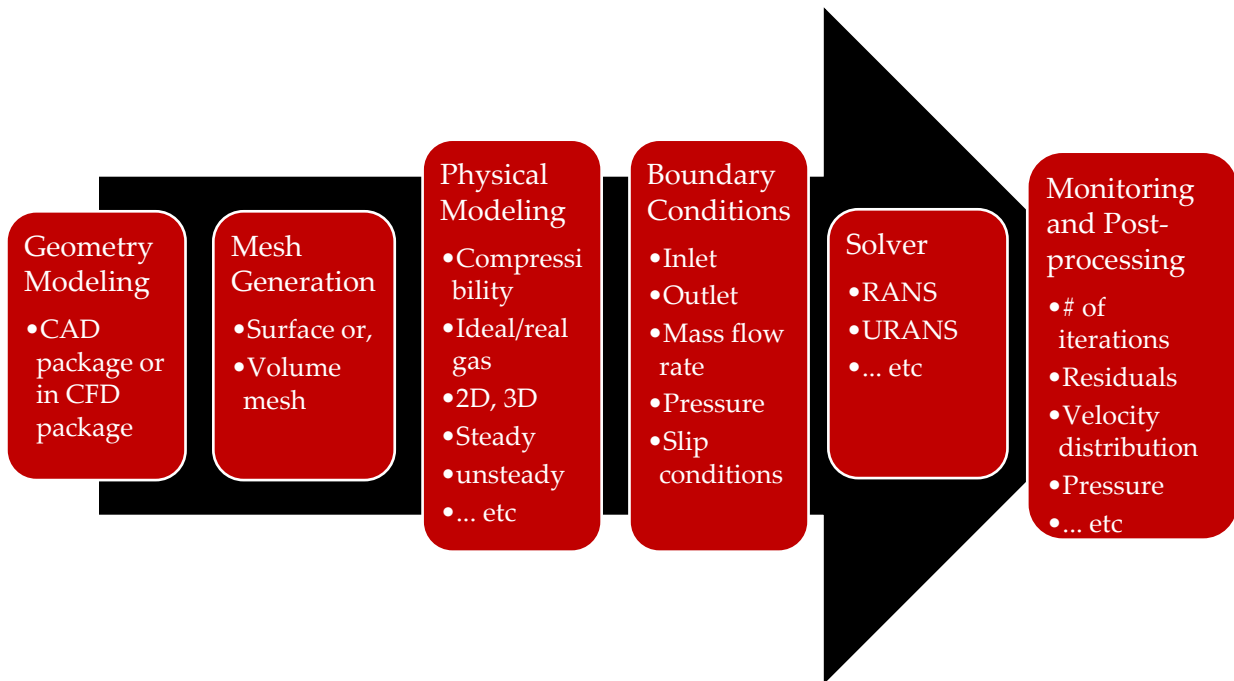to mesh and the complexity of the geometry as an example

Figure 24: CFD Simulation Workflow

All faces of the fluid domain must be represented by a boundary condition. These

conditions set at the boundaries specify the physics at that face. They generally include

the inputs required to solve the problem, such as pressure, the velocity of mass flow rate

conditions. Once the governing equations are solved iteratively in each cell within the

mesh domain, the different residuals are calculated, and if below a certain pre-specified

threshold, then the solution is considered converged and ready for post-processing,

where useful information about the flow or the solid can be extracted. The overall workflow for a typical CFD problem is illustrated in Figure 24.

A numerical study is compared to mimic the experimental setup and the flow conditions, as previously discussed in CHAPTER 4:, to be able to physically understand the flow emanating from the NPR plate. In this chapter, discussions on the model used for the numerical study, details on the mesh used, and refinements around critical regions are presented along with mesh sensitivity effects. The boundary conditions, solvers, planes of symmetry, and comparison of turbulence models are presented herein.

The Physical Model

The computational domain for the numerical model of this study is shown in Figure 25. A full-length section of the rig is modeled in the streamwise direction, with a sufficient extension outward in the far-right region. This domain extension would help minimize any flow disturbances towards the exit of the domain and to define the outlet boundary conditions. This domain features 2-half jets in the spanwise direction, in a way that a symmetry of a periodic condition can be applied. The inclusion of these two halves ensures the staggered configuration of pimples and dimples, and the flow behavior due to this configuration is adequately captured. This reduction in the boundary conditions in the spanwise direction is meant to make the numerical problem less computationally

expensive while maintaining the proper boundary conditions. Since different jet-to-target wall spacings are simulated, five models were created, one for each spacing ratio. The distance between the NPR features and the target wall is the only thing that changes.
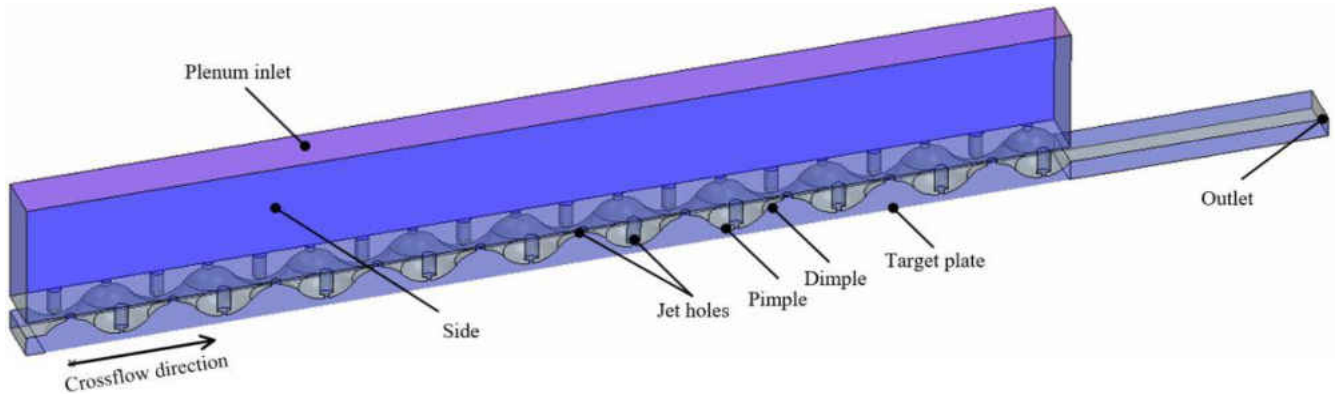

Figure 25: NPR Computational Model for Numerical Study

The Mesh

The computational domain is initially built in a commercially available CAD software based on the exact dimensions of the experimental setup. The model is then imported into the commercially available software *Simcenter Star-CCM+®* 11.06.011-R8 by *Siemens PLM®*. Pre-meshing, the physical model is trimmed on two planes at the center of the jets to be able to mimic two half rows of jets. The plenum on top of the jet holes is added as a solid rectangular box, and an outlet is included as briefly discussed earlier.

Figure 26 shows an overview of the meshed domain, using the custom controls and refinements near-critical regions. Using the advanced layer meshing, the model is discretized into fine elements. In the entire domain, polyhedral meshing cells are used except for the boundary layer region near all the walls, where advanced prism layers are used. On the target surface and pimple-dimpled surfaces, 20 layers of prism are used with a growth ratio of 120% for each layer past the first. The walls by the jet entrance have 15 prims layers with an expansion ratio of 120% as well. The first prism cell is set to have an initial cell thickness of 4 microns (0.004 mm). More refinements and volumetric controls are included in the model near the target wall region, and in the region close to the jet holes from the plenum side.
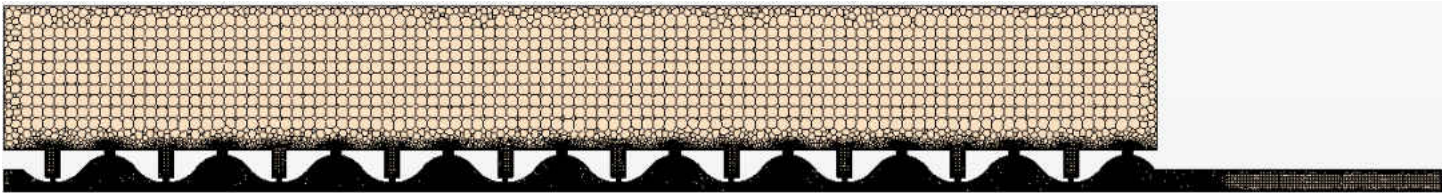

Figure 26: Overview of the Domain Mesh

One of the criteria to show the proper capturing of the physics at the wall is the non-dimensional wall thickness of y+. This value is detrimental based on the first wall's thickness. To be able to achieve a y+ value of < 1 in all locations, the 4 microns cell thickness is decided. Distribution of the final local y+ value is shown in Figure 27 for the target wall and Figure 28 for the NPR pimple-dimpled surfaces at the utmost critical case.
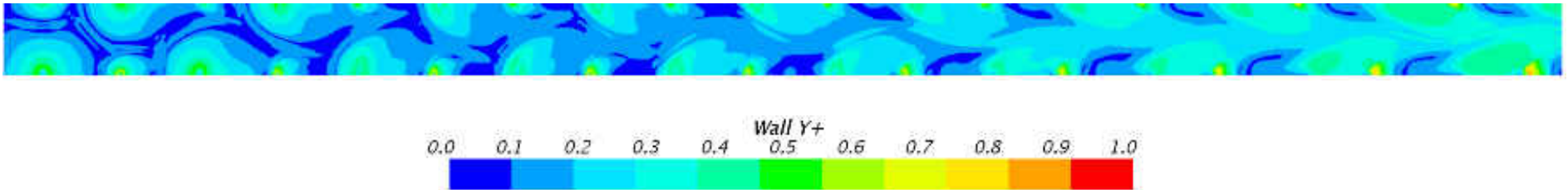
Re$_{av,j}$ = 9,000 Z/D$_j$ = 2.87
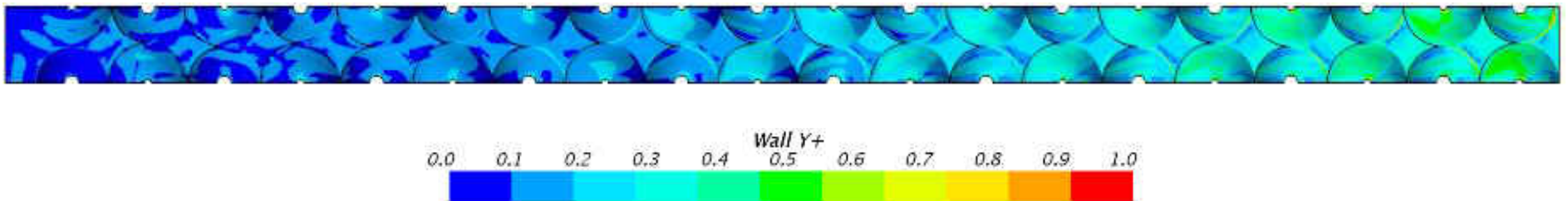

Figure 27: Target Wall Y+ Contour Plot

Figure 28: NPR Surfaces Wall Y+ Contour Plot

On the jet regions, two local refinement zones are dedicated to each of the jets, making the number of jet refinements equal to four. Figure 29 shows the region where the refinements are added with respect to the domain. The first refinement is at the nozzles, and the second is in the region of the jet core. This step ensures adequate capturing of the jet flow within the nozzle and associated velocity gradients. The final result of the mesh at the jet region is shown in Figure 29.

In total, the number of meshed elements in this domain is near 12.5 million cells. All the parameters related to the mesh quality are maintained within *Siemens PLM®* *Simcenter Star-CCM+®* recommended values and meshing best practices.
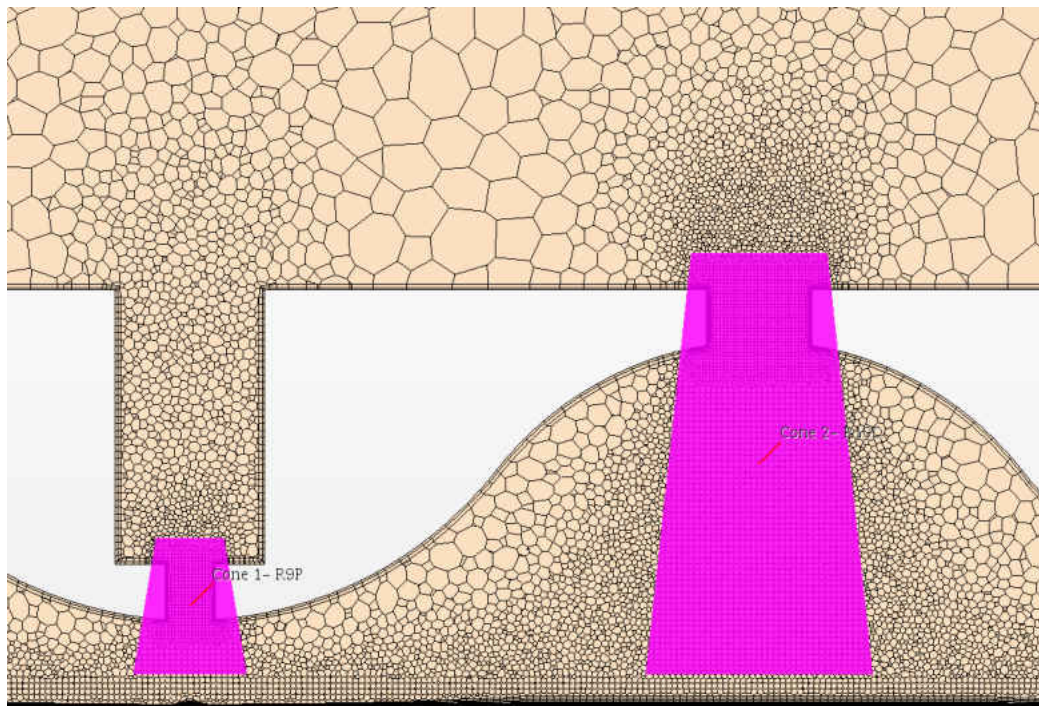

Figure 29: Depiction of the Control Volumes for Mesh Refinement at Jet Region
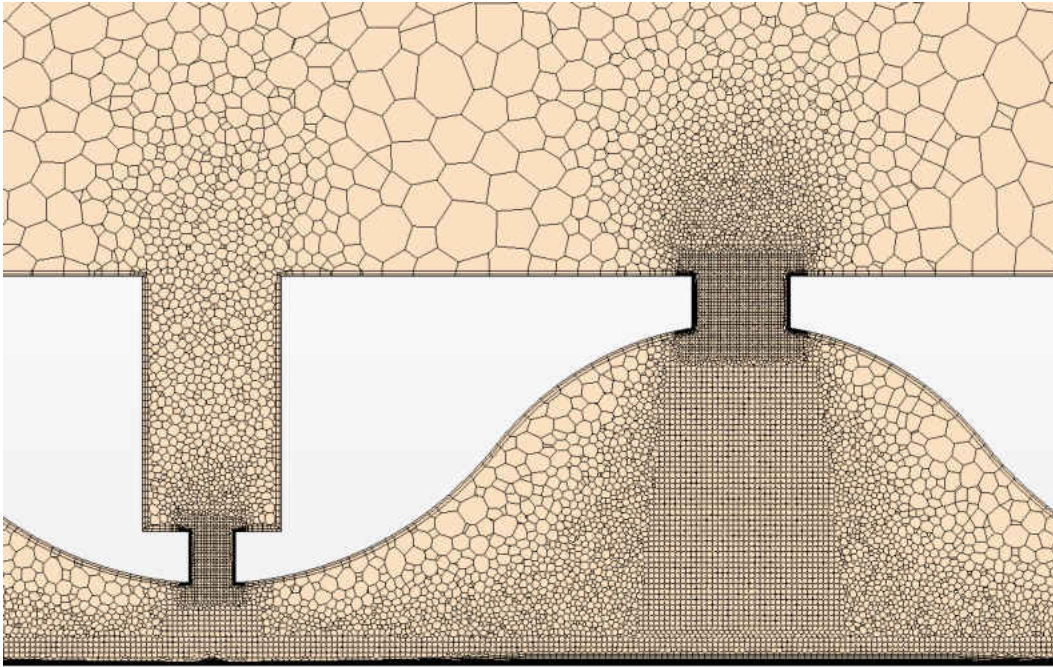
Figure 30: Locally Refined Mesh around the Jets

The effects of mesh refinement (mesh sensitivity) has been studied. Figure 31 shows the predicted effect on the surface heat flux for $Re_{av,j}$ = 9,000 case with spacing ratio $Z/D_{av,j}$ = 2.87. A maximum of ~ 1.5% change is observed when the mesh size is doubled to 25 million cells. This suggests that no additional refinement is needed, and additional refinement would deem insignificant. The heat transfer and fluid flow of the current configuration compares well with the heat flux results obtained from the experimental data for the majority of the areas. These areas showed enhancement in the results with increase in number of iterations.
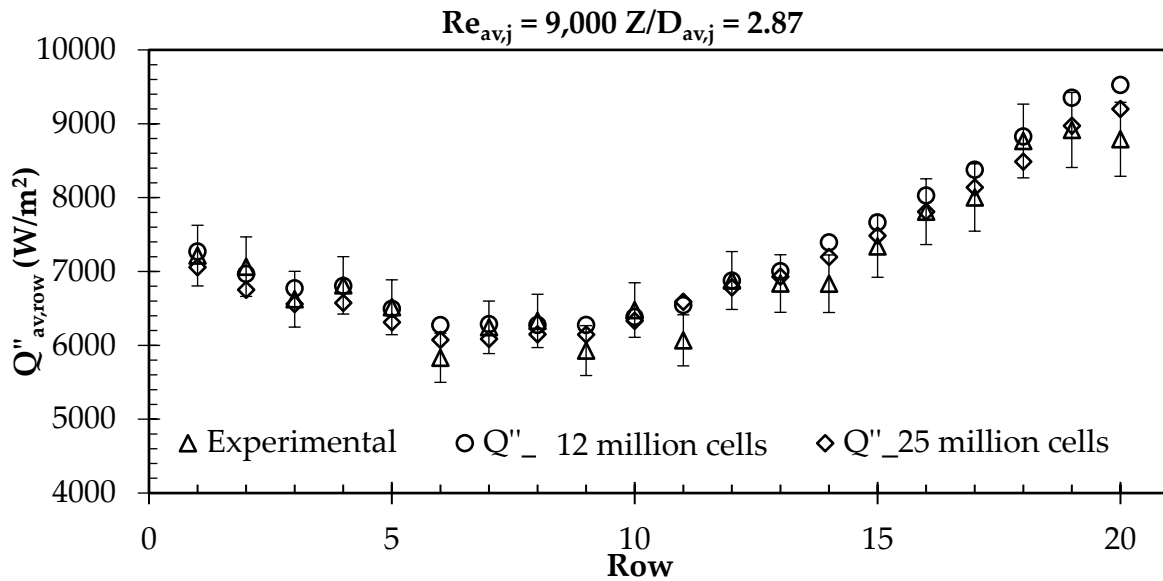
Figure 31: Effect of Mesh Refinement on Surface Heat Flux

Boundary Conditions, Solvers, Residuals and Convergence Criteria

The boundary conditions used for the numerical simulation are shown in Table 5. The stagnation pressure and temperature used for the inlet boundary condition are obtained from the plenum pressure and the thermocouple junction readings, at location E in Figure 17. The target mass flow rate is obtained from the method outlined in the Mass Flow Rate section of CHAPTER 4:.

Simulations for this model are performed using the *Siemens PLM® Simcenter Star-CCM+®* commercial computational fluid dynamics (CFD) solves using built-in segregated flow and energy. Properties of the fluid are temperature-dependent for higher accuracy, and the laws of an ideal gas are used.

83

Table 5: Boundary Conditions for Numerical Model

Surface Name	Boundary Condition
Inlet	Stagnation Pressure Temperature
Outlet	Target mass flow rate
Sides	Symmetry wall
Target surface	No-slip condition Iso-thermal (low and high-temperature tests)

Monitors for various parameters have been observed during the numerical simulation to determine the convergence criteria. Figure 32 shows locations of various point probes in the fluid domain and on the surfaces. Fifteen point-probes in the fluid region are used to monitor temperature, velocity, and pressure of the fluid. These are seen in rows 4, 12, and 18. Eleven point-probes on the surface in rows 3, 11, and 17 are used for heat flux monitoring. Heat transfer on the surface is monitored using 33 various locations, covering a large part of the target wall.
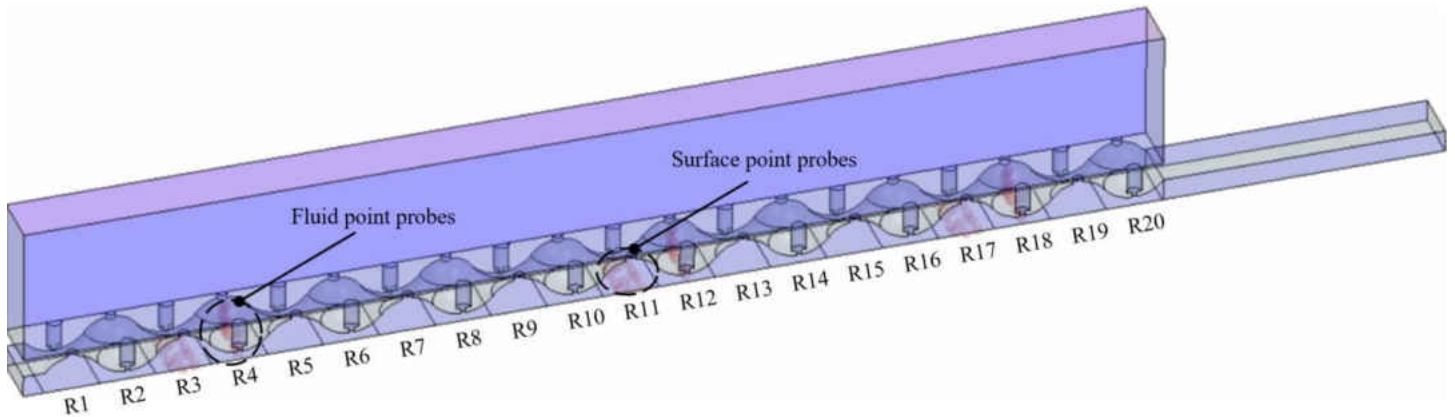
Figure 32: Surface and Fluid Point Probes

Various parameters are monitored for convergence criteria. The residual values

for energy, continuity, and momentum are $> 1 \times 10^{-5}$, while quantities of turbulence such

as turbulence kinetic energy (TKE) and dissipation are of values of $> 1 \times 10^{-4}$ are used as

determinants of the convergence criteria. Quantities of surface heat flux, temperature,

pressure, and velocity are additionally monitored as convergence checkers. The solution

convergence criteria are determined when $> 0.5\%$ change is observed in most of the above

quantities over 2,000 iterations.

Symmetry and periodic boundary conditions are compared in this study to show

the effects of the spanwise extents. The result influence of a full pitch as given by a

periodic side and a full pitch by periodic side boundary conditions. Figure 33 shows a

comparison between the effect of side boundary condition on the prediction of the area-

averaged Nusselt number. These results are compared to the experimental data for $Re_{av,j}$ = 9,000, and $Z/D_{av,j}$ = 2.87.

The results from Figure 33 show a minimal difference in the predicted Nusselt number. For both cases, the symmetry and periodic side boundary conditions, the maximum difference is seen in row 6. The maximum difference between the boundary conditions is ~ 2.4%. From the results, it can be concluded that a numerical study with the half-pitched model is sufficient for the capturing of the salient features of fluids flow and heat transfer due to the jets and the pimple-dimpled features. Throughout this study, the half-pitch model is deemed sufficient. The results agree with the experimental data and are within the total experimental uncertainty.
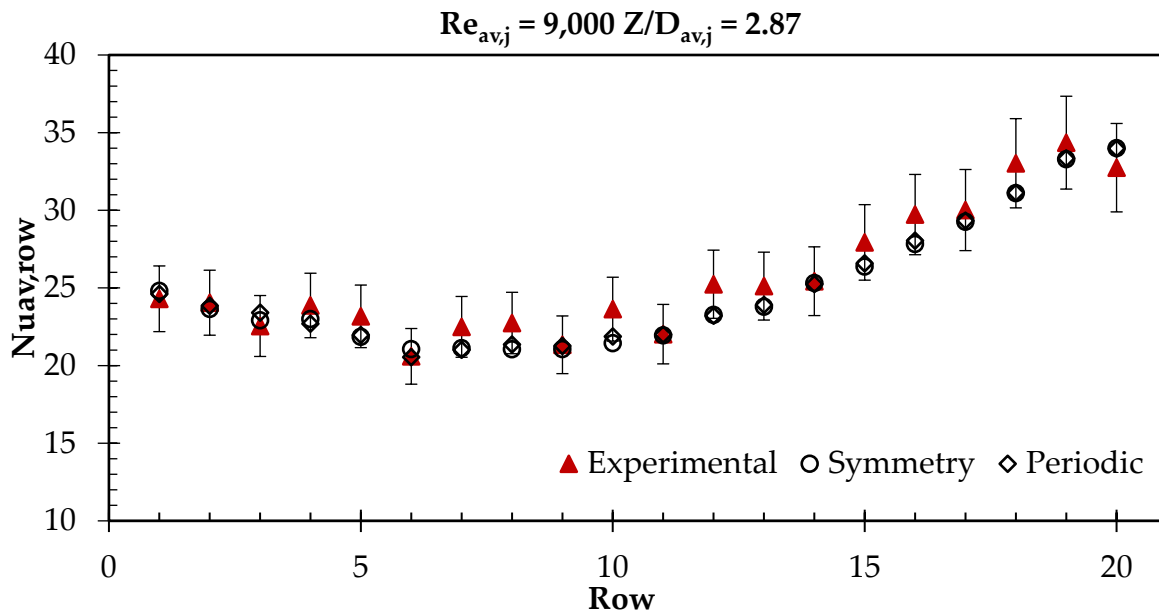

Figure 33: Comparison of Side Boundary Condition

Turbulence Models

Due to the anticipated complexity of fluid flow as a result of interactions between the pimples, dimples, and jets, it was of interest to see which turbulence model works best. Validation of different Reynolds Averaged Navier-Stokes (RANS) turbulence models against experimental data is performed, and a recommendation for the best matching turbulence model is made.

Validation of turbulence models is selected due to the anticipated high levels of turbulence and flow interactions. Strong recirculations in the dimples and around the pimples are expected to occur. The localized impingement regions are also affected and not expected to behave in a way such that it does in a flat plate configuration. These make the flow for the NPR configuration complex, and the selection of a single turbulence model is a hard choice. Extensive studies included a variety of 2-equations, and Reynolds stress turbulence models are evaluated in this study.

Reynolds Averaged Navier-Stokes Equation (RANS)

- Realizable κ–ε (RKE): The Standard κ–ε model is not very accurate for flows with an adverse pressure gradient, strong curvature to the flow, and jet flows. It uses the wall function, so flow in the buffer region is not simulated. This model performs well for external flow with complex geometries. It has very good

convergence rate. The low Reynolds number extension of this turbulence model requires a denser mesh in the near-wall region; its low Reynolds number property dampens the turbulence. The low Reynolds number extension improves its lift, drag, heat fluxes, separation, and reattachment. The RKE model contains a new transport equation for the turbulent dissipation rate. In addition, one of the models constant is expressed as a function of mean flow and turbulence properties in place of a fixed value. The variable coefficient all the model to satisfy particular mathematical constant on the normal stress consistent with the physics of the turbulence. This improves the accuracy of the model substantially and makes it most suitable for our applications since we have strong turbulence generated by the secondary structure from the dimples and protrusions

- K–ω – SST: It is a combination of the κ–ε in the free stream and κ–ω model near the wall. It is a low Reynolds number models and needs finer mesh near the wall. It performed well for the jet and separated flow but it the current situation we have a combination of two, and this model fails to predict the heat fluxes correctly

- K–ε – lag Elliptical Blending: This model additionally solves for a scalar for the normalized wall-normal stress component and elliptic blending factor to determine the turbulent eddy viscosity. The traditional linear eddy viscosity

models are incapable of accounting and any misalignment in the principal component of stress and strain, which result due to the non-equilibrium effects in most 3-D turbulent flows. This results in over-prediction of turbulent kinetic energy. Therefore, this improves the capability of modeling the effect of anisotropy, curvature, and rotational flows. Most of the turbulence models tried in this study over-predicted turbulent kinetic energy, which is manifested by over-prediction in heat fluxes. Therefore, this model is considered and expected to give a better prediction, which did not happen.

- K–ε – v2f: Close to the wall, the fluctuations of the velocity are much higher in the wall-parallel direction as compare to wall-normal direction, and velocity fluctuations are anisotropic. This anisotropy declines with increasing distance from the wall, and flow fluctuations become isotropic. The v2-f model introduces two new equations, which account for the transport of turbulent velocity fluctuations normal to the streamlines and wall-induced damping of the redistribution of turbulent kinetic energy in the parallel and normal directions. This model is recommended for flows over curved surfaces. Dimples and protrusions have curved surfaces, and it is worth looking at the performance of this model in predicting the flow and heat fluxes in this case.

- K–ω-SST: The κ–ω model has previously performed well in literature for flow that exhibits strong curvature, internal flows, jets, and separated flows. The SST model It is a combination of the k-epsilon in the free stream and k-omega model near the wall. It is a low Reynolds number models and needs finer mesh near the wall. It performed well for the jet and separated flow, but it the current situation, we have a combination of two, and this model fails to predict the heat fluxes correctly.

Figure 34 shows the comparison of surface heat flux for five turbulence models against test data for $Z/D_{av,j}$ = 2.87 and $Re_{av,j}$ = 9,000. Coefficients of all the turbulence models are maintained at default values. Maintaining the default values ensures that the selected model keeps its universality and allows for easier replication. Even though changes to those coefficients may yield better results for specific cases (change in $Re_{av,j,}$ or $Z/D_{av,j}$), these changes may affect the other cases as well.

The κε-v2f turbulence model shows some significant over prediction in heat flux up to the 10th row. In the crossflow dominated region rows 11-20, the model fails to predict the heat flux within the total experimental uncertainty. A maximum difference of ~ 41% is seen in row 14 when compared to the testing data. The general trend of the heat flux is not matched in this model and is not selected for this study.

The κ–ε-RSM model predicts the surface heat flux when compared to the experimental results. This difference, however, is < 20% in most of the rows. Compared to the κ–ε-v2f, this model also fails to capture the general trends of the surface heat flux with less error.

A better prediction that the κ–ε-v2f and the κ–ε-RSM is observed in the κ–ω-SST model. Even though it overpredicts the surface heat flux in the region (rows 1-15), the over prediction is not as drastic when compared to the κ–ε-v2f and the κ–ε-RSM models. Despite not being within the experimental uncertainty in that region, this model well predicts the heat flux in the last five rows. The maximum difference between the experimental data and the prediction is seen in row 11, with a 24 % difference. The general trend is not predicted here.

The κε-lag with elliptic blending over predicts the heat flux overall. The trends seen here are with an agreement with what the κ–ε-v2f model predicts. A maximum over prediction is at the middle rows of 6-14, with a difference being as high as 36%, compared to the testing data.

The best predicting turbulence model here is κ–ε realizable. This model shows a very good prediction of surface heat flux when compared to the data for all 20 rows with proper capturing of the general trend in the data. Slight variations, namely at rows 6, 9,

11, 14 and 20 are seen here, and could be due to slight fluctuations in the experimental testing data and does not necessarily imply physical fluctuations.

Comparing the above turbulence models, the RKE turbulence model is well predicting the surface heat flux and the general data trend. Therefore, this model has been selected and used for all further numerical simulations.
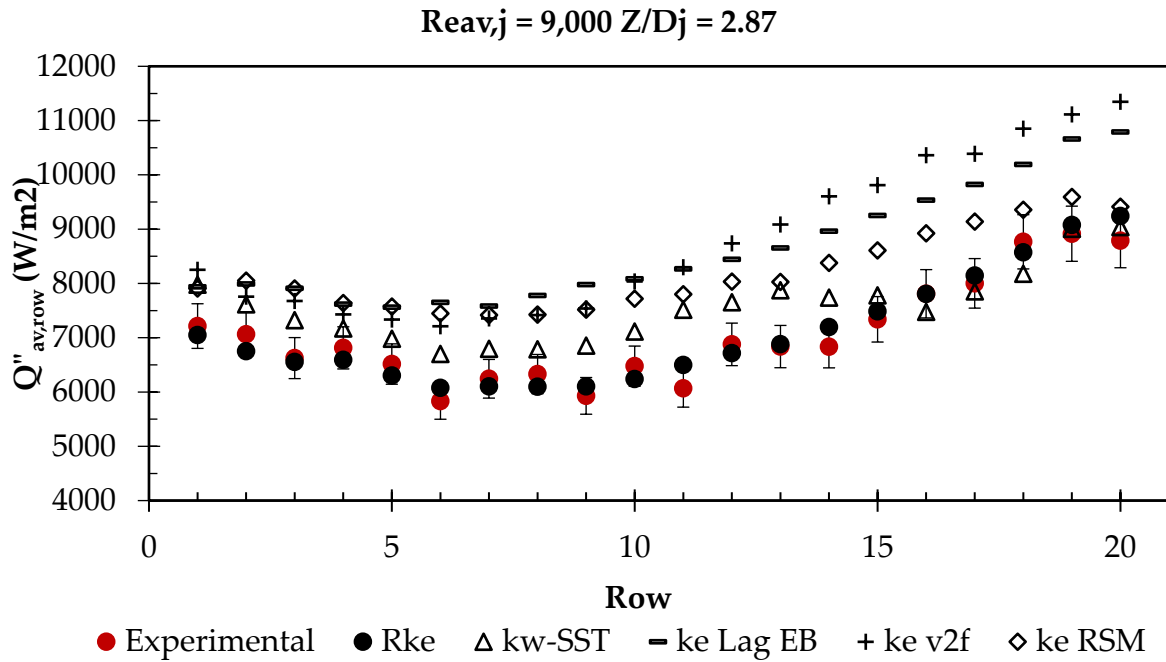
Reav,j = 9,000 Z/Dj = 2.87

Figure 34: Comparison of Predicted Surface Heat Flux Using Various Standard Turbulence Models for NPR Plate

CHAPTER 7:   HEAT TRANSFER MODELING

Statistical methods of multiple regression using logarithmic functions are used to build correlations for the flat and the pimple-dimple plates. The results are reported in the analysis of variance (ANOVA) tables. In order to employ statistics for both plates, two sets of variables were identified:

- Response Variable:

  o Area-averaged Nusselt number ($Nu_{av,global}$)

- Explanatory Variables:

  o ($Z/D_{av,j}$), the jet-to-wall spacing

  o ($Re_{av,j}$), the jet-averaged Reynolds number

The analysis carried out in this chapter uses a multivariable and non-linear regression, with a least-squares objective function based on the dependent variable, Nusselt number. This approach was chosen since the local, or relative, deviation, as appears by outliers in the data, is minimized.

Since the model exhibits more than a single explanatory variable, multiple regression is obtained. Often, researchers utilize powers and multiplicative formulas to correlate area-averaged Nusselt numbers, such as in Equation (7-1). Where the F-test is used for the three coefficients of regression to evaluate the model's confidence.

$$Nu_{av,global} = a \cdot Re_{av,j}{}^{b} \cdot \left(\frac{Z}{D_j}\right)^{c} \tag{7-1}$$

At some times, correlations from studies performed by other researchers in [99], for example, include other explanatory variables such as the nozzle effective open area ($A_{av,j}$), Prandtl number (Pr) and the streamwise-to-jet diameter ratio ($X_n/D_{av,j}$). In this study, however, the effective open area for the jets was maintained constant and is given in Equation (7-2)

$$A_{av,j} = \pi \cdot \left(\frac{D_{av,j}}{2}\right)^{2} = 153.06 \text{ mm}^2 \tag{7-2}$$

Since the Prandtl number is assumed a constant number of 0.709, calculated based on the physical properties of the jet, this value is combined in the constant correlation. The ratio of streamwise-to-jet diameter is also kept constant and is accounted for in the constant term (a). Equation (7-3) shows the transformation of Equation (7-1) to a base 10 logarithmic form.

$$\log_{10} Nu_{av,global} = \log_{10} a + b \cdot \log_{10} Re_{av,j} + c \cdot \log_{10}\left(\frac{Z}{D_j}\right) \qquad (7\text{-}3)$$

In the subsequent sections, the best fit value for the coefficient and the exponents are presented.

CHAPTER 8:   HEAT TRANSFER RESULTS

The present paper discusses heat transfer experiments with validation for multiple

works found in the literature. A multi-jet impinging array. An array of (26 x 20) circular

orifices emanating from a pimpled-dimpled and, flat surface, impinge on a flat, heated

target wall. In this experimental work, the effects of jet-averaged Reynolds number

($Re_{av,j}$), and Jet-to-plate distance ($Z/D_{av,j}$) on heat transfer defined over a span area, are

studied. Reynolds numbers tested are 5,000, 7,000, and 9,000. Jet-to target plate distances

tested, are 2.4, 2.87, 3.25, 4, and 6.

An Overall Energy Balance

An overall energy balance is carried for the testing setup for $Re_{av,j}$ = 9,000 and $Z/D_{av,j}$

= 2.87. The fundamental heat transfer across the entire control volume can be given by

the multiplication of the mass flow rate and the enthalpy addition:

$$Q_{in}\text{-}Q_{loss}= \dot{m}_{tot}c_p(T_{out,j}\text{-} T_{in,j}) \tag{8-1}$$

For the abovementioned case, one of the cases is selected, i.e., the high-

temperature test. The mass flow rate for this case is 0.252 kg/s. The averaged temperature

of the inlet air given by the temperature at the plenum and the outlet air measured is used

to find the averaged value for specific heat capacity at constant pressure. At 330 K, the

specific heat is 1,008 J/kg.K. The temperature of the air in the plenum is ~ 330 K and increases by ~ 3.9 degrees towards the exit of the testing section.

The heat lost due to conduction is calculated based on the detailed heat leakage section on page 56. Heat loss due to conduction is ~ 69.2 W. The supplied into the system is based on the outlined procedure in the previous section is ~ 1,019.2 W. The total heat into the system as calculated from the energy balance is found to be ~ 990.7 W. There is about 2.8% difference in the calculated and the actual energy balance which is acceptable. This difference could be due to uncertainty errors in temperature reading, which also affects the value of the specific heat used.

Validation and Flat Plate

In the past, different geometrical and flow parameters have been involved in the study of arrays of multi-jet impingement. For validation purposes, results from previous studies are compared to the present work. Here, a single Nusselt number is calculated by averaging globally over the entire area of the heated sections. Florschuetz et al. [27], Kercher, and Tabakoff [56]. Their correlations are compared to the present work for the flat, baseline plate in Figure 37. Florschuetz et al. showed their correlations for staggered and inline jets. A correlation for maximum crossflow is proposed in the form:

$$Nu_{av,row} = A.Re_{av,j}^{m}.(1-B.[(Z/D_j)(G_c/G_j)]^n).Pr^{1/3} \qquad (8\text{-}2)$$

Where

A, B, m and n   geometrically dependent parameters

G_c/G_j ratio of crossflow-to-jet velocity. Equation (8-3)

$$\frac{G_c}{G_j} = \frac{1}{\sqrt{2}\,C_d} \cdot \frac{\sinh\beta\,\left(\frac{X}{X_n} - \frac{1}{2}\right)}{\cosh\beta\,\left(\frac{X}{X_n}\right)}$$
(8-3)

$$\beta = \frac{C_d \cdot \sqrt{2} \cdot \left(\frac{\pi}{4}\right)}{\left(\frac{Y_n}{D}\right)\left(\frac{Z}{D}\right)}$$
(8-4)

Where

G_c/G_j The ratio of crossflow to jet velocity.

Figure 35 explores these values for all the $Z/D_{av,j}$ investigated in this study. On the

y-axis, the center of the copper block location is at every 0.5 X/X_n location due to a

normalized initial distance between the beginning of the testing section and the first jet

(X/X_n) of 0.5. In this plot, the crossflow velocity G_c is found using the summation of the

mass flow rate right upstream of each copper section. Here, results are based on a 1-D

model represented in [90]. It can be seen in the figure that the lower the $Z/D_{av,j}$, the lower

the linearity becomes in the trends. This ratio represents the local jet's mass flux or

relative strength and is an important parameter that is detrimental to the quantification

of how much the jet deflects and degrades due to crossflow[29]. It is apparent from these

results that for a flat plate scheme, the crossflow velocity rather dominates and contributes to up to ~65% of the jet's velocity in the downstream sections as the jet-to-wall spacing decreases. This phenomenon will be rather useful in the analysis of the NPR plate. As a high enhancement is seen, in the downstream sections. Namely, where the crossflow dominates, and also, with lowering the jet-to-target wall spacing.
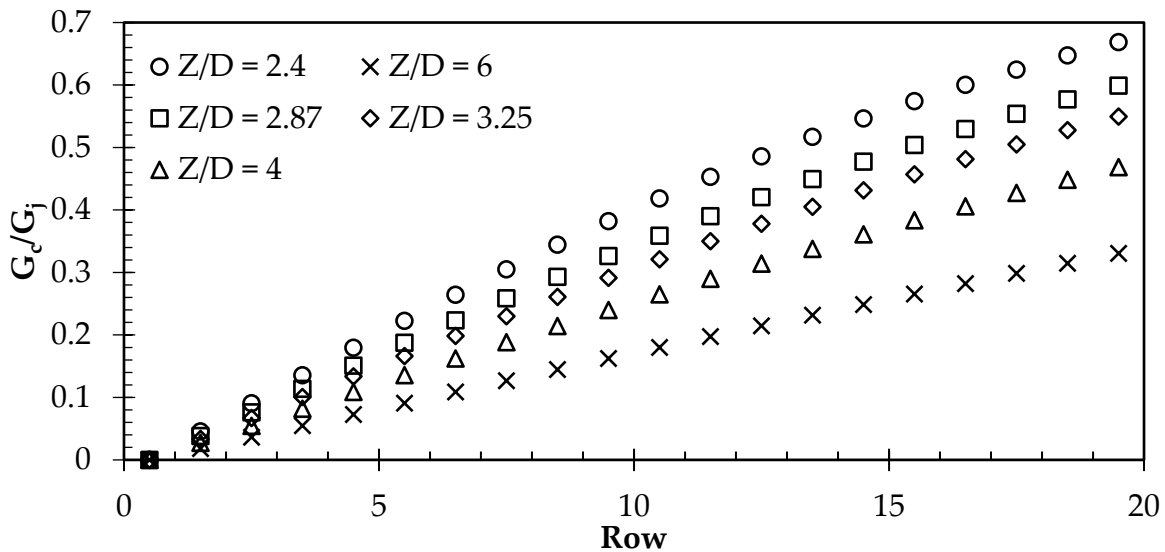

Figure 35: Distribution of Streamwise Jet Velocity Ratio Model

Florschuetz et al. included two correlations for their work: one that involves a two-test method, and another that involved a single test. They will be referred to in the text as correlation 5.1 and correlation 5.2. One major difference between the two is that the one-test correlation (5.2) involves an estimation of the jet's reference temperature. As

explained in CHAPTER 4:, the jet's reference temperature is calculated based on a two-equation two-unknown method for higher accuracy.

In Figure 36, the normalized row-averaged Nusselt number is shown for $Re_{av,j}$ = 9,000 and $Z/D_{av,j}$ = 2.87. Data from correlations 5.1 and 5.2 match each other quite well for this inline configuration and given Reynolds number as well as $Z/D_{av,j}$. When the $Z/D_{av,j}$ increases, the correlations start to deviate from each other, and the error becomes more apparent. The experimental data showed here match the correlations for Nusselt number of Florschuetz in the first 15 rows within the total uncertainty of this study, except for the data point at row 6. This could be due to an experimental error and could not be justified as physical. It is worth noting the higher trend seen for rows 15 to 20. While either Florschuetz's correlations did not pick up the trend seen experimentally, they designed and built their correlations based on ten rows. This study investigates 20.
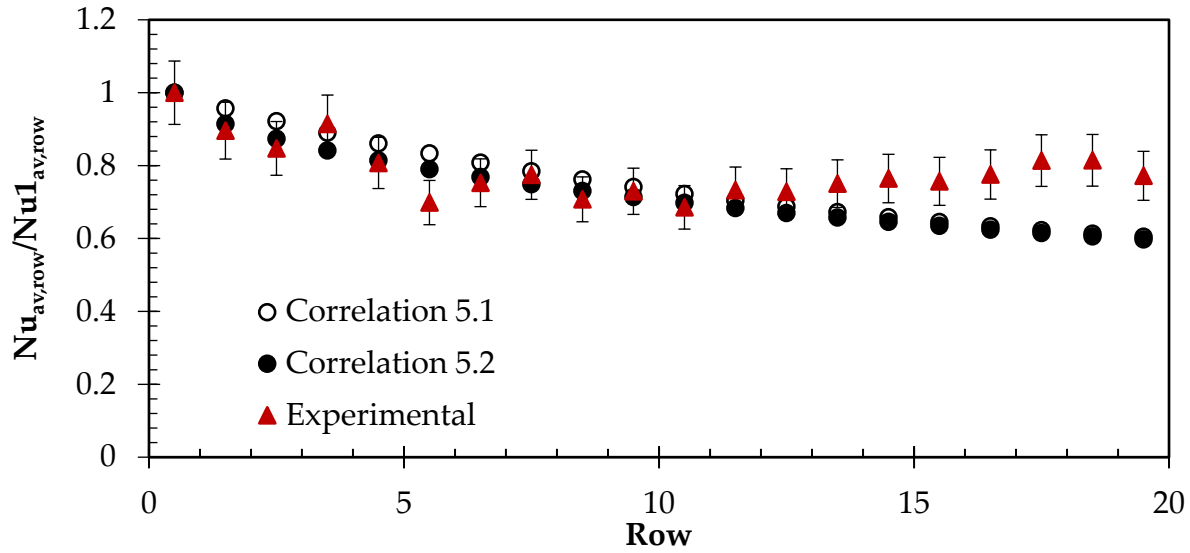
Figure 36: Normalized Area-Averaged Nusselt Number; Re = 9,000, $Z/D_{av,j}$ = 2.87

Kercher and Tabakoff studied multi-jet impingement for different numbers of jets, X, and Y spacing while maintaining an equal ratio (X/D_j = Y/D_j), and jet diameter. Their correlation was built based on these combined parameters in the form of

$$Nu_{av,row} = \varphi_1.\varphi_2.Re_{av,j}{}^m. (Z/D_j)^{0.91}.Pr^{1/3} \tag{8-5}$$

where

φ_1, φ_2 constants that vary with geometrical parameters

m   experimentally determined exponent.

Results from this present study are averaged over the global target wall area to produce an averaged Nusselt number plotted with respect to Reynolds number. The jet-to-wall spacing in Figure 37 was fixed at $Z/D_{av,j}$ = 3.25 for comparison purposes, as this

101

number serves as the middle of the range of $(Z/D_{av,j})$ in this study. The correlations of Florschuetz et al. and Kercher et al. show a maximum deviation of ~ 3% and ~ 6%, respectively, when compared to the present data.

The results of the Nusselt number from the present study are comparable to those shown in Figure 37. The obtained results lie within the error bands of the experimentally attained values of Nusselt number. The agreement between the classical impingement correlations and present work provides confidence to the heat transfer measurement for the pimpled-dimple plate configuration as well.
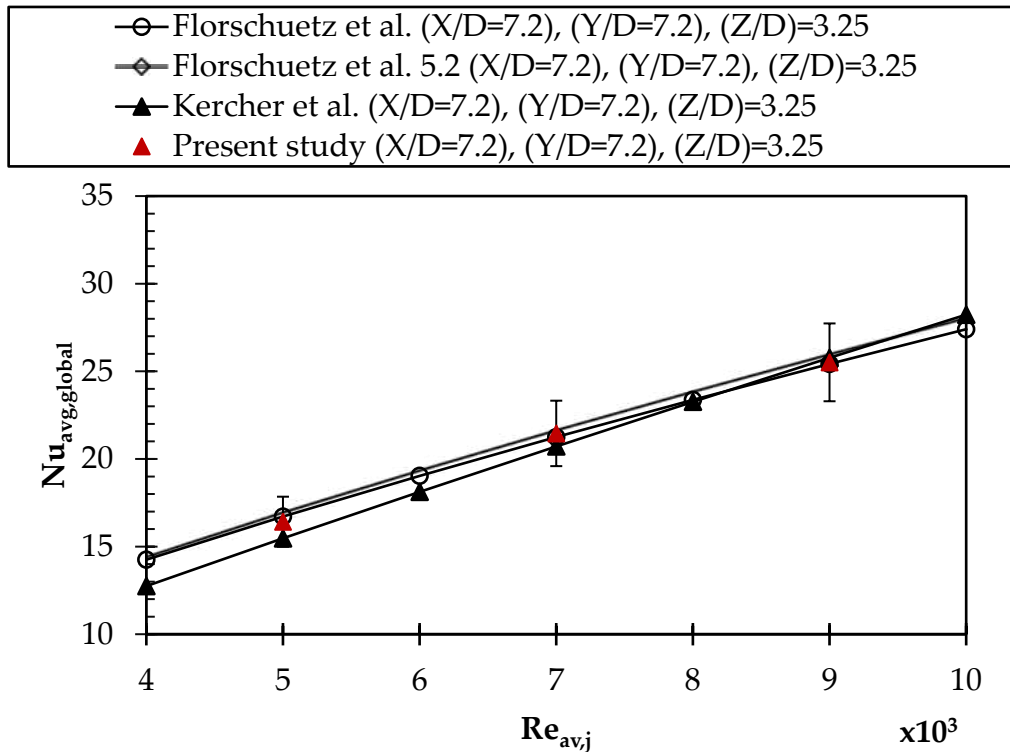
Figure 37: Comparison of Literature Data with Current Study

Comparison with Pimple-Dimpled Jet Plate

Nusselt number is calculated according to the span-averaged methodology described in the Heat Transfer section on page 61. Figure 38: Experimental Row-averaged Heat Transfer for $Re_{av,j}$ = 5,000 – Flat Plate. Figure 38 and Figure 39 show the rig distribution of the span-averaged Nusselt number (each point corresponds to a row copper block). Only the case of $Re_{av,j}^m$ = 5,000, is presented, as similar trends are seen for the two other Reynolds numbers. Initially, the testing matrix included $Z/D_{av,j}$ = 2.87, 4, and 6. However, the trends seen in Figure 39 showed that there's a considerable gap in the data between ($Z/D_{av,j}$) of 2.87 and 4, especially in the dominant crossflow region shown in the red boxes. Therefore, an additional case of $Z/D_{av,j}$ = 3.25 was introduced, to provide better insight into the effect of ($Z/D_{av,j}$) on heat transfer.

Even though heat transfer decreases for the flat impingement plate, this is the opposite of the pimple-dimpled plate. Thus, the lowest ($Z/D_{av,j}$) of 2.4 is also included in the study for comprehensiveness. It is clear from this plots that there are two distinct regions, from this section on, the analysis of heat transfer and fluid flow will be based on two observed regions within the channels: (a) impingement dominant region of sections 1-10, and (b) crossflow dominant region of 11-20. From this section on, heat transfer analysis will be broken down by these two regions.

In the case of jet impingement from the flat plate, and pimple-dimpled plates, a coupled effect of impingement and channel flow exist. In the impingement case, the shear layer thickness of the jet increases, with increasing the $(Z/D_{av,j})$ before impacting the target surface, i.e., at higher $(Z/D_{av,j})$, the jet shear layers are allowed to grow before impingement. The kinetic energy of the jet is progressively dissipated when the shear layer thickness increases, which causes a drop of Nusselt number locally. It can be observed that the Nusselt number of the pimple-dimpled plate is lower than that of the conventional flat plate. When crossflow develops, however, enhancement of heat transfer is seen specifically with the pimple-dimpled plate as also observed by Gupta et al.[100]. Jet deflection, crossflow induced jet-to-jet interaction, and generation of secondary structures promotes higher heat transfer. These effects will be discussed in the numerical portion of this study. Moreover, the production rate of turbulent kinetic energy is increased, and thus the enhancement of turbulent heat transfer is observed. At the highest $(Z/D_{av,j})$ of 6, impingement region heat transfer is lower in the pimple-dimpled case when compared to the flat plate. In the crossflow region, heat transfer did not seem to be affected.
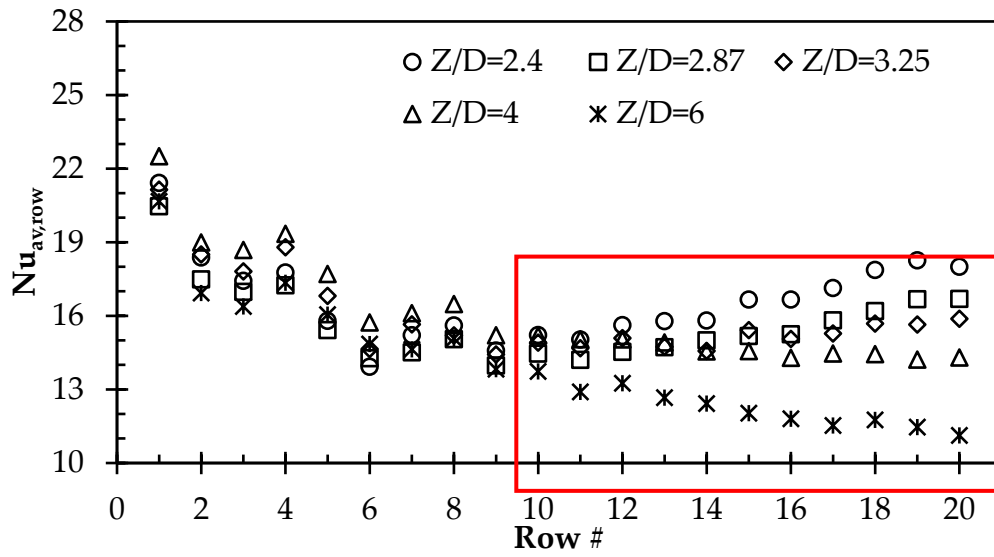
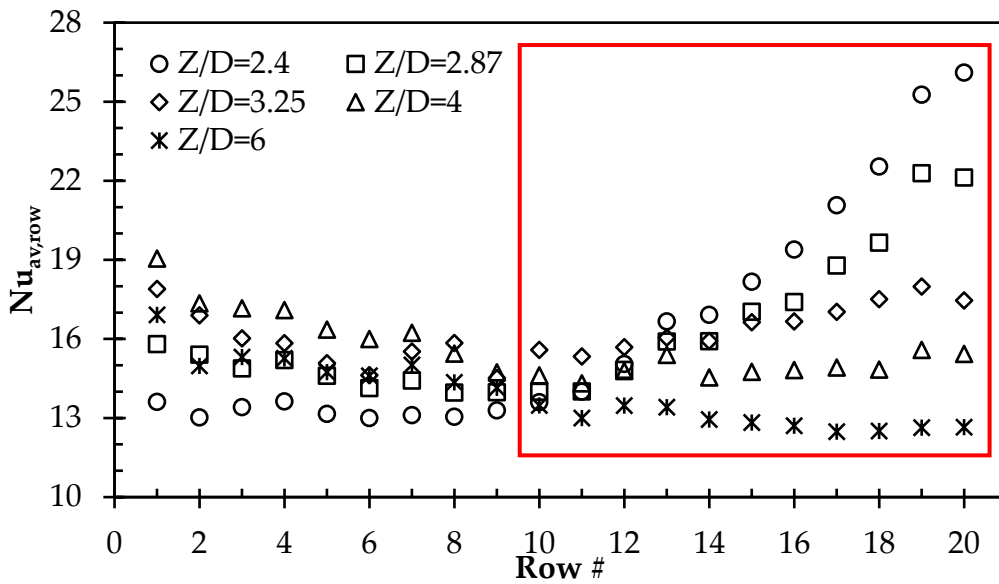*Figure 38: Experimental Row-averaged Heat Transfer for $Re_{av,j}$ = 5,000 – Flat*

Plate

Figure 39: ExperinemtalRow-averaged Heat Transfer for $Re_{av,j}$ = 5,000 -Pimple-

Dimpled Plate

Effect of Jet-to-Wall Spacing

On Flat Plate

The global averaged Nusselt numbers corresponding to different jet-to-plate wall ratios for the impingement region and crossflow region are presented in Figure 40 and Figure 41, respectively. Initially, in the impingement region, it can be seen in Figure 40 that when Reynolds number increases, the spread between the data points for the same Reynolds number remains almost at ~10% at various $(Z/D_{av,j})$. While the data points somewhat overlap, and even with uncertainty bars on the graph, it is visible that $Z/D_{av,j}$ = 4 yields the highest heat transfer in the impingement region. This agreement with Figure 38 and Figure 39 could be because there is little jet-to-jet interaction between the emanating jets. However, in the crossflow region (Figure 41), it can be observed that lower (Z/D_j) ratios yield higher heat transfer due to strongly induced crossflow. Heat transfer at $Z/D_{av,j}$ = 2.4 is superior to that at $Z/D_{av,j}$ = 6.
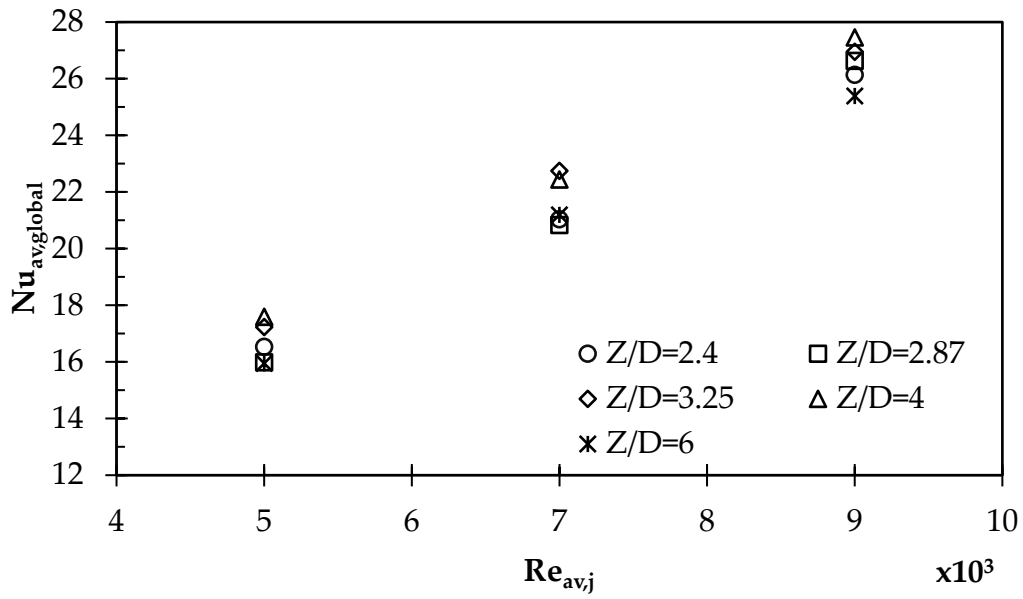
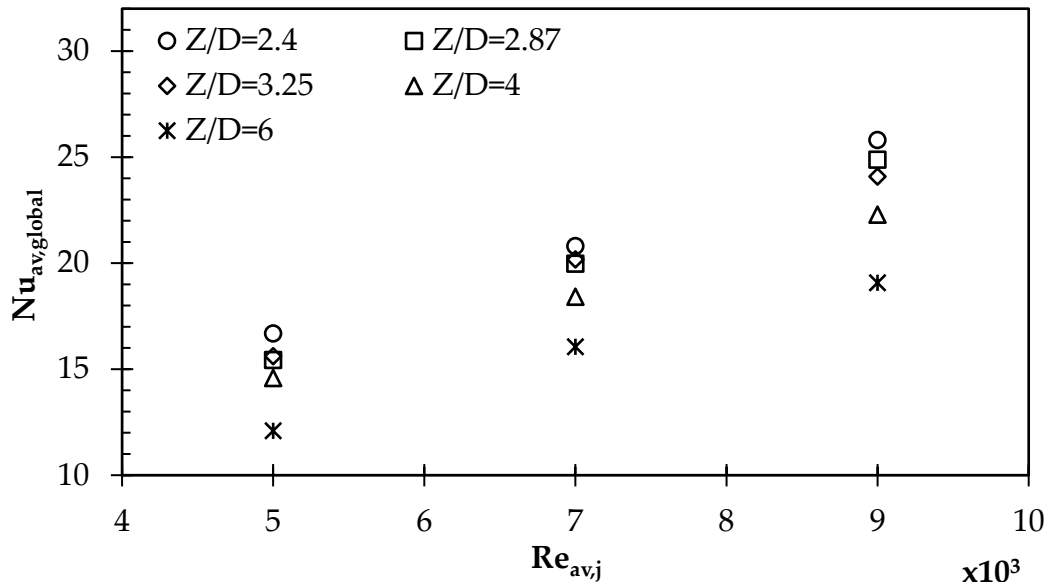*Figure 40: Experimental Global-Averaged Heat Transfer for Flat Plate: Rows 1-10*

Figure 41:Experimental Global-Averaged Heat Transfer for Flat Plate: Rows 11-20
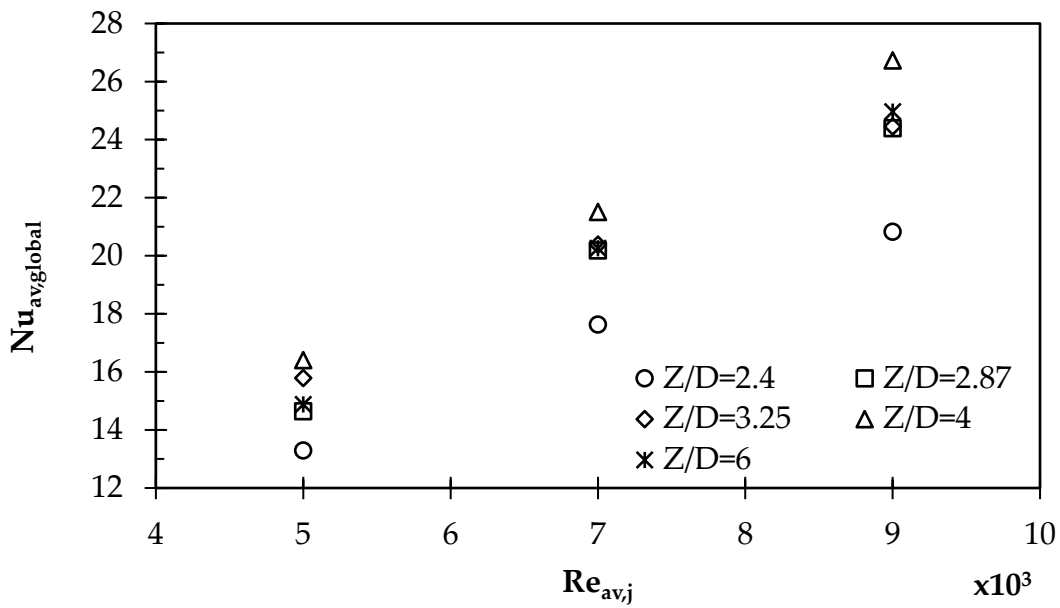
On Pimple-Dimpled Plate

Figure 13 shows the global averaged Nusselt number from the pimple-dimpled plate for rows 1-10 (Figure 42) and rows 11-20 (Figure 43). It can be seen that in the impingement region, the global area-averaged Nusselt number decreases with increasing Z/D_j for all ranges of Reynolds numbers.

Superior heat transfer is obtained from $Z/D_{av,j} = 4$. A similar trend is seen in Figure 40, where the jet plate is flat. However, when introducing pimples and protrusions, the worst-performing spacing is the lowest at $Z/D_{av,j} = 2.4$ for all Reynolds numbers.

Comparing Figure 41 and Figure 43, there is an up to 18% enhancement in the heat transfer in the crossflow region for the pimple-dimpled plate in the low $(Z/D_{av,j})$ cases (2.4 and 2.87). Even though there is some enhancement in higher $(Z/D_{av,j})$ cases, it is $< \sim 10$ % for $Z/D_{av,j} = 3.25$, 4, and 6. Narrower spacing between the jet and the target wall performs best, as expected.

Impingement from the pimple-dimpled plate outperforms the flat one in these downstream regions, as the crossflow helps to generate secondary vortical structures, through interaction with the pimples, and dimples. These other structures, and elevated levels of unsteadiness, aid the enhancement of mass exchange. Moreover, these surfaces aid in a weaker thermal boundary layer since it is renewed at a higher rate than the flat plate.

The impingement region for the pimple-dimpled case sees a maximum detriment of about 20% at the lowest $(Z/D_{av,j})$ of 2.4. At the other end of the spectrum, $(Z/D_{av,j})$ of 6 saw the lowest detriment in a globally-averaged Nusselt number. At low $(Z/D_{av,j})$, jet vortices break up upon the impact on the impingement surface, since this low of spacing can well be within the potential core region which has relatively low turbulence and thus, produces a relatively lower heat transfer compared to crossflow effects. The general detriment trend is attributed to the lack of jet-to-jet interactions between each other in that region.

Figure 42: Experimental Global-Averaged Heat Transfer for Pimple-Dimpled Plate:

Rows 1-10
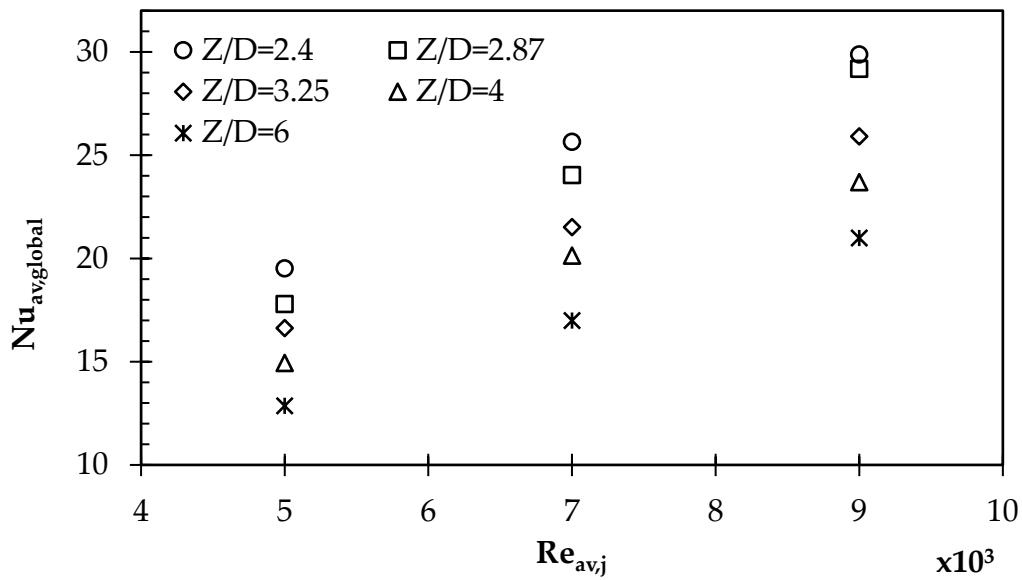
Figure 43: Experimental Global-Averaged Heat Transfer for Pimple-Dimpled Plate:

Rows 11-20

110

Row-by-Row Comparison

Figure 44, Figure 45 and Figure 46 show the row averaged Nusselt number for $Z/D_j = 2.87, 3.25$, and 4 for $Re_{av,j} = 5,000$. It is clear from the plots that for the first half of the rows, Nusselt number decreases with decreasing $(Z/D_{av,j})$, and then for the other half of the rows, this trend reverses. The highest Nusselt number enhancement in the second half of the rows is seen for $Z/D_{av,j} = 2.87$, followed by $Z/D_{av,j} = 3.25$, while a minimal effect is noticed for $Z/D_{av,j} = 4$. It can also be noticed that numerical results matched well with the test data, and differences observed are of the order of experimental uncertainty.

Figure 47 - Figure 49 and Figure 50 - Figure 52 show the comparison of Nusselt number for $Z/D_{av,j} = 2.87$, 3.25, and 4 for $Re_{av,j} = 7,000$ and Figure 50 - Figure 52 show the comparison of Nusselt number for $Z/D_{av,j} = 2.87$, 3.25, and 4 for $Re_{av,j} = 9,000$. For these Reynolds numbers, similar trends are noticed for different $(Z/D_{av,j})$ values, but Nusselt number augmentation for $Z/D_{av,j} = 2.87$ in the second half of the rows is additionally pronounced
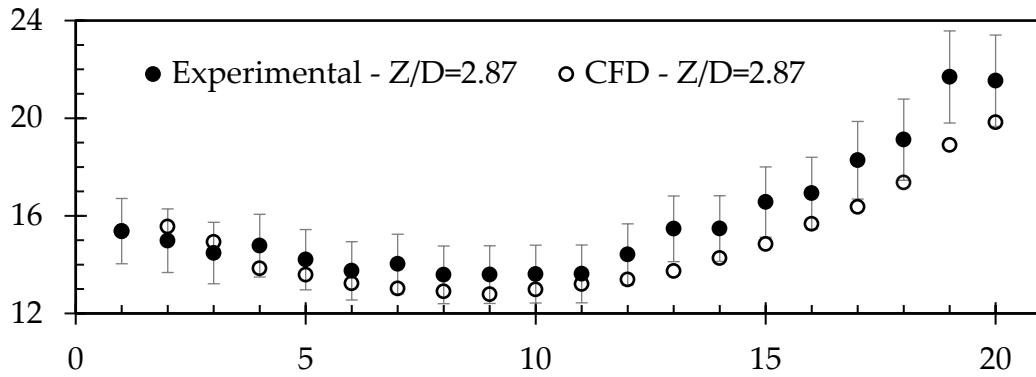
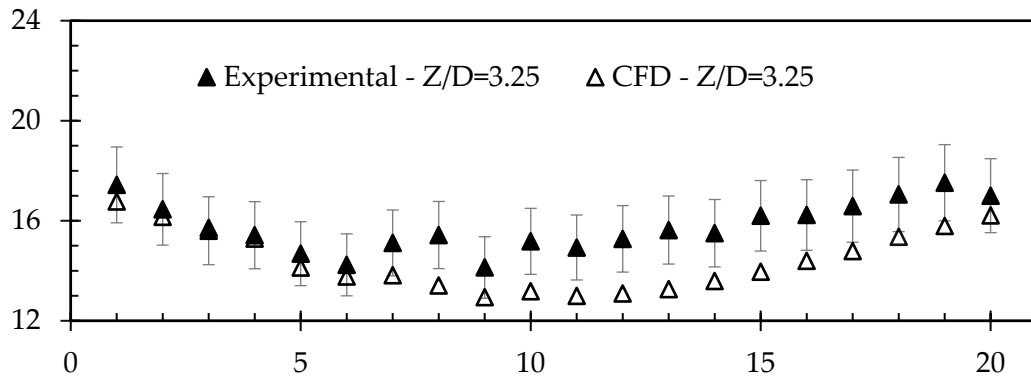*Figure 44: Nusselt Number for $Z/D_{av,j}$ = 2.87, $Re_{av,j}$ = 5,000*

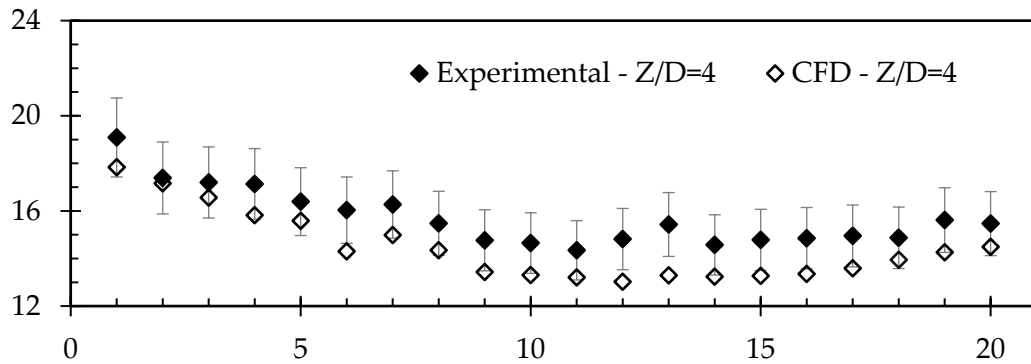*Figure 45: Nusselt Number for $Z/D_{av,j}$ = 3.25, $Re_{av,j}$ = 5,000*

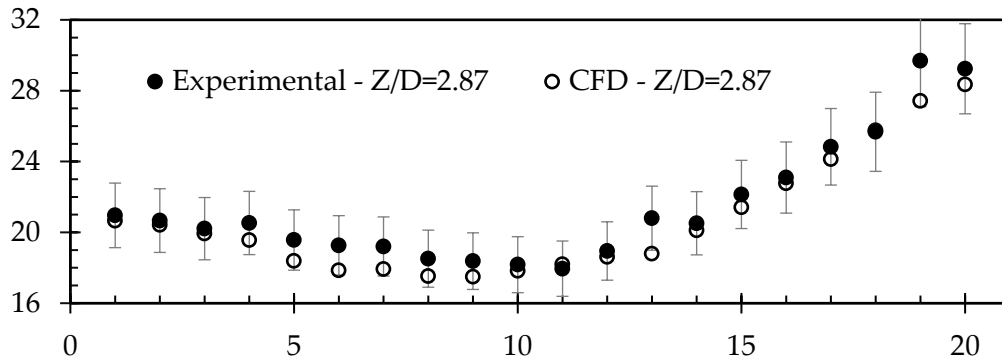*Figure 46: Nusselt Number for $Z/D_{av,j}$ = 4, $Re_{av,j}$ = 5,000*

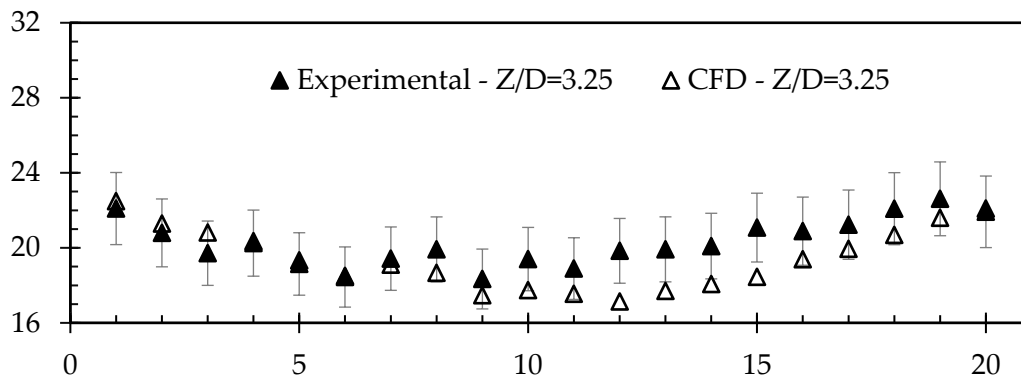*Figure 47: : Nusselt Number for Z/D$_{av,j}$ = 2.87, Re$_{av,j}$ = 7,000*

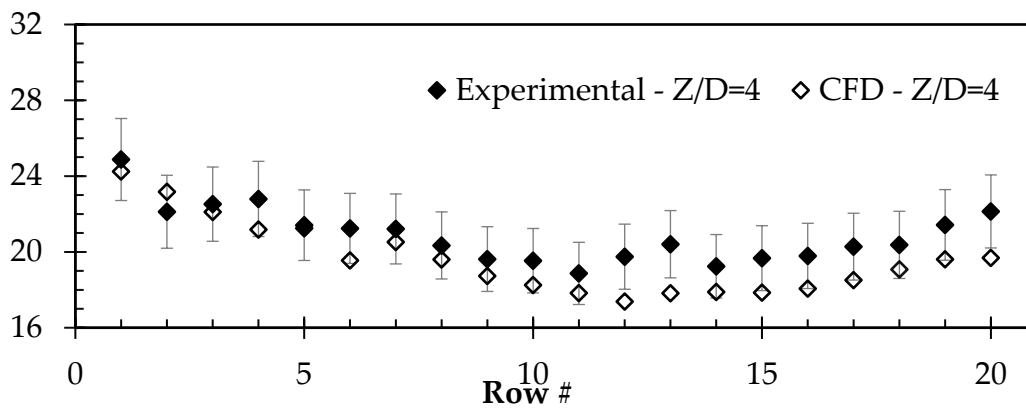*Figure 48: Nusselt Number for Z/D$_{av,j}$ = 3.25, Re$_{av,j}$ = 7,000*

Figure 49: Nusselt Number for Z/D$_{av,j}$ = 4, Re$_{av,j}$ = 7,000
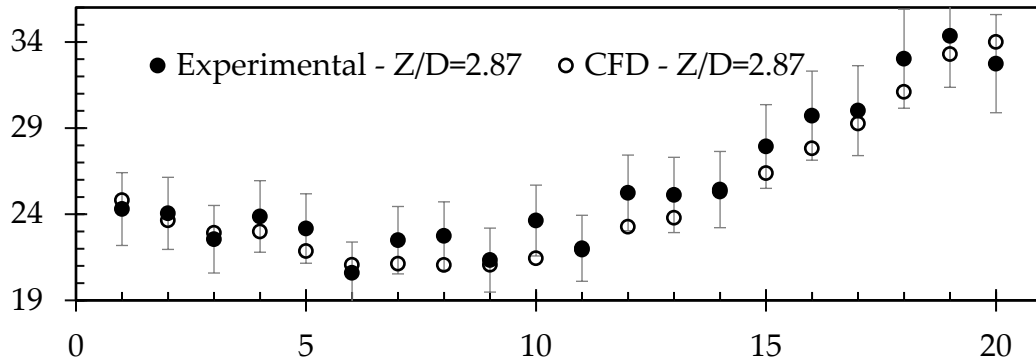
113

Figure 50: : Nusselt Number for Z/D$_{av,j}$ = 2.87, Re$_{av,j}$ = 9,000
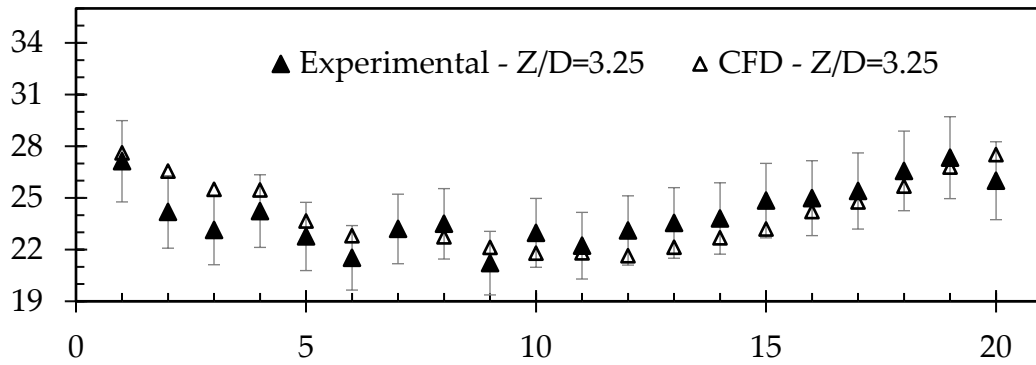

Figure 51: Nusselt Number for Z/D$_{av,j}$ = 3.25, Re$_{av,j}$ = 9,000
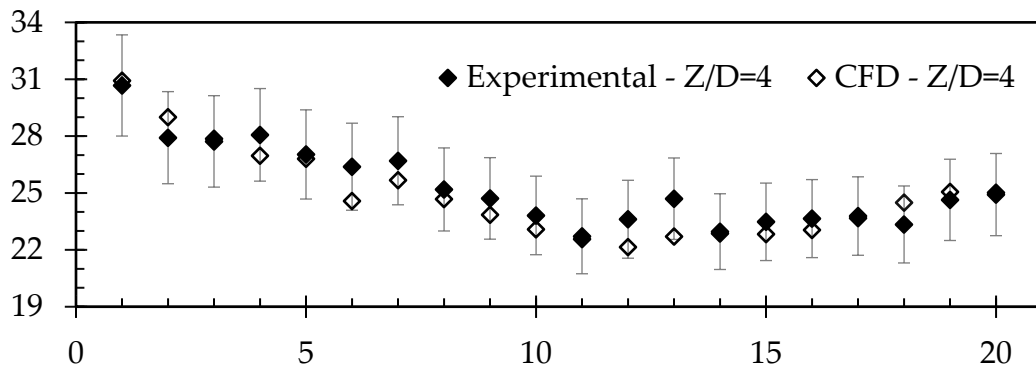

Figure 52: Nusselt Number for Z/D$_{av,j}$ = 4, Re$_{av,j}$ = 9,000

Numerical Surface Heat Flux

The numerical prediction for heat transfer agrees well with test data for both Reynolds numbers as well. Figure 53 shows the comparison of local heat flux for three $(Z/D_{av,j})$ values at a $Re_{av,j} = 5,000$. All the contour plots shown in this figure are for the high target surface temperature case. However, heat transfer patterns remain similar compared to the low target wall temperature case. Note that all numerical data was post-processed in an identical manner as that of the experiment. Hence, two heat flux cases were run per each Reynolds number case (see data reduction section for heat transfer coefficient calculation). As the smaller jet is closer to the target surface compared to the larger jet, its footprint is visible much further downstream than that of the larger jet (due to the lower effective $(Z/D_{av,j})$ of, the smaller jet, it experiences a lower level of jet deflection).

As the $(Z/D_{av,j})$ increases, heat transfer enhancement in the downstream rows 11-20 decreases. An increase in distance from the jets to the target wall decreases the jet impingement strength, as well as the interaction of jets with the vortical structures formed due to the NPR features on the opposite wall. Figure 54and Figure 55 shows the comparison of local heat flux for three $Z/D_{av,j}$ values at $(Re_{av,j})$ of 7,000 and 9,000, respectively. Although the absolute value of heat transfer increases with increasing Reynolds number, there is no significant change in the surface heat transfer patterns.
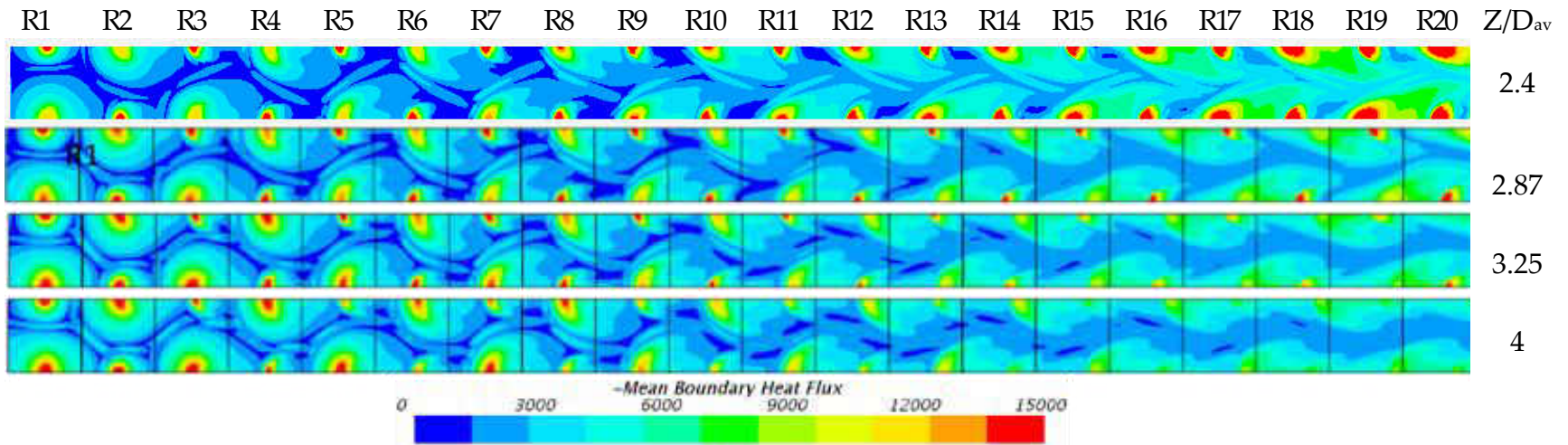
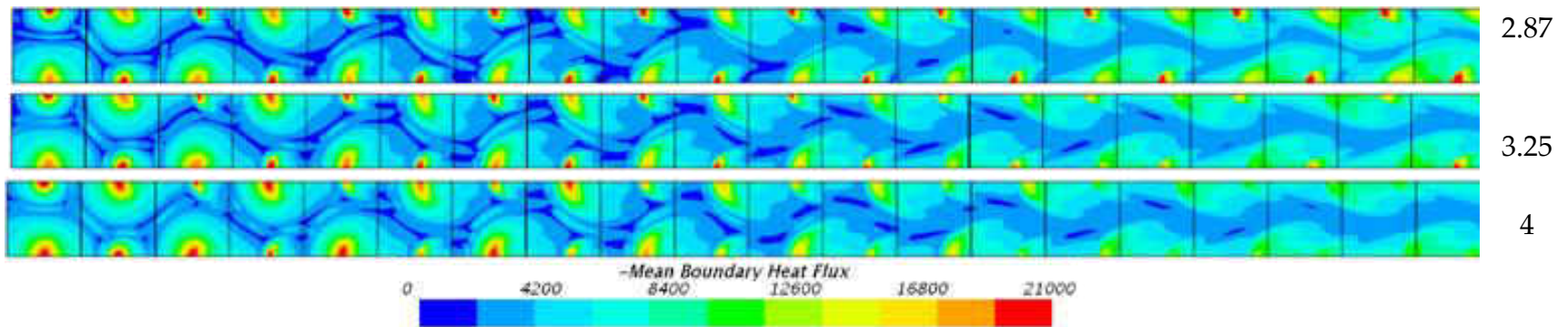*Figure 53: Numerical Surface Heat Flux - $Re_{av,j}$ = 5,000*

Figure 54: Numerical Surface Heat Flux - $Re_{av,j}$ = 7,000
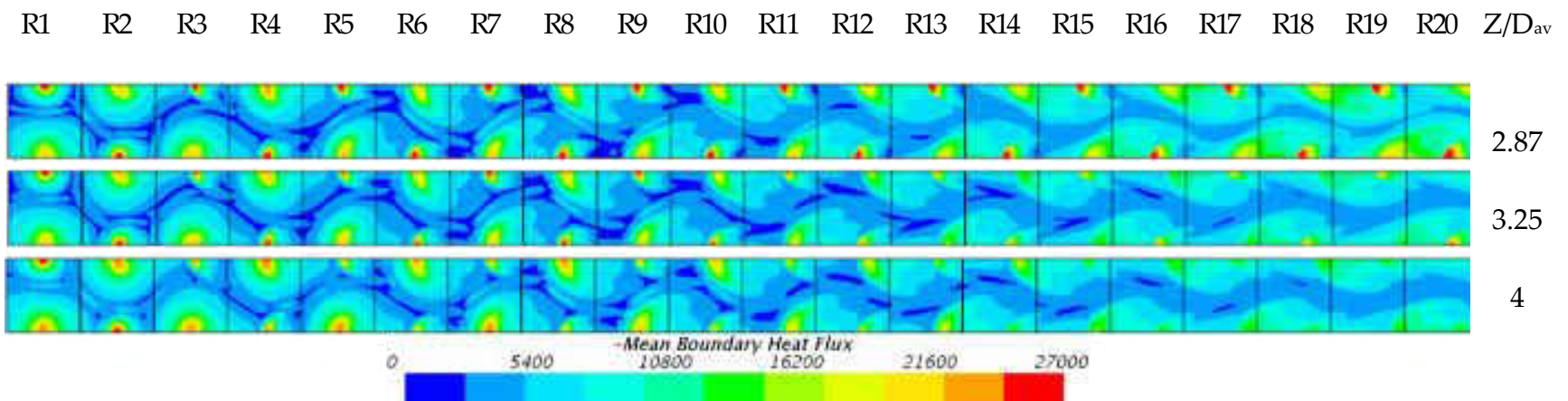
116

Figure 55: Numerical Surface Heat Flux - $Re_{av,j} = 9,000$

Turbulence Kinetic Energy

The iso surfaces for the Lambda 2 criterion is shown in Figure 56 [101] colored by turbulent kinetic energy (TKE) for $Z/D_{av,j}$ = 2.87 and $Re_{av,j}$ = 9,000. The Lambda 2 criterion is used as a vortex identification method and serves to highlight strong, vortical structures that are generated in the flow field. In the first 3 rows of jets (Row 1- Row 3), flow issues from the jets and impinges on the wall, forming some recirculation regions around the jets; these are identified by the iso-surfaces of Lambda 2.
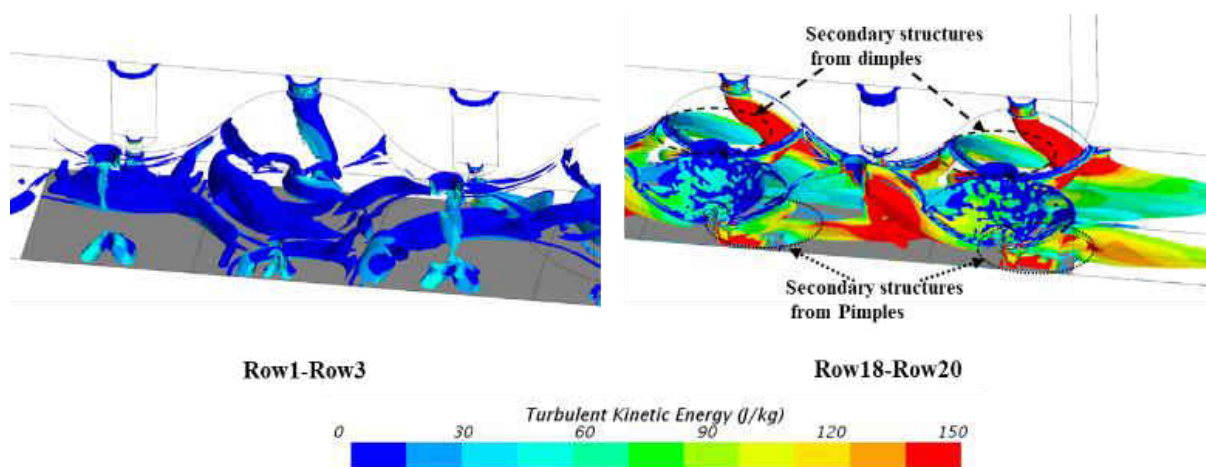

Figure 56: Lambda 2 Iso Surfaces for Select Rows

The TKE in early regions could be lower than that for the flat plate, and the dominant heat transfer mechanism is the impingement of flow on the target surface, which is very localized. Therefore, little to no heat transfer enhancement seen in these rows when compared to a conventional flat orifice plate. However, in the later rows

(Rows 18- 20), secondary structures could form, which are generated by the crossflow interacting with the NPR features. It is well known that when the flow goes over dimples, a counter-rotating pair of vortices forms, and sheds downstream, while for pimples, flow impinges at the front, and then forms a recirculation region on the lee side of the pimple. These additional secondary structures increase the turbulence in the flow, which could be depicted by elevated levels of TKE in these rows. This high TKE is indicative of higher mixing of cold and hot flow, which results in higher heat transfer. Additionally, secondary structures from the dimples shield the jets (by forming a recirculation around it) from the cross flow, and secondary structures from the pimple interact directly with the jets; both these effects enhance heat transfer in these rows. This mechanism of heat transfer enhancement remains unaltered with changes in the Reynolds number, however, as Z/D_j increases, these interactions between jets, secondary structures, and the heated wall, is weakened, resulting in little (or no) enhancement in heat transfer.

Velocity Streamlines

Another method to identify potential flow fields is by investigating the velocity streamlines [101, 102]. Figure 57 and Figure 58 show the surface heat fluxes and the velocity magnitudes for $Re_{av,j}$ = 5,000 for $Z/D_{av,j}$ = 2.4, 2.87 and 3.25.
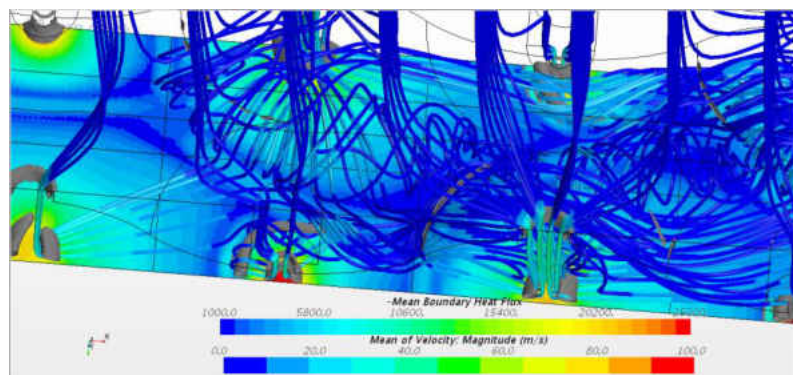
Z/D$_{av,j}$ = 2.4
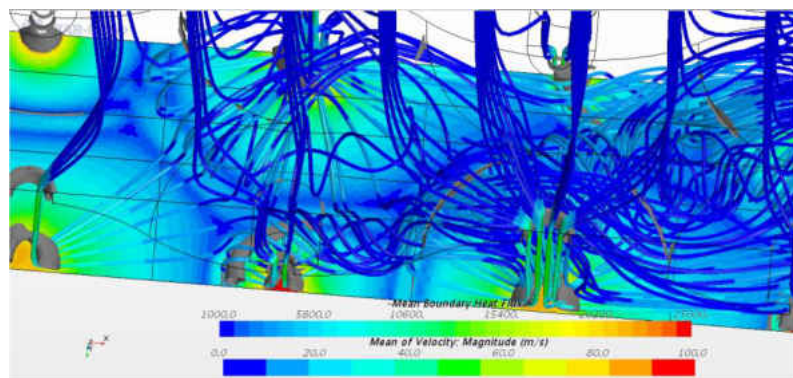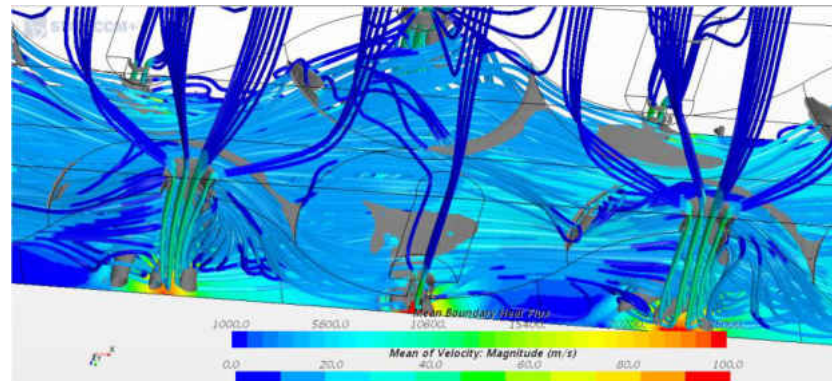
Z/D$_{av,j}$ = 2.87
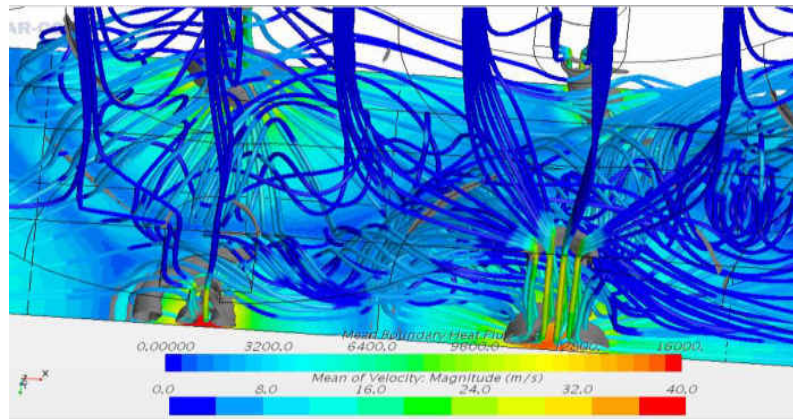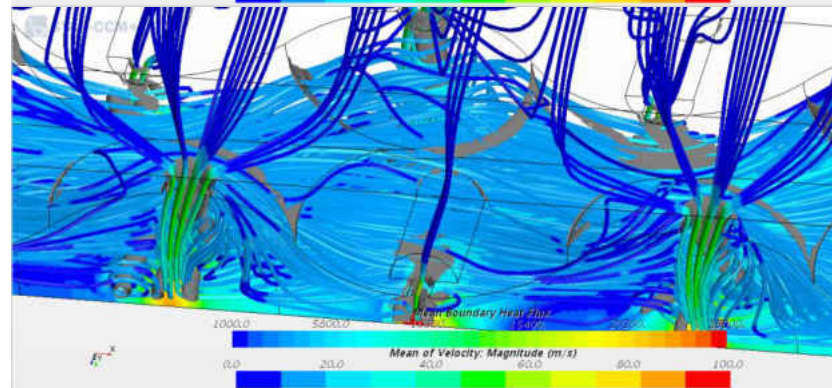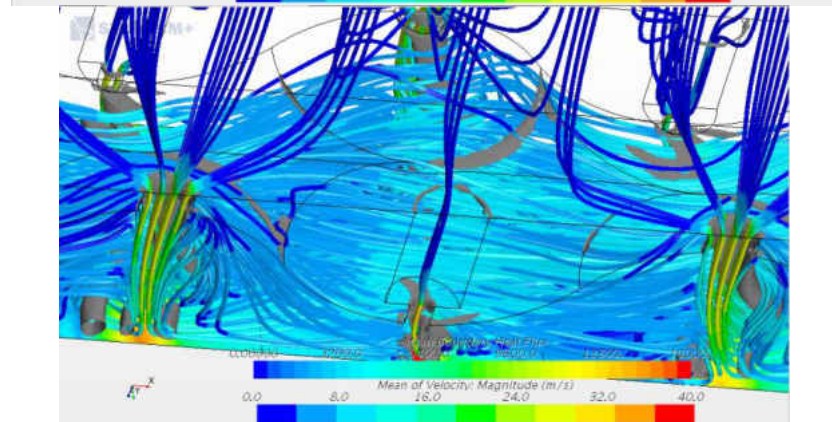
Z/D$_{av,j}$ = 3.25

Figure 57: Surface Heat Flux and Streamlines Re$_{av,j}$ = 5,000, Rows 1-3 (left) and 7-9 (right)

120
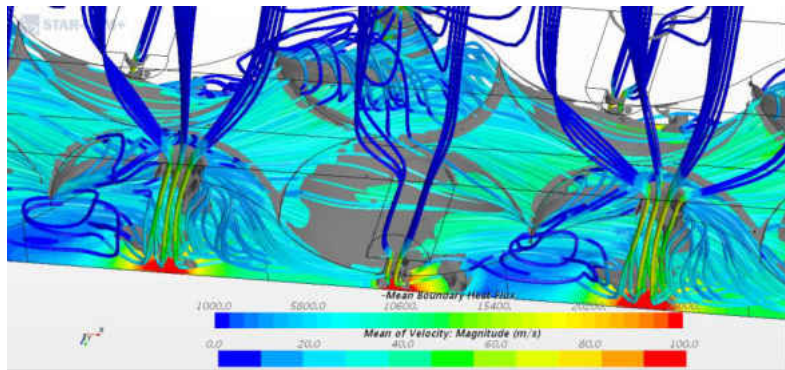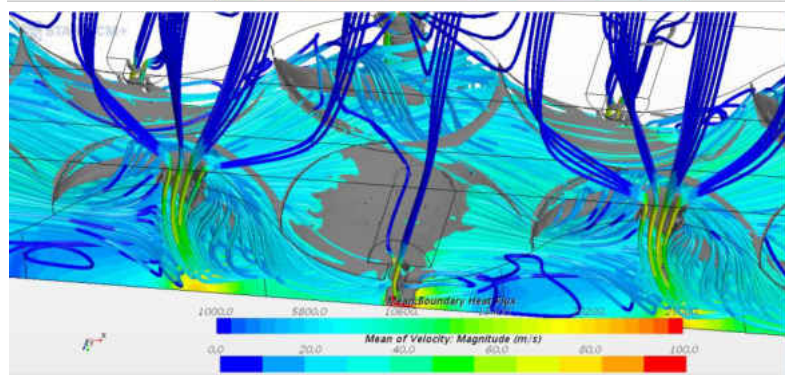
Z/D$_{av,j}$ = 2.4

Z/D$_{av,j}$ = 2.87

Z/D$_{av,j}$ = 3.25
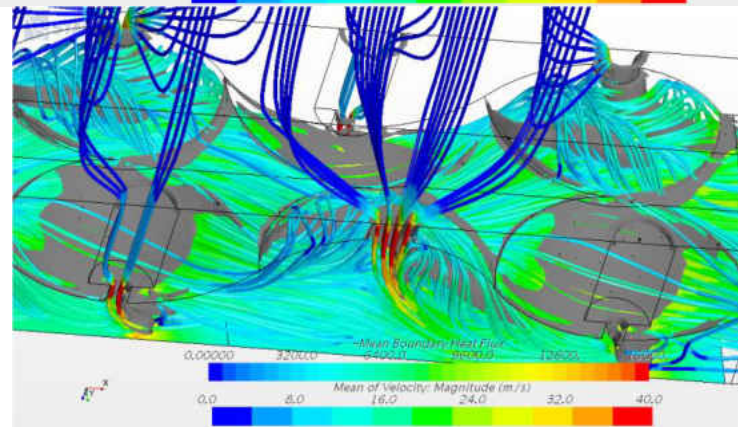
Figure 58: Surface Heat Flux and Streamlines Re$_{av,j}$ = 5,000, Rows 13-15 (left) and 18-20 (right)

In the $Z/D_{av,j}$ of 2.4, and in the initial rows of 1-3, the flow shows an impingement behavior similar to the flat impinging jet. Interaction with the target wall in tight spacing between the jet and the wall, jet interacts with pimple-dimples and loses some of its momenta. The behavior is also seen in the heat transfer results where the initial rows for this case feature the lowest heat transfer possible. Due to this tight spacing ratio, the jet still holds it is potential core at rows 7-9. Little to no change is seen when comparing to rows 1-3 here as the effect of crossflow is still premature. The mean velocity starts picking up the speed around the region between rows 9 and 13. Recirculation zones within the dimples and interactions around the pimples, in addition to the creation of vortical structures, promote turbulence in region 13-15. The maximum heat transfer enhancement, velocity, and turbulence generation are seen in regions 18-20.

As discussed earlier, based on the row-by-row comparison, the greater difference between the cases in the impingement region is noticed in the crossflow region. The impingement region behaves similarly for all the cases except for the 2.4, as discussed above. The region of rows 18-20 in the 5,000 case shows a difference in the interaction between the NPR features. As the spacing is tighter in the lower case of 2.87, the velocity magnitude is higher, and crossflow is faster, providing less protection for the jets and more interaction with the target surface.

The effects of the increasing jet bending as given by crossflow and jet interaction with the features start influencing the heat transfer increasingly after the 13th row. Before that, the ratio of Nu/Nu_0 decreases up until the 8-9th row and starts increasing thereafter. Figure 59 and Figure 60 show the streamlines and surface heat flux for $Re_{av,j}$ = 9,000 for $Z/D_{av,j}$ = 2.4 and 2.87. Higher heat flux is seen on the surface in rows 1-3 outside the vicinity of the jet in the 2.87 cases. A little downstream, jet bending starts to occur more dominantly in rows 7-9 since the jets are slower than the 2.4 cases in that region. Locally and globally, heat transfer starts to increase in the 2.4 case due to the stronger forces of vortical structures. The jets in such cases are still somewhat protected by the NPR features, and the interactions produce the highest heat transfer in the region of maximum crossflow velocity in rows 18-20.
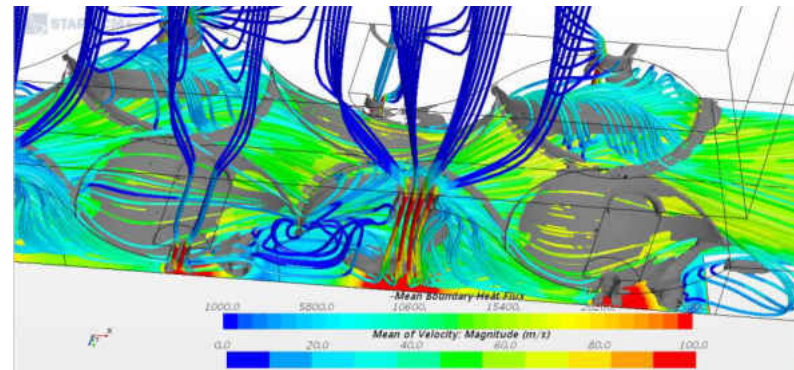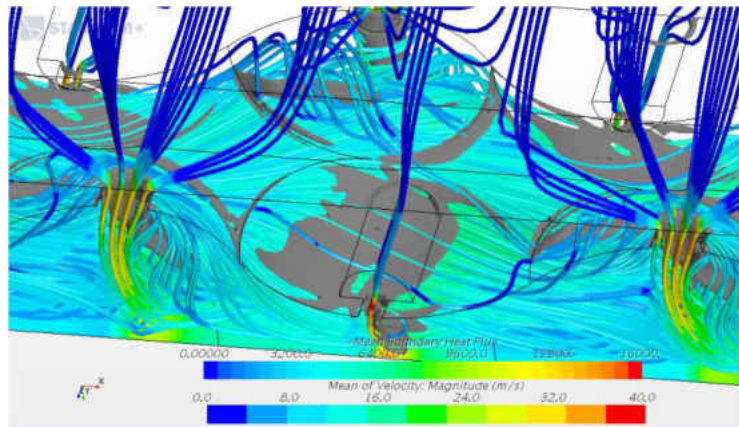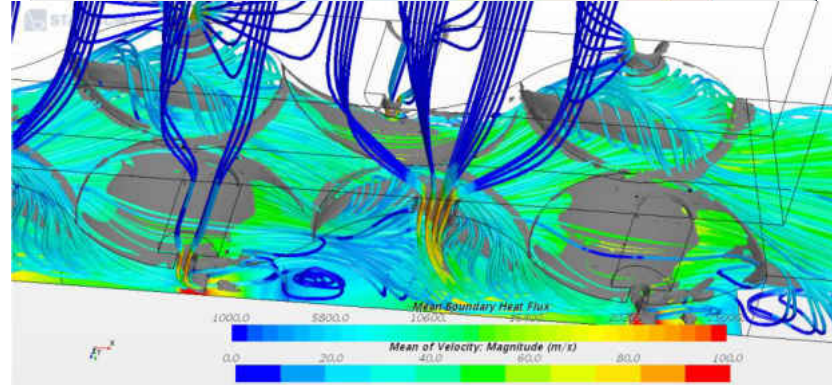
Figure 59: Surface Heat Flux and Streamlines Re$_{av,j}$ = 9,000, Rows 1-3 (left) and 7-9 (right)
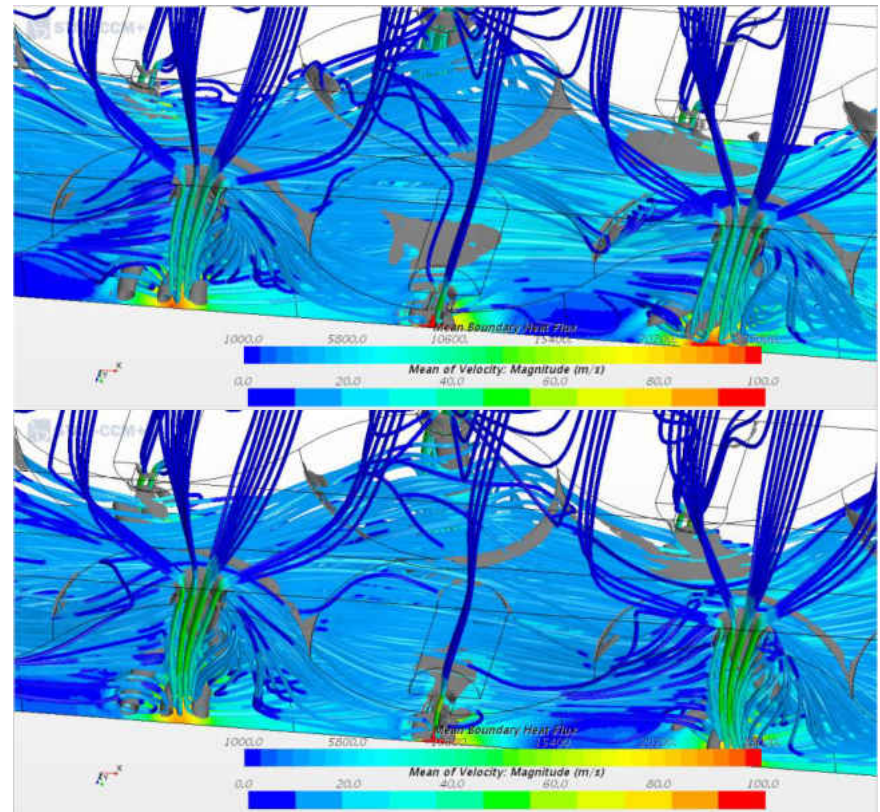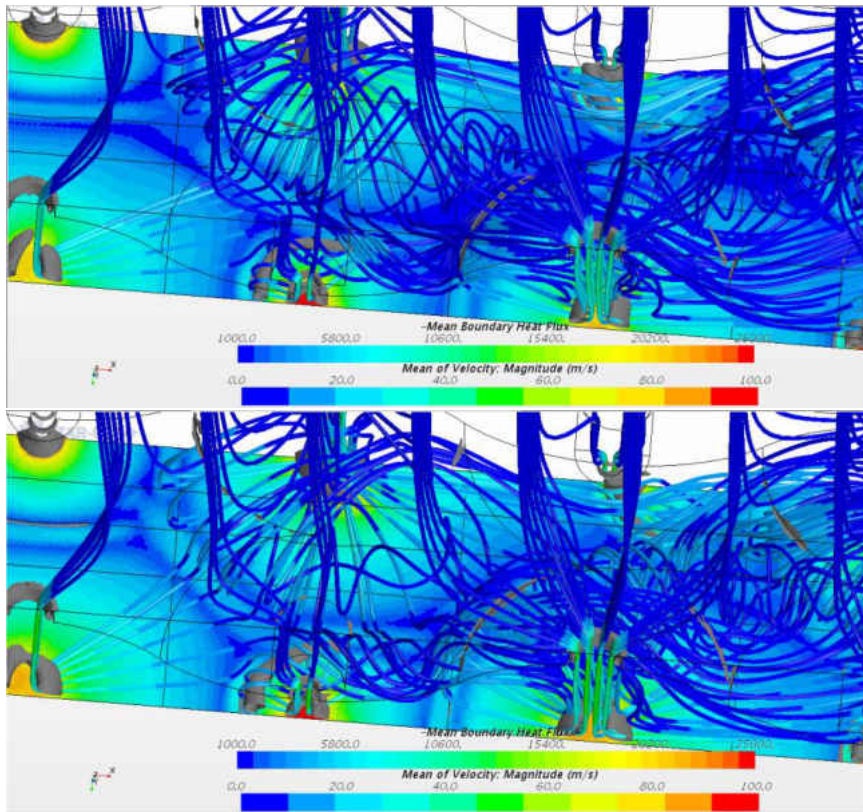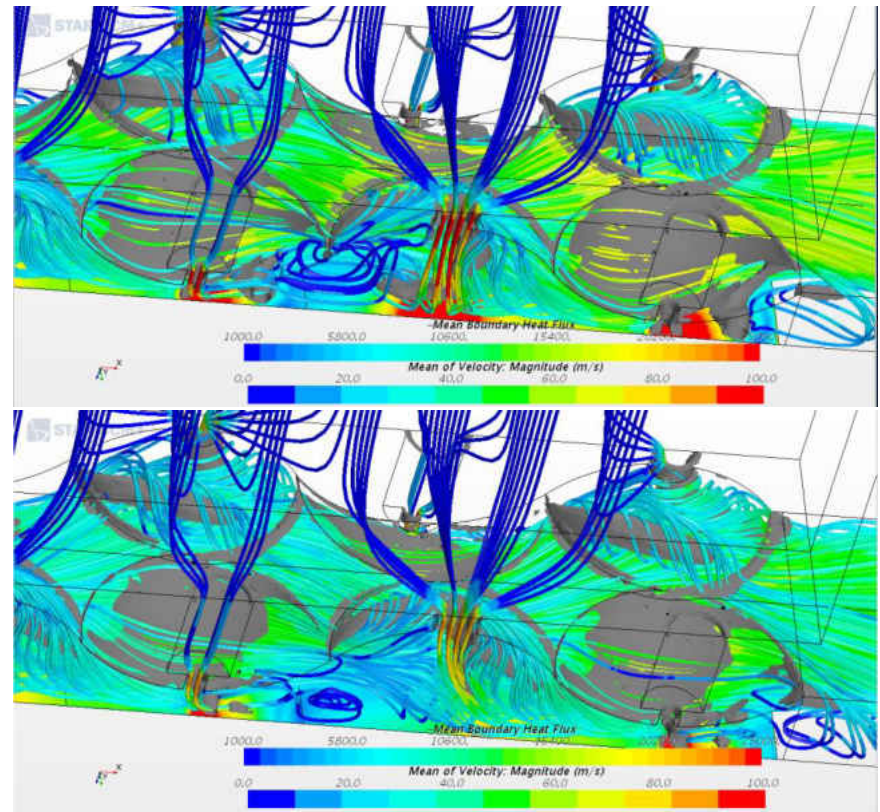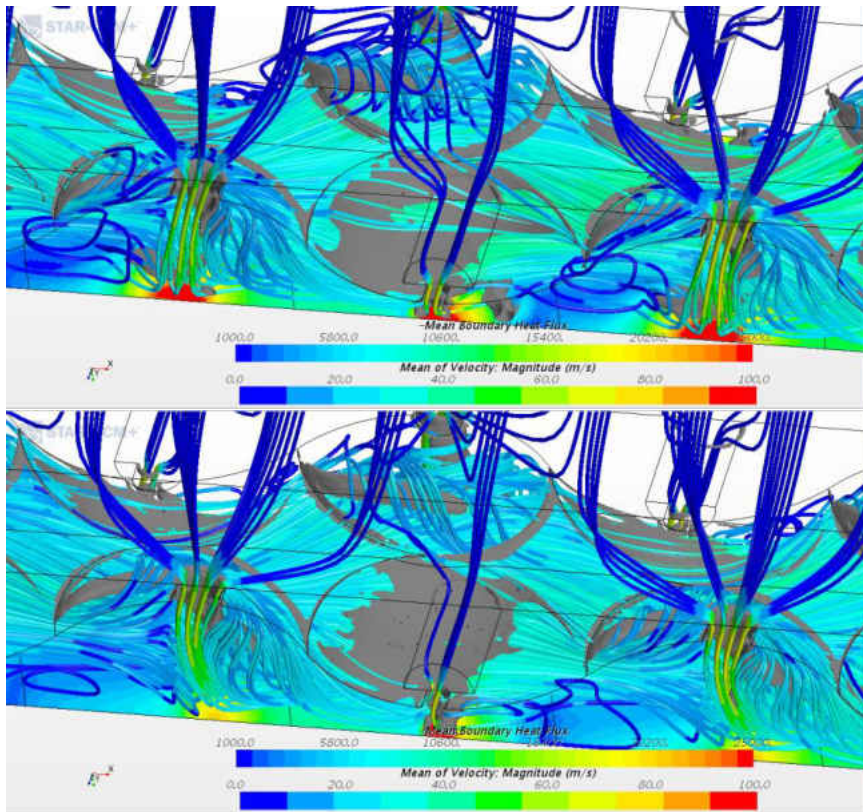
Z/D$_{av,j}$ = 2.4

Z/D$_{av,j}$ = 2.87

Z/D$_{av,j}$ = 2.4

Z/D$_{av,j}$ = 2.87

Figure 60: Surface Heat Flux and Streamlines Re$_{av,j}$ = 9,000, Rows 13-15 (left) and 18-20 (right)

125

Surface Visualization

A qualitative comparison of surface patterns is seen in Figure 61 and Figure 63 for the experimental results for $Z/D_{av,j} = 2.87$ and $Z/D_{av,j} = 4$ with $Re_{av,j} = 7,000$. The target surface is uniformly painted with an oil-florescent pigment mixture, and the test is run until the paint pattern reaches a steady state.

Once the paint dries, a picture of the surface is taken and then processed for analysis. Figure 62 and Figure 64 show the numerical simulation results for the same cases with the heat flux contours overlayed with surface streamlines of the wall shear stress vector. The numerical simulation results show heat flux contours over-layed with surface streamlines of the wall shear stress vector. Accumulation of paint in the experiment corresponds to recirculation/low wall shear stress (lower heat transfer) zones, and locations of thin paint are associated with higher velocity/high wall shear stress (high heat transfer) zones. It can be noticed that for the second half of the rows, jets bends slightly, which results in a more significant gap between jet impingement location, and their downstream recirculation zones. This is also an agreement with the discussion presented in Comparison with Pimple-Dimpled Jet Plate on Page 103 from Overall, that the zones can be defined into two: Impingement and crossflow. Comparing both Figure 61 and Figure 63, the interaction between jet-to-jet as well as secondary structure from

the dimples deteriorates at higher $(Z/D_{av,j})$. The strength of the jet impingement and vortical structures formed are decreased as a result of increasing $(Z/D_{av,j})$. As a result of jet-to-jet interaction, jet bending is more evident in the higher $(Z/D_{av,j})$ case. Due to a weakened impingement, heat transfer is lower in the downstream sections, and lower crossflow jet velocity causes the detriment in the downstream row.
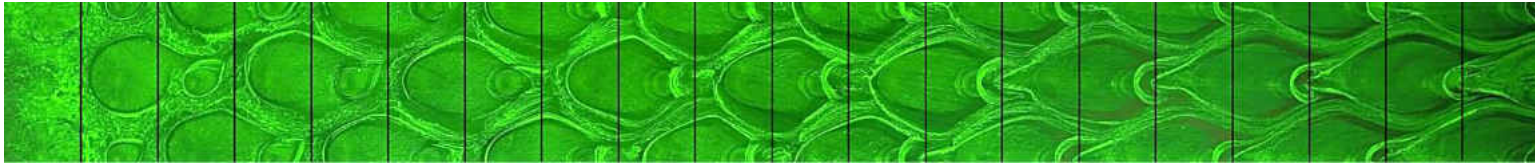
Figure 61: Surface Flow Visualization for $Re_{av,j}$ = 7,000, $Z/D_{av,j}$ = 2.87
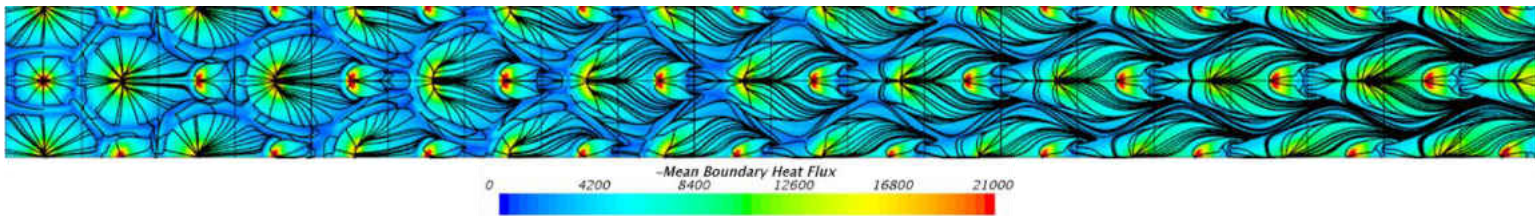
Figure 62: Numerical Heat Flux Contours for $Re_{av,j}$ = 7,000, $Z/D_{av,j}$ = 2.87
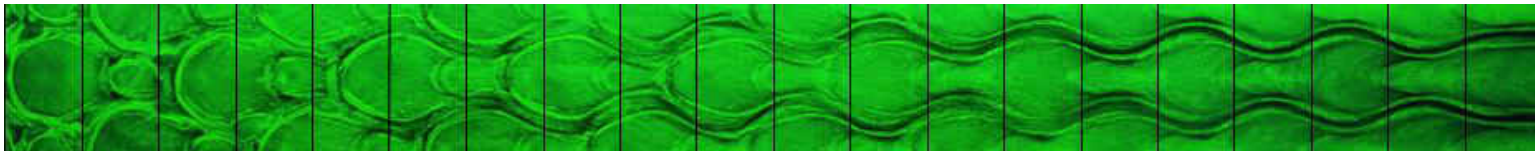
Figure 63: Surface Flow Visualization for $Re_{av,j}$ = 7,000, $Z/D_{av,j}$ = 4
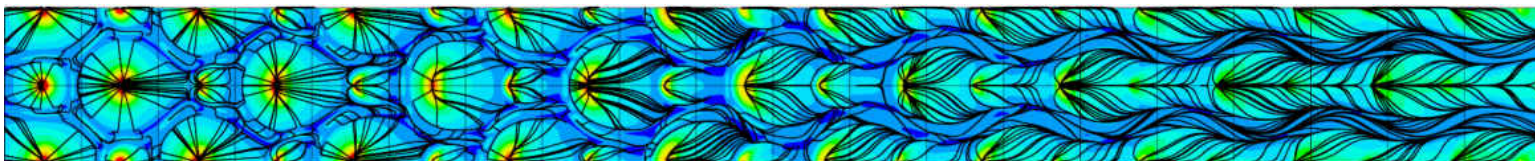
Figure 64: Numerical Heat Flux Contours for $Re_{av,j}$ = 7,000, $Z/D_{av,j}$ = 4

CHAPTER 9:   CORRELATIONS

The methodology of least squares of a regression line is utilized for the logarithmic multivariable problem. The Analysis of Variance (ANOVA) tables are presented for the flat plate and the novel NPR plate. The statistical hypothesis assumes that both variables ($Re_{av,j}$) and ($Z/D_{av,j}$) are evident and contribute in determining the ultimate value of Nusselt number.

Flat Plate

The results of 15 observations regression analysis are shown below in Table 6, Table 7, and Table 8. The coefficient of determination (R^2) value in Table 6 indicates that 97.72% of the variation in log (Nu) is being captured by the multiple regression to log (Re) and log ($Z/D_{av,j}$). Due to the use of multiple variables, the adjusted R^2 is used. The standard error reported is an approximated standard deviation of the distribution in the least-squares estimate.

Table 6: Regression Statistics of Flat Plate

R Square	0.98049
Adjusted R Square	0.97724
Standard Error	0.01318
Observations	15

Table 7: Analysis of Variable for Flat Plate

	df	SS	MS	F	Significance F
Regression	2	0.10479	0.05240	301.55929	5.51232E-11
Residual	12	0.00209	0.00017		
Total	14	0.10688			

Table 8 shows that all two-sided P-values for both variables are very small, indicating that the coefficients are not zero.

Table 8: Summary of Least Squares Fit to log(Nu$_{av,global}$) on Log(Re$_{av,j}$)

and log(Z/D$_{av,j}$) - Flat

	Coefficients	Standard Error	t Stat	P-value
Intercept	-1.59118	0.12552	-12.67670	2.61827E-08
Re	0.77569	0.03254	23.83471	1.7836E-11
Z/D$_{av,j}$	-0.14733	0.02489	-5.91822	7.05122E-05

Using the information above from the tables, the Nusselt number for the flat plate can be found by anti-logging the Equation from Chapter 6. The Nusselt number is then given by:

$$Nu_{av,global,flat} = 0.0256 \cdot Re_{av,j}^{0.776} \cdot \left(\frac{Z}{D_{av,j}}\right)^{-0.147} \tag{9-1}$$

130

It is now appropriate to replot Figure 37: Comparison of Literature Data with Current Study, and adding the model fitted in this section in Figure 65: Comparison of This Study with Others (Model and Experimental)
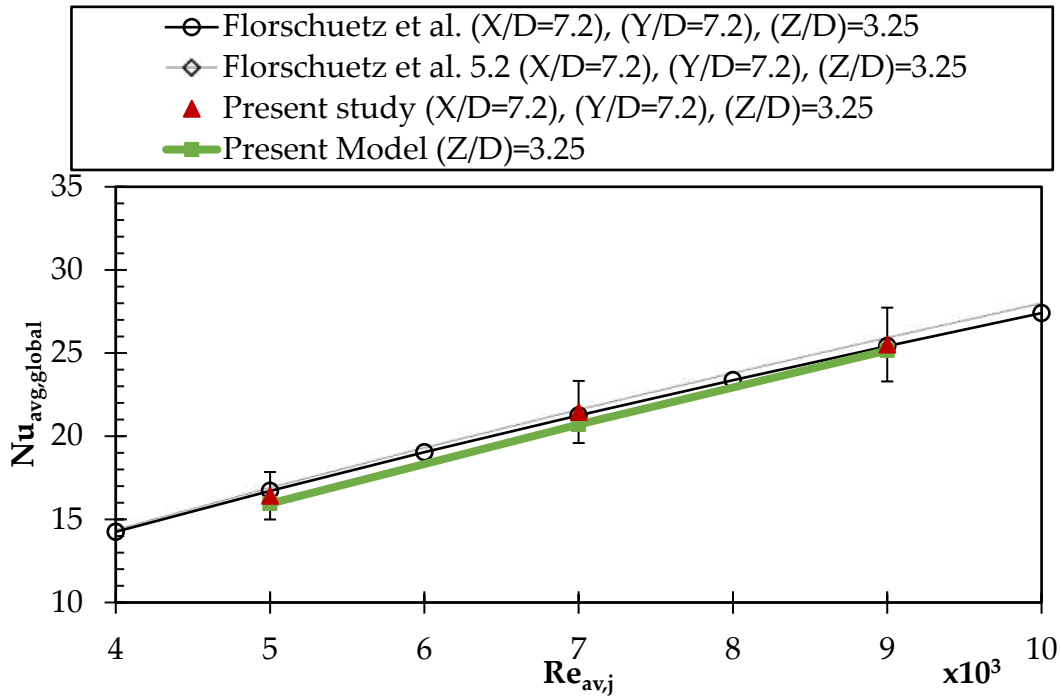
Figure 65: Comparison of This Study with Others (Model and Experimental)

From the above figure, the fitted model shows a good prediction of both data from literature and the experimental data. This model is found to be at a maximum of 3.8% off from the experimental data.

Pimple-Dimple Plate

Table 9 shows summary statistics for the NPR plate regression analysis. Similar results and accuracy of the regression model from the flat plate, with a great accuracy of 97.92% model fitness, and a standard deviation of 0.013.

Table 9: Regression Statistics of NPR Plate

R Square	0.98221
Adjusted R Square	0.97924
Standard Error	0.01304
Observations	15

Table 10 shows small values for the sum of squares and the mean sum of squares for the residuals to be low, and the F-value to be high, indicating a robust model.

Table 10: Analysis of Variable for NPR Plate

	df	*SS*	*MS*	*F*	*Significance F*
Regression	2	0.11266	0.05633	331.19023	3.17E-11
Residual	12	0.00204	0.00017		
Total	14	0.11470			

Even though Table 11 shows P-values of < 0.0001, it is a good indicator from the comparison that the Nusselt number is dependent on the Reynolds number on a larger degree than on the $Z/D_{av,j}$. This is acceptable since not only intuition agrees with such

statement, but also because the increase in Reynolds number for example contributes to

a higher jet velocities and increase in jet momentum. Thus, an increase in Nusselt number

would be expected.

Table 11: Summary of Least Squares Fit to log(Nu$_{av,global}$) on Log(Re$_{av,j}$)

and log(Z/D$_{av,j}$) - NPR

	Coefficients	Standard Error	t Stat	P-value
Intercept	-1.70132	0.12419	-13.69953	1.09E-08
Re	0.80523	0.03220	25.00769	1.01E-11
Z/D$_{av,j}$	-0.14981	0.02463	-6.08241	5.48E-05

Using the information above from the tables, the Nusselt number for the NPR plate

can be found by anti-logging. The Nusselt number is then given by:

$$Nu_{av,global,NPR} = 0.0199 \cdot Re_{av,j}^{0.805} \cdot \left(\frac{Z}{D_j}\right)^{-0.15} \tag{9-2}$$

It is again proper to plot the experimental data obtained for NPR and the model.

Figure 66: Comparison of Experimental and Model for NPR shows two plotted entities:

the model and the experimental data. The deviation in the results is close to 2%.

With the R^2 values reported for these two plates, both of the models are of excellent approximation to the data. Even though some models in the literature account for Prandtl number, it is assumed constant here and combined with the constant.
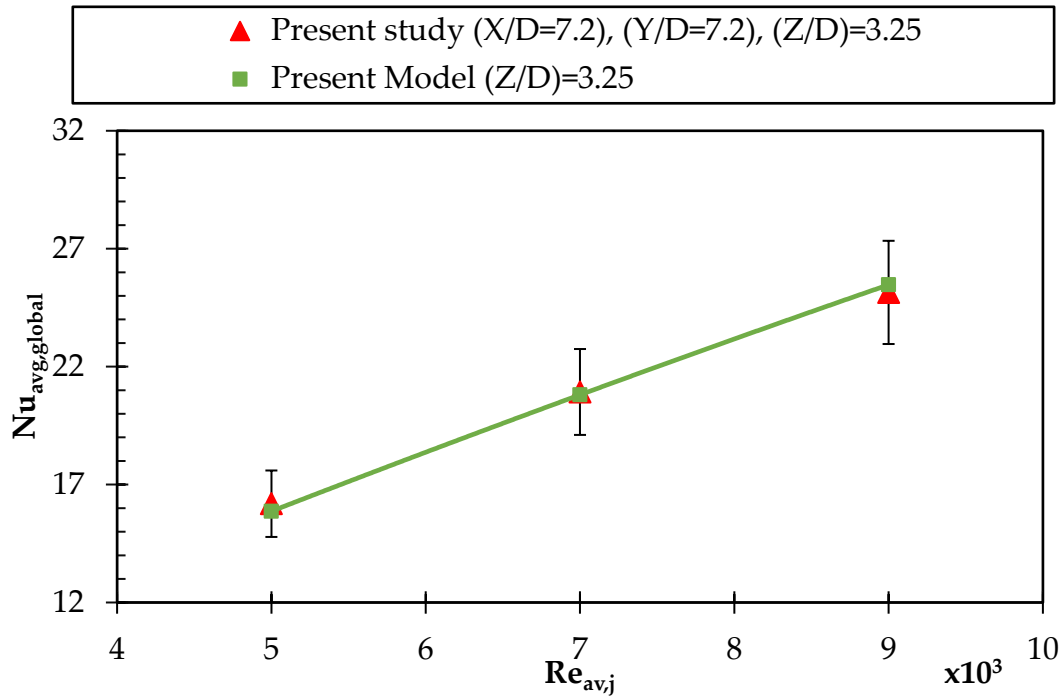
Figure 66: Comparison of Experimental and Model for NPR

CHAPTER 10: CONCLUSION AND FUTURE WORK

The evaluation of global-averaged heat transfer measurements are presented, and compared for two jet plate configurations; flat and pimpled-dimpled. Staggered arrays of jets with equal jet-to-jet spacing along the span and stream-wise directions are considered. The effect of Reynolds number and jet-to-impingement wall surface are studied. Correlations for both plates were developed for the overall heat transfer, non-dimensionalized by the quantity, Nusselt number.

Conclusions

Combining the effects of impingement crossflow and pimple-dimple appears to help the heat transfer in the downstream regions. Crossflow helped in detaching the boundary layer and provide for a more effective cooling. The following findings can be concluded from this study:

1. There is no evident enhancement, nor detriment in local-averaged or global averaged heat transfer within the first 10 rows at various $Z/D_{av,j}$ when comparing a flat to a pimple-dimpled orifice plate.

2. The increase of $Z/D_{av,j}$ results in lower overall surface heat transfer due to weakened impingement heat transfer in upstream rows, and lower crossflow velocities in downstream rows. These effects are seen for both plate configurations.

3. The Pimple-dimpled orifice plate showed higher heat transfer in downstream rows when compared to the flat orifice plate.

4. Heat transfer enhancement of the pimple-dimpled plate, over the flat orifice plate, is attributed to the formation of secondary vortical structures that are formed as the crossflow interacts with the pimple-dimple features. These structures are seen to interact with the issuing jets, as well as the target wall. The resulting interactions are seen to enhance mixing in the downstream regions.

5. The combination of pimples and dimples, is thought to have a positive impact on heat transfer. However, due to the geometric constraints of this study and the inflexibility of the NPR plate's geometrical dimensions, it was not evident that an enhancement is present.

6. At some cases, nearly 23% enhancement is seen in the crossflow region of the NPR plate compared to the baseline, giving confidence that an enhancement in the

impingement region could also be feasible, as discussed in the last section, Future

Work.

7. Parametric effect of varying the jet-to-wall spacing ratio ($Z/D_{av,j}$) and the jet-averaged Reynolds number ($Re_{av,j}$) were investigated. Increasing the Reynolds number increases the momentum of the jets providing higher heat transfer. Increasing the spacing ratio results in higher heat transfer in early regions, but higher in the crossflow regions. Such behavior is more visible in the pimple-dimple plate and suggests that pimples and dimples create stronger vorticies with the aid of crossflow.

8. Correlations from the experimental results of heat transfer of the baseline and novel impingement plates were developed in a non-dimensionalized form:

   a. For flat plate,

$$Nu_{av,global,flat} = 0.0256 \cdot Re_{av,j}^{0.776} \cdot \left(\frac{Z}{D_{av,j}}\right)^{-0.147}, R^2 = 0.9772$$

   b. For pimple-dimple plate,

$$\mathrm{Nu_{av,global,NPR}}= 0.0199 \cdot \mathrm{Re_{av,j}}^{0.805} \cdot \left(\frac{Z}{\mathrm{D_{av,j}}}\right)^{-0.15}, R^2 = 0.9792$$

Future Work

While the majority of studies shown earlier proposed an overall enhancement in heat transfer, this study is constrained to a single geometrical plate parameter. The configuration herein is meant to provide for an additional structural rigidity while still providing for an enhancement of cooling. In the light of such study, the following is recommended:

- An exploration of a full optimization study incorporating the following exploration variables:

    - $D_{j,dimple}$, $D_{j,pimple}$ t/D_{pimple} ratio, t/D_{dimple} ratio

    - Variation of X_n, Y_n

    - Combined structural + heat transfer study

This recommendation will result in an impingement configuration that will result in an overall enhancement in heat transfer as the objective function should be to maximize the heat transfer coefficient.

APPENDIX A: PUBLICATIONS

1. <u>Zawati, H.</u>, Gupta, G., Khlyapov, Y., Fernandez, E., Kapat, J., Schaenzer, M., Rodriguez, J., 2020, "Multi-Jet Impingement Heat Transfer with a Dimple-Pimple Patterned Jet Plate," ***Proceedings of the ASME Turbomachinery Technical Conference and Exposition***, London, England, June 22-26, 2020, American Society of Mechanical Engineers Digital Collection. Paper No. GT2020-16102, pp. xx-xx. **Accepted Paper**

2. Torres, J., <u>Zawati, H.</u>, Fernandez, E., Kapat, J., 2020, "Experimental and Numerical Study of Array Jet Impingement Cooling on a Leading-Edge Curved Surface," ***Proceedings of the ASME Turbomachinery Technical Conference and Exposition***, London, England, June 22-26, 2020, American Society of Mechanical Engineers Digital Collection. Paper No. GT2020-14810, pp. xx-xx. **Accepted Paper**

3. Osorio, A., Hodges, J., <u>Zawati, H.</u>, Fernandez, E., Kapat, J., Rodriguez, J., 2019, "Impact of Sweeping Jet on Area-Averaged Impingement Heat Transfer," ***Proceedings of the ASME Turbomachinery Technical Conference and Exposition***, Phoenix, Arizona, USA, June 17-21, 2019, American Society of Mechanical Engineers Digital Collection. Paper No. GT2019-91897, pp. V05AT13A014. https://doi.org/10.1115/GT2019-91897

4. <u>Zawati, H.</u>, Elmore, M., Nagaiah N., Kapat, J., 2018, "Thermal Analysis and Pressure Loss Modeling for an Optimized Heat Exchanger Used in a Recuperated CO2 Power Cycle," ***Proceedings of the ASME Turbomachinery Technical Conference and Exposition***, Oslo, Norway, June 11-15, 2018, American Society of Mechanical Engineers Digital Collection. Paper No. GT2018-76975, pp. V009T38A021. https://doi.org/10.1115/GT2018-76975.

5. Hodges J., Blanchette, L., <u>Zawati, H.</u>, Fernandez, E., Rodriguez, J., Kapat, J., 2016, "An Experimental Investigation of the Flow Field and Heat Transfer from a Single Impinging Jet with Varying Confinement Conditions," ***Proceedings of the 52nd AIAA/SAE/ASEE Joint Propulsion Conference***, Salt Lake City, Utah, USA, July 25-27, 2016, American Institute for Aeronautics and Astronautics. Paper No. AIAA 2016-5048, pp. xx. https://doi.org/10.2514/6.2016-5048.

6. Mohagheghi, M., <u>Zawati, H.</u>, Pinol, T., Gou, J., Xu, C., Kapat, J., 2016, "Use of 1-D Finite Enthalpy Method for a High-Temperature Recuperator Made of Polymer

Derived Ceramic Composite for a Supercritical Carbon Dioxide Power System," *The 5th International Symposium–Supercritical CO2 Power Cycles,* San Antonio, Texas, USA, March 28-31, 2016, Paper No. 134. http://sco2symposium.com/papers2016/HeatExchanger/134paper.pdf

APPENDIX B: COPYRIGHT PERMISSIONS

Siemens AG

Husam Zawati

From: presspictures.cc@siemens.com
Sent: Thursday, April 9, 2020 11:50 AM
To: Husam Zawati
Cc: presspictures.cc@siemens.com
Subject: AW: Request for permission to use

Dear Husam,
you can use both pictures for your doctoral dissertation.
Pictures must bear the copyright: Siemens AG

Feel free to contact us if you have any further questions on this matter.

Best regards,
Kirsten Sepperl

External service provider at Siemens AG
Siemens Photography and Multimedia department
mailto:presspictures.cc@siemens.com

SIEMENS
Ingenuity for life

Siemens Aktiengesellschaft: Vorsitzender des Aufsichtsrats: Jim Hagemann Snabe; Vorstand: Joe Kaeser, Vorsitzender; Roland Busch, Lisa Davis, Klaus Helmrich, Janina Kugel, Cedrik Neike, Ralf P. Thomas; Sitz der Gesellschaft: Berlin und München, Deutschland; Registergericht: Berlin Charlottenburg, HRB 12300, München, HRB 6684; WEEE-Reg.-Nr. DE 23691322

To help us answer your questions quickly and to your satisfaction, always include all correspondence in your e-mails.

Von: Husam Zawati <hzawati@knights.ucf.edu>
Gesendet: Donnerstag, 9. April 2020 17:44
An: CG Press Pictures <presspictures.cc@siemens.com>
Betreff: RE: Request for permission to use

Hi Kirsten,
Thank you for the reply. Please see below

https://press.assets.siemens.com/content/siemens/press/ui/en/search.html#/asset/sid:16c41157-3f4a-4590-b5a1-a858c69ad9f2
SGT5-4000F model

AND

https://press.assets.siemens.com/content/siemens/press/ui/en/search.html#/asset/sid:a641d51e-0428-4d4b-87b5-e261e253c5c9
SGT 700.

Thank you,
Husam Zawati

From: presspictures.cc@siemens.com [mailto:presspictures.cc@siemens.com]
Sent: Thursday, April 9, 2020 9:55 AM
To: Husam Zawati <hzawati@knights.ucf.edu>

1

143

Cc: presspictures.cc@siemens.com
Subject: Request for permission to use

Dear Husam Zawati,

Thank you very much for your request and your interest in Siemens Press Pictures.
Could you please explain in more detail which pictures exactly you are interested in. Please send us the URL or ID and we will check your request.

Feel free to contact us if you have any further questions on this matter.

Best regards,
Kirsten Sepperl

External service provider at Siemens AG
Siemens Photography and Multimedia department
mailto:presspictures.cc@siemens.com

SIEMENS
Ingenuity for life

To help us answer your questions quickly and to your satisfaction, always include all correspondence in your e-mails.

Von: Husam Zawati <hzawati@knights.ucf.edu>
Gesendet: Mittwoch, 8. April 2020 18:43
An: CG Press Pictures <presspictures.cc@siemens.com>
Betreff: Request for permission to use

Dear Sir/Madam,

I am completing the writing of my doctoral dissertation titled: "Heat Transfer and Correlations of Jet Array Impingement with a Hemispherical-Dimpled Plate" at the University of Central Florida.

I would like your permission to reprint in my dissertation, some of the images of gas turbine engines available to download from:
https://press.assets.siemens.com/content/siemens/press/ui/en/search.html#/

In the caption, I would include the Company, model, and the proper citation.

Thank you for the consideration,

Husam Zawati
Graduate Research Assistant and Project Lead
Center for Advanced Turbomachinery & Energy Research (CATER)
Laboratory for Turbine Aerodynamics, Heat Transfer & Durability
Laboratory for Cycle Innovation & Optimization
Lab: (407) 823-6072 | Cell: (407) 408-3885

2

Capstone Turbine Corporation

PHOTOGRAPH RELEASE AGREEMENT

This PHOTOGRAPH RELEASE AGREEMENT is made and entered into as of this 8th day of April, 2020, by and between Capstone Turbine Corporation, a Delaware corporation ("Capstone") and Husam Zawati, an individual (the "Author").

Capstone, to the best of its knowledge, is the owner of a certain photograph attached hereto at Exhibit A (the "Photograph"). The Author is preparing to publish a dissertation tentatively entitled HEAT TRANSFER AND CORRELATIONS OF JET ARRAY IMPINGEMENT WITH A HEMISPHERICAL-DIMPLED PLATE (the "Dissertation"). Author desires to include the Photograph within the Dissertation, and Capstone hereby grants the Author a world-wide, royalty-free license to use the Photograph in the Dissertation, including all future editions thereto, in any and all formats in which the Dissertation appears.

Author shall indemnify, defend and hold harmless Capstone and its officers, directors, and agents from any third party claim that may arise from the Author's use of the Photograph. Because the Photograph is being used free of charge, the Photograph is provided to the Author "as is" without warranty of any kind, either expressed or implied, including, but not limited to, the implied warranties of merchantability, non-infringement and fitness for a particular purpose.

Capstone grants to the Author a non-exclusive license to use Capstone's name for the sole purpose of providing appropriate attribution as to the source the Photograph in the Dissertation. Whenever the Photograph is displayed, Author shall ensure that the Photograph is accompanied by the following attribution:

Courtesy: Capstone Turbine Corporation

IN WITNESS WHEREOF, the parties hereto have caused this Agreement to be executed as of the date written above.

AUTHOR: CAPSTONE TURBINE CORPORATION:

Husam Zawati   By: _____

Husam Zawati   Maria Silva
(Printed Name)   Marketing & Media Relations Manager
                                       (Printed Name)

APPENDIX C: SELECTED IMAGES FROM EXPERIMENTAL SETUP
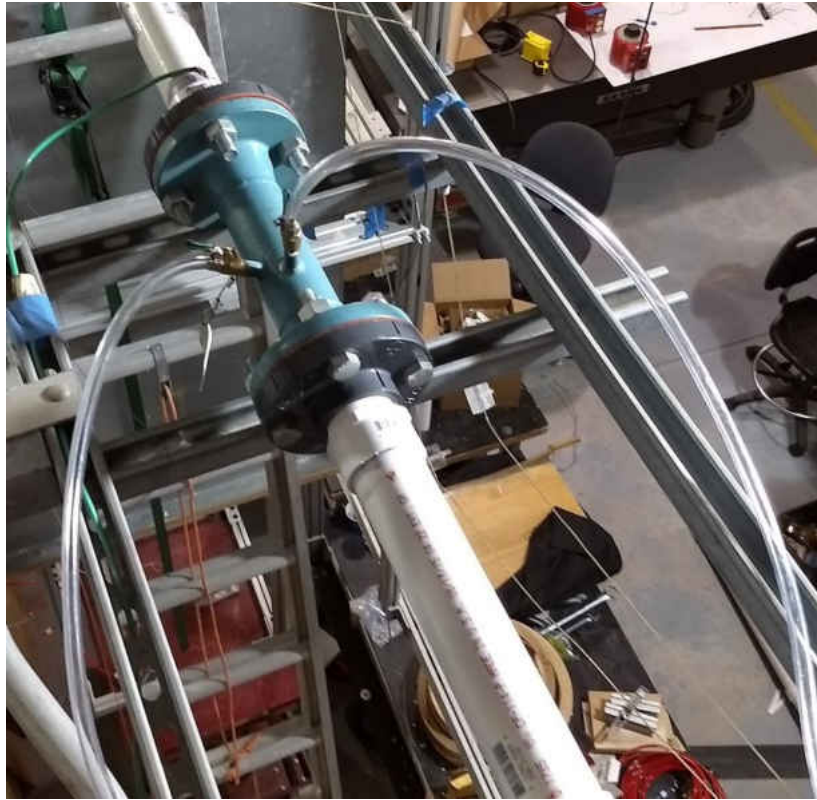
Figure 67: Experimental Plenum and Venturi

Figure 68: The 2″ Venturi Used in Current Study

LIST OF REFERENCES

[1] 2020, "Annual Energy Outlook 2020, Table A9," Energy Information Administration, Washington D.C.

[2] Clement, D., Lehman, M., Hamrin, J., and Wiser, R., 2005, "International Tax Incentives for Renewable Energy: Lessons for Public Policy," Center for Resource Solutions, San Francisco, California, USA.

[3] Cansino, J. M., Pablo-Romero, M. d. P., Román, R., and Yñiguez, R., 2010, "Tax incentives to promote green electricity: An overview of EU-27 countries," Journal of Energy Policy, 38(10), pp. 6000-6008.

[4] Zuluaga, M. M., and Dyner, I. J. J. o. c. P., 2007, "Incentives for renewable energy in reformed Latin-American electricity markets: the Colombian case," 15(2), pp. 153-162.

[5] Şöhret, Y., Ekici, S., Altuntaş, Ö., Hepbasli, A., and Karakoç, T. H., 2016, "Exergy as a useful tool for the performance assessment of aircraft gas turbine engines: a key review," Progress in Aerospace Sciences, 83, pp. 57-69.

[6] MacIsaac, B., and Langton, R., 2011, Gas turbine propulsion systems, John Wiley & Sons.

[7] Langston, L. S., 2011, "Powering Ahead," Mechanical Engineering, 133(05), pp. 30-33.

[8] 2011, Annual energy review, Government Printing Office US Energy Information Administration.

[9] Fosheim, J., Gagne, A., Johnson, P., and Thomas, B., 2014, "Enhancing the undergraduate educational experience: development of a micro-gas turbine laboratory," International Journal of Mechanical Engineering Education, 42(3), pp. 267-278.

[10] Kover, A., 2018, "GE Turbine Delivers Second World Record," https://www.ge.com/reports/whoops-ge-turbine-delivers-second-world-record/.

[11] Gülen, S. C., 2019, Gas Turbines for Electric Power Generation, Cambridge University Press.

[12] Boyce, M. P., 2011, Gas turbine engineering handbook, Elsevier.

[13] Boles, M., and Cengel, Y., 2014, "An Engineering Approach," New York: McGraw-Hil l Education.

[14] Han, J.-C., 2018, "Advanced Cooling in Gas Turbines 2016 Max Jakob Memorial Award Paper," Journal of Heat Transfer, 140(11).

[15] Han, J.-C., Dutta, S., and Ekkad, S., 2012, Gas turbine heat transfer and cooling technology, CRC press.

[16] Otto, M., 2019, "Improving Turbine Performance: A Contribution to the Understanding of Heat Transfer and Vortical Structures in Staggered Pin Fin Arrays."

[17] Sharma, A., Dudykevych, T., Sansom, D., and Subramanian, R., 2017, "Increased reliability of gas turbine components by robust coatings manufacturing," Journal of Thermal Spray Technology, 26(6), pp. 1084-1094.

[18] Arai, M., and Suidzu, T., 2013, "Porous ceramic coating for transpiration cooling of gas turbine blade," Journal of Thermal Spray Technology, 22(5), pp. 690-698.

[19] Naik, S., 2017, "Basic Aspects of Gas Turbine Heat Transfer," Heat Exchangers–Design, Experiment and Simulation, pp. 111-142.

[20] Clarke, D. R., Oechsner, M., and Padture, N. P., 2012, "Thermal-barrier coatings for more efficient gas-turbine engines," MRS Bulletin, 37(10), pp. 891-898.

[21] Son, C., Gillespie, D., Ireland, P., and Dailey, G. M., "Heat transfer and flow characteristics of an engine representative impingement cooling system," Proc. ASME Turbo Expo 2000: Power for Land, Sea, and Air, American Society of Mechanical Engineers, pp. V003T001A027-V003T001A027.

[22] Han, B., and Goldstein, R., 2001, "Jet‑impingement heat transfer in gas turbine systems," Annals of the New York Academy of Sciences, 934(1), pp. 147-161.

[23] Livingood, J. N., and Hrycak, P., 1973, "Impingement heat transfer from turbulent air jets to flat plates: a literature survey."

[24] Florschuetz, L., and Isoda, Y., "Flow distributions and discharge coefficient effects for jet array impingement with initial crossflow," Proc. ASME 1982 International Gas Turbine Conference and Exhibit, American Society of Mechanical Engineers, pp. V004T009A013-V004T009A013.

[25] Florschuetz, L., Metzger, D., and Su, C., "Heat transfer characteristics for jet array impingement with initial crossflow," Proc. ASME 1983 International Gas Turbine Conference and Exhibit, American Society of Mechanical Engineers, pp. V004T009A001-V004T009A001.

[26] Florschuetz, L., and Su, C., 1987, "Effects of crossflow temperature on heat transfer within an array of impinging jets," Journal of Heat Transfer, 109(1), pp. 74-82.

[27] Florschuetz, L., Truman, C., and Metzger, D., "Streamwise flow and heat transfer distributions for jet array impingement with crossflow," Proc. ASME 1981 International Gas Turbine Conference and Products Show, American Society of Mechanical Engineers, pp. V003T009A005-V003T009A005.

[28] Metzger, D., Florschuetz, L., Takeuchi, D., Behee, R., and Berry, R., 1979, "Heat transfer characteristics for inline and staggered arrays of circular jets with crossflow of spent air," Journal of Heat Transfer, 101(3), pp. 526-531.

[29] Amano, R. S., and Sundén, B., 2014, Impingement jet cooling in gas turbines, WIT Press.

[30] Goldstein, R. J., Sobolik, K., and Seol, W., 1990, "Effect of entrainment on the heat transfer to a heated circular air jet impinging on a flat surface."

[31] Han, B., and Goldstein, R. J., 2001, "Jet‑impingement heat transfer in gas turbine systems," Annals of the New York Academy of Sciences, 934(1), pp. 147-161.

[32] Hodges, J. D., Blanchette, L., Zawati, H., Fernandez, E., Rodriguez, J., and Kapat, J. S., "An experimental investigation of the flow field and heat transfer from a single impinging jet with varying confinement conditions," Proc. 52nd AIAA/SAE/ASEE Joint Propulsion Conference, p. 5048.

[33] El-Sheikh, H. A., and Gurimella, S., 2000, "Enhancement of air jet impingement heat transfer using pin-fin heat sinks," IEEE Transactions on Components and Packaging Technologies, 23(2), pp. 300-308.

[34] Tan, L., Zhang, J.-Z., and Xu, H.-S., 2014, "Jet impingement on a rib-roughened wall inside semi-confined channel," International Journal of Thermal Sciences, 86, pp. 210-218.

[35] Beitelmal, A. H., Saad, M. A., and Patel, C. D., 2000, "Effects of surface roughness on the average heat transfer of an impinging air jet," International Communications in Heat and Mass Transfer, 27(1), pp. 1-12.

[36] Osorio, A., Hodges, J., Zawati, H., Fernandez, E., Kapat, J. S., and Rodriguez, J., "Impact of Sweeping Jet on Area-averaged Impingement Heat Transfer," Proc. ASME Turbo Expo 2019: Turbomachinery Technical Conference and Exposition, American Society of Mechanical Engineers.

[37] Chyu, M., Yu, Y., Ding, H., Downs, J., and Soechting, F., "Concavity enhanced heat transfer in an internal cooling passage," Proc. ASME International Gas Turbine and Aeroengine Congress and Exhibition, Citeseer, pp. V003T009A080-V003T009A080.

[38] Weigand, B., and Spring, S., 2011, "Multiple jet impingement– a review," Journal of Heat Transfer Research, 42(2).

[39] Andrews, G., Hussain, R. A., and Mkpadi, M., 2006, "Enhanced impingement heat transfer: the influence of impingement X/D for interrupted rib obstacles (rectangular pin fins)."

[40] Katti, V., and Prabhu, S., 2009, "Influence of streamwise pitch on the local heat transfer characteristics for in-line arrays of circular jets with crossflow of spent air in one direction," Heat and mass transfer, 45(9), pp. 1167-1184.

[41] Hollworth, B., and Berry, R. D., 1978, "Heat transfer from arrays of impinging jets with large jet-to-jet spacing."

[42] Geers, L. F., Hanjalić, K., and Tummers, M., 2006, "Wall imprint of turbulent structures and heat transfer in multiple impinging jet arrays," Journal of Fluid Mechanics, 546, pp. 255-284.

[43] Park, J., Goodro, M., Ligrani, P., Fox, M., and Moon, H.-K., 2007, "Separate effects of Mach number and Reynolds number on jet array impingement heat transfer."

[44] Yong, S., Jing-zhou, Z., and Gong-nan, X., 2015, "Convective heat transfer for multiple rows of impinging air jets with small jet-to-jet spacing in a semi-confined channel," International Journal of Heat and Mass Transfer, 86, pp. 832-842.

[45] Florschuetz, L. W., Berry, R., and Metzger, D., 1980, "Periodic streamwise variations of heat transfer coefficients for inline and staggered arrays of circular jets with crossflow of spent air."

[46] Lee, J., Ren, Z., Ligrani, P., Lee, D. H., Fox, M. D., and Moon, H.-K., 2014, "Cross-flow effects on impingement array heat transfer with varying jet-to-target plate distance and hole spacing," International Journal of Heat and Mass Transfer, 75, pp. 534-544.

[47] Lee, J., Ren, Z., Ligrani, P., Fox, M. D., and Moon, H.-K., 2015, "Crossflows from jet array impingement cooling: Hole spacing, target plate distance, Reynolds number effects," International Journal of Thermal Sciences, 88, pp. 7-18.

[48] Goodro, M., Park, J., Ligrani, P., Fox, M., and Moon, H.-K., "Effect of hole spacing on jet array impingement heat transfer," Proc. ASME Turbo Expo 2007: Power for Land, Sea, and Air, American Society of Mechanical Engineers Digital Collection, pp. 963-976.

[49] Dano, B. P., Liburdy, J. A., and Kanokjaruvijit, K., 2005, "Flow characteristics and heat transfer performances of a semi-confined impinging array of jets: effect of nozzle geometry," International Journal of Heat and Mass Transfer, 48(3-4), pp. 691-701.

[50] Chi, Z., Kan, R., Ren, J., and Jiang, H., 2013, "Experimental and numerical study of the anti-crossflows impingement cooling structure," International Journal of Heat and Mass Transfer, 64, pp. 567-580.

[51] Fechter, S., Terzis, A., Ott, P., Weigand, B., Von Wolfersdorf, J., and Cochet, M., 2013, "Experimental and numerical investigation of narrow impingement cooling channels," International Journal of Heat and Mass Transfer, 67, pp. 1208-1219.

[52] Van Treuren, K. W., Wang, Z., Ireland, P. T., Jones, T. V., and Kohler, S., "Local heat transfer coefficient and adiabatic wall temperature measurement beneath arrays of staggered and inline impinging jets," Proc. ASME 1994 International Gas Turbine and Aeroengine Congress and Exposition, American Society of Mechanical Engineers Digital Collection.

[53] Ricklick, M., Kapat, J., and Heidmann, J., 2010, "Sidewall effects on heat transfer coefficient in a narrow impingement channel," Journal of Thermophysics and Heat Transfer, 24(1), pp. 123-132.

[54] Son, C., Gillespie, D., Ireland, P., and Dailey, G. M., 2001, "Heat transfer and flow characteristics of an engine representative impingement cooling system," J. Turbomach., 123(1), pp. 154-160.

[55] Esposito, E., Ekkad, S., Kim, Y., and Dutta, P., 2009, "Novel jet impingement cooling geometry for combustor liner backside cooling," Journal of thermal science and engineering applications, 1(2).

[56] Kercher, D., and Tabakoff, W., 1970, "Heat transfer by a square array of round air jets impinging perpendicular to a flat surface including the effect of spent air," Journal of Engineering for Power.

[57] Huang, L., and El-Genk, M. S., 1994, "Heat transfer of an impinging jet on a flat surface," International Journal of Heat and Mass Transfer, 37(13), pp. 1915-1923.

[58] Azad, G. S., Huang, Y., and Han, J.-C., 1970, "Jet Impingement Heat Transfere on Pinned Surface Using a Transient Liquid Cristal Technique," International Journal of Rotating Machinery, 8.

[59] Yan, W., Liu, H., Soong, C., and Yang, W.-J., 2005, "Experimental study of impinging heat transfer along rib-roughened walls by using transient liquid crystal technique," International Journal of Heat and Mass Transfer, 48(12), pp. 2420-2428.

[60] Obot, N., and Trabold, T., 1987, "Impingement heat transfer within arrays of circular jets: Part 1—Effects of minimum, intermediate, and complete crossflow for small and large spacings," Journal of Heat Transfer.

[61] Trabold, T., and Obot, N., 1987, "Impingement heat transfer within arrays of circular jets: part II—effects of crossflow in the presence of roughness elements."

[62] Spring, S., Xing, Y., and Weigand, B., 2012, "An experimental and numerical study of heat transfer from arrays of impinging jets with surface ribs," Journal of Heat Transfer, 134(8).

[63] Xing, Y., Spring, S., and Weigand, B., 2010, "Experimental and numerical investigation of heat transfer characteristics of inline and staggered arrays of impinging jets," Journal of Heat Transfer, 132(9).

[64] Xie, Y., Li, P., Lan, J., and Zhang, D., 2013, "Flow and heat transfer characteristics of single jet impinging on dimpled surface," Journal of Heat Transfer, 135(5), p. 052201.

[65] Sriromreun, P., and Sriromreun, P., 2019, "A Numerical and Experimental Investigation of Dimple Effects on Heat Transfer Enhancement with Impinging Jets," Journal of Energies, 12(5), p. 813.

[66] Vinze, R., Khade, A., Kuntikana, P., Ravitej, M., Suresh, B., Kesavan, V., and Prabhu, S., 2019, "Effect of dimple pitch and depth on jet impingement heat transfer over dimpled surface impinged by multiple jets," International Journal of Thermal Sciences, 145, p. 105974.

[67] Xing, Y., and Weigand, B., 2010, "Experimental investigation of impingement heat transfer on a flat and dimpled plate with different crossflow schemes," International Journal of Heat and Mass Transfer, 53(19-20), pp. 3874-3886.

[68] Azad, G. S., Huang, Y., and Han, J.-C., 2000, "Impingement heat transfer on dimpled surfaces using a transient liquid crystal technique," Journal of Thermophysics and Heat Transfer, 14(2), pp. 186-193.

[69] Chang, S. W., Jan, Y. J., and Chang, S. F., 2006, "Heat transfer of impinging jet-array over convex-dimpled surface," International Journal of Heat and Mass Transfer, 49(17-18), pp. 3045-3059.

[70] Chang, S. W., and Liou, H.-F., 2009, "Heat transfer of impinging jet-array onto concave-and convex-dimpled surfaces with effusion," International Journal of Heat and Mass Transfer, 52(19-20), pp. 4484-4499.

[71] Ekkad, S. V., and Kontrovitz, D., 2002, "Jet impingement heat transfer on dimpled target surfaces," International Journal of Heat and Fluid Flow, 23(1), pp. 22-28.

[72] Kanokjaruvijit, K., and Martinez-Botas, R., 2004, "An experimental investigation of the heat transfer due to multiple jets impinging normally on a dimpled surface," Proceedings of the Institution of Mechanical Engineers, Part C: Journal of Mechanical Engineering Science, 218(11), pp. 1337-1347.

[73] Kanokjaruvijit, K., and Martinez-botas, R. F., 2005, "Jet impingement on a dimpled surface with different crossflow schemes," International Journal of Heat and Mass Transfer, 48(1), pp. 161-170.

[74] Kanokjaruvijit, K., and Martinez-Botas, R., 2008, "Heat transfer and pressure investigation of dimple impingement," Journal of Turbomachinery, 130(1), p. 011003.

[75] Kanokjaruvijit, K., and Martinez-Botas, R. F., 2010, "Heat transfer correlations of perpendicularly impinging jets on a hemispherical-dimpled surface," International Journal of Heat and Mass Transfer, 53(15-16), pp. 3045-3056.

[76] Kim, S.-M., and Kim, K.-Y., 2016, "Evaluation of cooling performance of impinging jet array over various dimpled surfaces," Journal of Heat and Mass Transfer, 52(4), pp. 845-854.

[77] Innes, M. C., 2017, "Auxetic structure with stress-relief features," Google Patents.

[78] Javid, F., Liu, J., Rafsanjani, A., Schaenzer, M., Pham, M. Q., Backman, D., Yandt, S., Innes, M. C., Booth-Morrison, C., and Gerendas, M., 2017, "On the design of porous structures with enhanced fatigue life," Extreme Mechanics Letters, 16, pp. 13-17.

[79] Bogard, D. G., 2006, "Airfoil film cooling," The gas turbine handbook, 4, pp. 309-321.

[80] Theocaris, P., Stavroulakis, G., and Panagiotopoulos, P., 1997, "Negative Poisson's ratios in composites with star-shaped inclusions: a numerical homogenization approach," Archive of Applied Mechanics, 67(4), pp. 274-286.

[81] Evans, K. E., and Alderson, A., 2000, "Auxetic materials: functional materials and structures from lateral thinking!," Advanced materials, 12(9), pp. 617-628.

[82] Abramovitch, H., Burgard, M., Edery-Azulay, L., Evans, K., Hoffmeister, M., Miller, W., Scarpa, F., Smith, C., and Tee, K.-F., 2010, "Smart tetrachiral and hexachiral honeycomb: Sensing and impact detection," Composites Science and Technology, 70(7), pp. 1072-1079.

[83] Bertoldi, K., Guerrero, F. E. S., Javid, F., Jette, F., Pham, M. Q., Schaenzer, M., and Shanian, A., 2018, "Hybrid Dimple-And-Void Auxetic Structures With Engineered Patterns For Customized NPR Behavior," Google Patents.

[84] Bertoldi, K., Booth-Morrison, C., Farhangi, M., Innes, M. C., Javid, F., Schaenzer, M., and Shanian, A., 2018, "Auxetic Structures With Angled Slots In Engineered Patterns For Customized NPR Behavior And Improved Cooling Performance," Google Patents.

[85] Nagaraja, S. B., Graham, O., Kwankoo, K., Giridharan, M. G., and Boardman, G. A., 2018, "Acoustic Damper for Gas Turbine Engine Combustors," Google Patents.

[86] Bertoldi, K., Booth-Morrison, C., Farhangi, M., Javid, F., Pham, M. Q., and Taylor, M. J., 2017, "Auxetic Structures With Distorted Projection Slots In Engineered Patterns To Provide NPR Behavior And Improved Stress Performance," Google Patents.

[87] Bertoldi, K., Innes, M. C., Javid, F., Pham, M. Q., Schaenzer, M., and Shanian, A., 2018, "Negative Poisson's Ratio Waffle Structures," Google Patents.

[88] Bertoldi, K., Innes, M. C., Javid, F., Pham, M. Q., Schaenzer, M., Shanian, A., and Taylor, M. J., 2018, "Multi-Layer NPR Structures," Google Patents.

[89] Flores, W., Curbelo, A., Calderon, L., Kapat, J. S., and Ahmed, K., "Adiabatic Film Cooling Effectiveness Measurement of High Performance Combustion Liner Slot Jets," Proc. Turbo Expo: Power for Land, Sea, and Air, American Society of Mechanical Engineers, p. V05BT19A023.

[90] Florschuetz, L., Metzger, D. E., and Truman, C., 1981, "Jet array impingement with crossflow-correlation of streamwise resolved flow and heat transfer distributions," Journal of Heat Transfer.

[91] Garimella, S. V., and Nenaydykh, B., 1996, "Nozzle-geometry effects in liquid jet impingement heat transfer," International Journal of Heat and Mass Transfer, 39(14), pp. 2915-2923.

[92] Morris, G. K., and Garimella, S. V., 1998, "Orifice and impingement flow fields in confined jet impingement."

[93] Schweiz, 2012, "Table of Emissivity of various surfaces," Schaffhausen: Mikron Instrument.

[94] Tsilingiris, P., 2008, "Thermophysical and transport properties of humid air at temperature range between 0 and 100 C," Energy Conversion and Management, 49(5), pp. 1098-1110.

[95] Dieck, R., Steele, W., and Osolsobe, G., 2005, "Test uncertainty. asme ptc 19.1-2005," American Society of Mechanical Engineers, New York, NY.

[96] Figliola, R. S., and Beasley, D. E., 2014, Theory and design for mechanical measurements, John Wiley & Sons.

[97] Moffat, R. J., 1988, "Describing the uncertainties in experimental results," Experimental Thermal and FLuids Science, 1(1), pp. 3-17.

[98] Kline, S. J., 1953, "Describing uncertainty in single sample experiments," Mechanical Engineering, 75, pp. 3-8.

[99] Huber, A. M., and Viskanta, R., 1994, "Effect of jet-jet spacing on convective heat transfer to confined, impinging arrays of axisymmetric air jets," International Journal of Heat and Mass Transfer, 37(18), pp. 2859-2869.

[100] Gupta, G., Fernandez, E., Otto, M., and Kapat, J. S., "Experimental and Numerical Investigation of Fully Turbulent Flow in a Rectangular Channel with Dimples and Protrusions," Proc. AIAA Propulsion and Energy 2019 Forum, p. 4178.

[101] Jeong, J., and Hussain, F., 1995, "On the identification of a vortex," Journal of Fluid Mechanics, 285, pp. 69-94.

[102] Hunt, J. C., Wray, A. A., and Moin, P., 1988, "Eddies, streams, and convergence zones in turbulent flows."